MAGNETOELECTRIC COUPLING AT MULTIFERROIC INTERFACES
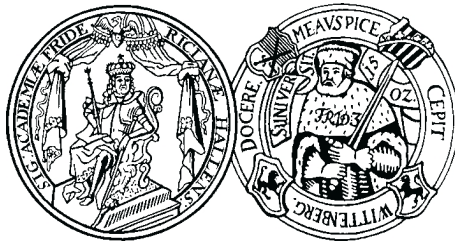
Dissertation

zur Erlangung des akademischen Grades

doctor rerum naturalium (Dr. rer. nat.)

vorgelegt von

MICHAEL FECHNER

geboren am 05.08.1981 in Schkeuditz

Martin-Luther-Universität Halle-Wittenberg

Institut für Physik
der Naturwissenschaftlichen Fakultät II
Fachgruppe Quantentheorie des Festkörpers
Von-Seckendorff-Platz 1, 06120 Halle/Saale

Gutachterin bzw. Gutachter:

1. Prof. Dr. Ingrid Mertig
2. Prof. Dr. Steffen Trimper
3. Prof. Dr. Evgeny Y. Tsymbal

Halle/Saale, den 30 Juni 2010

Contents

INTRODUCTION

The magnetoelectric effect allows controlling a magnetization via an electric field and vice versa. It was first observed in Cr_2O_3 by Astrov [1] in 1960. The discovery caused a lot of excitement due to possible technical application [2,3]. Furthermore, there was a broad interest in the underlying fundamental physics of the effect. However, the intense experimental and theoretical investigations at this time pointed out that the magnetoelectric coupling might always be small and limited [4].

Forty years later two independent events led to a revival of the field [5]. The first was the observation of an induced polarization by a magnetic spiral [6] in $TbMnO_3$. Referring to the unique connection of the polarization with the magnetization in that material, a large magnetoelectric coupling is present. The second was the fabrication of a component multiferroic [7] which exceeded the magnetoelectric coupling coefficient by any other system known at that time by a factor of 36. Consequently, the advanced methods for film growth help to overcome the former issues.

Related to magnetoelectrics are multiferroics [8], which are materials that exhibit at least two order parameters, e.g. polarization and magnetization. Already in the early stage of investigations of the magnetoelectric effect, it was expected that they are ideal candidates for showing large magnetoelectric coupling [5,9]. Nevertheless, at this time only some multiferroic materials were known. The reason for this is that the presence of ferroelectricity and ferromagnetism is mutually exclusive [10], since their driving mechanisms are "contraindicated". This issue was overcome by the usage of advanced theoretical methods to find new mechanisms for ferroelectricity. As a result, new multiferroic materials have been discovered and synthesized that were not known thirty years before [11].

Consequently, magnetoelectric multiferroics are an interesting topic. There are many possible applications for them. The most promising application is their use for data storage due to two reasons. First, the magnetoelectric coupling may allow to write magnetic information by an electric field [3]. Thus, information could be written faster and less power consuming as with other techniques available today. Secondly, the presence of two independent ferroic properties allows to have four logic states in a multiferroic tunnel junction [12].

For both applications successful attempts were already shown [13–15].

Nowadays there are different pathways to grow multiferroic materials [9]. On the one hand, there are the intrinsic multiferroics, which show multiferroic behavior in one phase of a single material, whereas on the other hand there are component multiferroics. They are realized by combining ferroelectric and ferromagnetic materials. Both pathways have advantages and disadvantages. In general, some intrinsic multiferroics show large magnetoelectric coupling but only at low temperature. Furthermore, they exhibit a small polarization or magnetization. This is in contrast to component multiferroics, which exhibit good ferroic properties at room temperature but a rather small magnetoelectric coupling.

The aim of this work is to study two-component multiferroics to identify and elucidate the coupling mechanism. Therefore, interfaces made of a ferroelectric $ATiO_3$ (A=Pb, Ba) compound with a thin ferromagnetic film (Fe or Co) were investigated. Several questions have been arising for such interfaces, which will be captured by this work. They mostly concern the preferred interface structure between both components as well as the magnetic ordering in the ferromagnetic film. The expected strength of the magnetoelectric coupling in such a system shall be determined, too. Furthermore, the mechanisms that are responsible for the coupling are of special interest. At least, the influence of oxygen impurities on the properties needs to be investigated. After answering these questions, the last issue is to apply the established mechanism towards the control of magnetization by the electric polarization.

To solve the questions above first principle methods will be applied. They allow a detailed investigation of structural relaxations and a precise determination of the magnetic properties. The used methods in this work rely on density functional theory [16, 17] (**DFT**) and pseudopotentials generated by the projected augmented plane wave method [18] (**PAW**).

This thesis is organized in three parts. The first part is an introduction of ferroic properties of solids. Furthermore, the origin of the magnetoelectric coupling and its relation to multiferroics is discussed. The reason why ferroelectricity and ferromagnetism are mutually exclusive will be focused on as well. A comparison of intrinsic and component multiferroics will be the last topic of the first part. The second part deals with the used methods and the theory behind them. The basis of DFT as well as the pseudopotential theory will be explained. The last part will consist of two sections. The first is a general overview of the most important results obtained in this work, whereas the second part contains the papers written during the Phd studies. At the end, there will be a general summary and outlook.

FERROIC PROPERTIES

In this chapter of this work the ferroic properties of solids will be introduced. After a general classification of dielectrics, ferroelectricity and the microscopic origin of it will be discussed. In the second part magnetism and in particular ferromagnetism is considered in the same manner. The third part deals with the magnetoelectric effect. Multiferroics and their relation to the magnetoelectric effect are the topics of the last part.

2.1 Ferroelectricity and magnetism

2.1.1 Dielectric materials

Dielectrics are electric insulators whose charge carriers are not mobile. They could be either in a gas, liquid or solid phase. Since the charge carriers are immobilized, an interaction with electric fields leads to an electric polarization $\mathbf{P}$. The interaction can be used to classify the dielectrics. It is obtained from Maxwell's equation for solids [19, 20] and the total charge density of a solid, which can be decomposed into two contributions,

$$\rho = \rho_P + \rho_{ex}, \tag{2.1}$$

where the first term corresponds to a polarization density and the latter to external charges. The polarization density arises from dipoles within the solid e.g., polar molecules or displaced ions, whereas the external charges are due to additional sources. The ρ_P is related to the electric polarization $\mathbf{P}$ by

$$\rho_P = -\nabla \cdot \mathbf{P}, \tag{2.2}$$

which can be shown by the continuity equation for the polarization current density,

$$\frac{\partial}{\partial t}\rho_p + \nabla \cdot \mathbf{j}_p = 0. \tag{2.3}$$

By the usage of equation (2.2) and (2.1) with the first Maxwell equation $\nabla \cdot \epsilon_0 \mathbf{E} = \rho$ the electric displacement field $\mathbf{D}$ is obtained,

$$\nabla \cdot \mathbf{D} = \nabla \cdot (\epsilon_0 \mathbf{E} + \mathbf{P}) = \rho_{ex}. \tag{2.4}$$

The electric displacement field acts as an auxiliary quantity, whereas the electric field $\mathbf{E}$ is the experimental measurable quantity.

After deriving an equation for $\mathbf{P}$, in a next step cases where $\mathbf{P} \neq 0$ will be discussed. This goes towards the classification of dielectric materials. If there are no permanent dipoles within a solid, it is called a real dielectric. In such materials, an applied electric field causes a displacement of the positive and negative charges. The separation of charges generates local dipoles that give rise to a macroscopic polarization. A material is paraelectric, if there exist permanent local dipoles within it, which show no long-range order. Since the orientation of the dipoles is random, there is no macroscopic polarization. Nevertheless, the local dipoles can be aligned by an electric field and the material becomes polarized. Examples for paraelectrics are $SrTiO_3$ and $KTaO_3$. The electric polarization for the first two kinds of materials can be expanded in terms of the electric field

$$\mathbf{P} = \sum_i^3 \gamma_{ij} E_j + \sum_i^3 \beta_{ijk} E_j E_k + ... \qquad . \tag{2.5}$$

For small electric fields the dominant term is the first one. Furthermore, if there is no preferred direction in the material and it is thus isotropic, the term will be simplified to $\mathbf{P} = \chi_e \epsilon_0 \mathbf{E}$. χ_e is the electric susceptibility also called response function. The relation permits a simplification of the relation between dielectric displacement field and the electric field to $\mathbf{D} = (1 + \chi_e)\epsilon_0 \mathbf{E} = \epsilon_r \epsilon_0 \mathbf{E}$.

Until now only materials with a vanishing electric polarization for $\mathbf{E} = 0$ were discussed. Nevertheless, there are materials having a spontaneous polarization $\mathbf{P}_s \neq 0$, which are called pyroelectrics. Theophrastus already made a first reference of them in 314 BC. He observed that if tourmaline is heated it could attract bits of ash. The explanation for the observation is that the electric polarization changes when the material is heated, which gives rise to an electrochemical potential causing an attractive force. The electric polarization within these materials is due to the off centering of the atoms from their centrosymmetric positions which give rise to local dipoles. To create a macroscopic polarization it is necessary that these dipoles show a cooperative long-range order. The dipole-dipole interaction is the driving force for this alignment. Pyroelectrics show a complicated behavior in electric fields, so they are considered as nonlinear materials.

Ordinary pyroelectric materials inhabit only one specific direction for the electric polarization, which is determined by the crystal structure. Consequently, the only way to switch the polarization is to perform an essential redeployment in the crystal structure. This requires the application of an unphysical large electric field. However, there is an interesting subclass of pyroelectrics, which are ferroelectrics. In these materials, the electric polarization can point in two or more directions. A more precise definition is: A material is called ferroelectric, if it fulfills two conditions. First, it has to be an insulator, which exhibits a spontaneous polarization. Secondly, this polarization has to be switchable between different stable states [21, 22]. The switching is done by the interaction of the polarization with an electric field ($-\mathbf{E} \cdot \mathbf{P}$). Ferroelectrics were first discovered 1921 by Valasek [23]. He found out that Rochelle salt shows a hysteresis of the electric polarization when an electric field
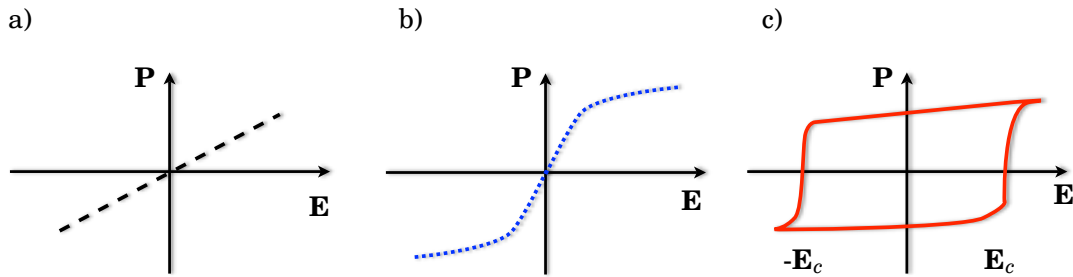
FIGURE 2.1: The figure shows schematically the electric polarization **P** of dielectrics as a function of an external electric field **E**. Figure (a) depicts the linear increase of a real dielectric, whereas (b) shows the situation for a paraelectric material with two different slopes. The curve (c) shows the hysteresis curve of a ferroelectric. The points E_c mark the coercive fields needed to switch the polarization.

is applied. Due to the similarity with the magnetic hysteresis, it was called a ferroelectric. The mechanisms that lead to ferroelectricity will be the topic of the next chapter. It should be mentioned that due to their crystal symmetry ferroelectrics are also piezoelectric. Piezoelectricity is the ability of some materials to generate an electric field as a response to mechanical stress. All ferroelectrics are piezoelectric and pyroelectric.

The switchable polarization, the response to stress and the sensitivity to temperature are three remarkable properties of ferroelectrics. They make them attractive candidates for technical applications. The switchable polarization allows the application as random access memories (RAM), while the sensitivity for temperature due to the pyroelectricity is useful for sensors. The piezoelectric properties allow constructing actuators or transducers.

A short summary of the classification is depicted in figure 2.1, where the polarization as a function of the applied electric field is drawn. In a real dielectric, the polarization increases linearly with the field strength (a) as discussed above. For paraelectrics, the curve has two different slopes. For small electric fields, the dipoles are aligned in the direction of the field. After the orientation process the slope will decrease and the polarization saturates. The ferroelectric hysteresis is sketched in (c). The curve has a nonzero polarization for E= 0 and shows saturation for high fields similar to paraelectrics. In the figure, E_c marks the coercive field needed to switch the polarization.

2.1.2 Microscopic understanding of ferroelectricity

In this section, the microscopic mechanism that causes ferroelectricity will be introduced. Nowadays many materials that show ferroelectricity are known. The intensive investigations of these materials starting in 1990 have led to a deeper understanding of mechanisms that produce ferroelectricity [24]. Since the focus of this work is on ferroelectrics with perovskite structure, the discussion here is restricted on them. The best investigated ferroelectric and consequently a prototypical is barium titanate ($BaTiO_3$). It has an ABO_3 pe-

rovskite crystal structure depicted in figure 2.2 (a). In the perovskites structure A cations are placed on the corners of the unit cell and the B cation finds its place in the center. The face-centered sites are occupied with oxygen atoms. They form an octahedron around the B site giving it a coordination number of six, while twelve oxygen atoms surround the A site. $BaTiO_3$ has a cubic perovskite structure at temperatures above 130 °C. Below this temperature its structure becomes distorted by displacing the Ti and oxygen atoms in opposite directions along the [001] axis. Furthermore, the cell is elongated in the same direction, causing a tetragonal unit cell. The structural change produces an electric polarization of about 26 $\mu C/cm^2$. Since the [100], [010] and [001] axis are equivalent in the cubic phase the change can occur in any of these directions. In the following, the tetragonal axis will be taken as [001]. The equivalence of the [001] and [00$\bar{1}$] axis cause two distinct polarization states, which are shown in figure 2.2 (b) and (c).

The ferroelectric phase transition can be described by a continuous change of the structure given by a parameter ξ. In the case of $BaTiO_3$ ξ is the displacement of Ti and oxygen atoms. The internal energy U has a double well shape, shown in the center of figure 2.2, for a continuous evolution of ξ. For $\xi = \pm 1$ the potential has two minima, that correspond to the stable polarization states. If an electric field is applied, a shift of the potential will lower the energy of one minimum and consequently the system will prefer this polarization state. However, the switching of the polarization in bulk ferroelectrics is not due to a uniform switching through the high symmetry structure at $\xi = 0$. This arises from the fact that bulk ferroelectrics break into domains and thus the switching can be due to nucleation and growth of them, which are processes with lower energy barriers [21, 25].

$BaTiO_3$ will undergo two more phase transitions, if the temperature is further lowered. The second transition is from tetragonal to orthorhombic (around 5 °C) and the third one to rhombohedral (around -90 °C). During the transition, the polarization rotates from [001]
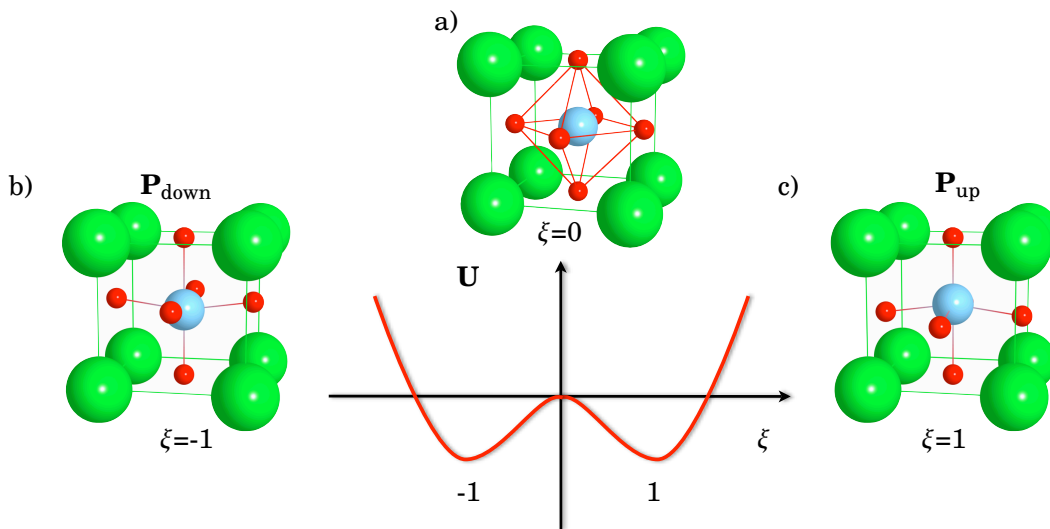

FIGURE 2.2: Crystal structure of $BaTiO_3$ in its paraelectric cubic structure ($\xi = 0$) and in its ferroelectric tetragonally distorted structures with $\xi = \pm 1$.

to [011] and finally to [111]. The first transition is a second order phase transition and the following two transitions are of first order. This is related to the symmetry of the structures. All structures are subgroups of the cubic structure, but only between the cubic and tetragonal structure exists a group-subgroup relation. Due to that, the first transition is of second order, whereas the two others are of first order. Furthermore, there are some perovskite ferroelectrics that show only one phase transition, i.e. $PbTiO_3$. However, not all perovskite crystals exhibit a ferroelectric phase, since there are competing forces in these structures that favor polar and non-polar ground states. $SrTiO_3$ for example is a perovskite with no polar distortion at all. In the following, the requirements for the stabilization of the ferroelectric phase will be the topic.

The predominant reason for the displacement of the atoms in the perovskite structure is a structural frustration. Goldschmidt [22] put already in 1926 criteria for the stability of the perfect cubic perovskite structure. Therefore, he used two rules, which were successfully applied before to ionic binary compounds. The first rule states, that a cation will be surrounded by as many anions as it can touch, but no more. The second rule states, that all the anions must touch the cations and the anion-cation distance is obtained as the sum of their ionic radii. In consequence, the perovskite structure is mainly determined by the oxygen octahedra, whereas the A site cation has to fill only the holes in-between. By considering these geometrical rules the cubic perovskite structure has to fulfill the following condition:

$$r_A + r_O = \sqrt{2}\,(r_B + r_O)\,, \tag{2.6}$$

to be stable. Here r_x (x=A,B,O) corresponds to the ionic radius of an A, B or O atom. The introduction of a tolerance factor t allows to discuss this relation for a different number of compounds. Thus the relation that has to be considered is

$$t = \frac{r_A + r_O}{\sqrt{2}\,(r_B + r_O)}\quad. \tag{2.7}$$

Different structures result as a function of t. If $t \approx 1$ the cubic perovskite structure will be favored. For $t > 1$ the structure is dominated by the A-O distance since the B ion is too small to fill the oxygen octahedron. Hence, the B cation shifts off-center, leading to a polar structure. $BaTiO_3$ is a good example for this case. If $t < 1$ the A side cation is too small to fill the hole between the octahedra, there will be a lot of space left for the 12 oxygen neighbors. The resulting structure depends on the size of t. If t is slightly less than 1, the system prefers rotations and tilting of the oxygen octahedra like, in $SrTiO_3$. If t is smaller the structure will show large distortions of the B and A site cations, like in $PbTiO_3$. In the case of an even smaller t the compound itself will have a strongly distorted structure. Consequently, the structure dramatically changes until the A site cation has only 6 neighbors, like in $LiNbO_3$. A system with t very different from 1, will favor any of the other ABO_3 structure types instead. The drawback of the geometrical approach is that it may predict the structure for a certain composition but not unveil the underlying microscopic mechanism.

The more profound description for the off centering of the ions in the perovskite structure is based on the microscopic bonding mechanisms [22] between the ions. If all bonds

were just ionic and all ionic radii fit the structure ($t = 1$), the system would prefer a non off-centered cubic perovskite structure, thus being not ferroelectric. This arises from the fact that the Coulomb interaction may favor the ferroelectric state, but the short-range repulsions between the electron clouds of adjacent ions are only minimized for non-polar cubic structures [26, 27]. Consequently, the existence or absence of ferroelectricity is determined by a balance between these short-range repulsions and an additional force that can stabilize the ferroelectric state [28]. As a source of stabilization the second-order or pseudo-Jahn-Teller effect [29–32] has been identified.

The Jahn-Teller effect [33] is the geometrical distortion of a non-linear molecule to minimize the total energy. Hermann Arthur Jahn and Edward Teller found it. They proved by applying group theory that a non-linear degenerate molecule could not be stable. The molecule undergoes a distortion that removes the degeneracy and lowers the total energy. Initially developed for molecules the formalism could also be applied to transition metal oxides with octahedral complexes.

An intuitive way to access this effect is to expand the energy of the electronic ground state E as a function of the coordinate distortion ξ [22]

$$
\begin{aligned}
E(\xi) \quad = \quad & E(0) + \langle 0 \,|\, (\delta H/\delta \xi)_0 \,|\, 0\rangle \xi \\
& + \frac{1}{2}\left(\langle 0 \,|\, (\delta^2 H/\delta \xi^2)_0 \,|\, 0\rangle - 2 \sum_{n \neq 0} \frac{|\langle 0 \,|\, (\delta H/\delta \xi)_0 \,|\, n\rangle|^2}{E_n - E(0)} \right) \xi^2 \\
& + \cdots \quad .
\end{aligned}
\tag{2.8}
$$

$E(0)$ is the ground state energy of the undistorted system and E_n are the excited-state energies of the undistorted system. The whole expansion can be classified into two parts. The linear term corresponds to the first order Jahn-Teller contribution, which would be nonzero for degenerate states, but vanishes in our case. The characteristic tetragonal distortion in some $3d^1$ perovskites ($SrVO_3$) originates from this term. For the stabilization of ferroelectricity, the two second-order terms are important. The first term is always positive, whereas the second one is always negative. Consequently, a reduction in energy of second order can only be achieved if the second term is larger than the first one. The first of the second order terms can be associated with an increase in energy due to a distortion of the system without redistribution of electrons. It is dominated by the Coulomb repulsion between the ions. Obviously, for closed-shell ions without spatially distributed valence electrons it will be very small. The second term corresponds to a hybridization of the ground and excited states due to the distortion. It can be associated with the formation of new bonds in the disturbed system and will only be large if two conditions are fulfilled. Firstly, the denominator $E_n - E(0)$ has to be small. Hence, there has to be a low lying excited state available, which is close to the ground state. Secondly, the scalar product in the nominator must be nonzero. Generally, this is the case, if the product of the symmetry representations of the ground state, excited state and the distortion will be symmetric. Therefore, a centrosymmetric ground state has to undergo a non-centrosymmetric distortion towards non-centrosymmetric excited state. Fulfilling these conditions, the second term may be larger than the first one and the distortion takes place.
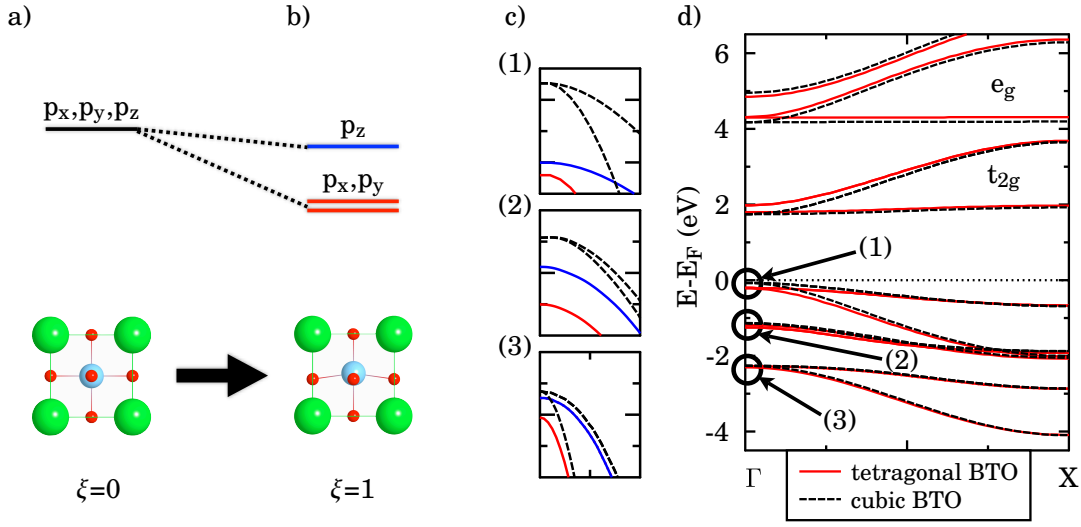
FIGURE 2.3: Lifting of the degeneracy of the p and d states in cubic and tetragonal $BaTiO_3$ by distortion. The shift of the energy levels is shown from left to right starting from cubic $BaTiO_3$ (a) towards tetragonally distorted $BaTiO_3$ (b). At the right-hand side in (d) the band structure of cubic and tetragonally distorted $BaTiO_3$ is shown. The small pictures (c) show a zoom into the band structure around the Γ point. The characters of the p bands (p_x, p_y, and p_z) at the Γ point are drawn in the same color like in (b).

The Jahn-Teller effect in $BaTiO_3$ will be discussed in two steps. First there will be a general discussion of the downshift of energy levels as a result of the distortion [34]. This is followed by a comparison of the energy levels picture with a real bandstructure. In $BaTiO_3$ the d states are hybridized with the O $2p$ states. The electrons are occupying the lowest energy levels in the ground state, which are mainly at the O sites. Consequently, the oxygen atoms become negatively charged while Ti^{4+} is formally in a d^0 state. In the cubic structure of $BaTiO_3$ the p states are all threefold degenerate due to symmetry of the crystal structure as depicted in figure 2.3 (a). The Ti^{4+} is a closed-shell ion and therefore can be shifted off-center because the increase in Coulomb repulsion is small. The off-centering lifts the degeneracy as shown in 2.3 (b). In the distorted structure the p levels become downshifted in energy because of the Jahn-Teller effect. The p_x and p_y levels maintain their degeneracy due to symmetry and experience a larger shift, since the overlap with the Ti orbitals is additionally reduced.

In a real bandstructure the downshift can be clearly observed at the Γ point. Figure 2.3 (d) shows the bandstructure of cubic and tetragonally distorted $BaTiO_3$. The lowest unoccupied bands reveal the character of Ti d states, while the highest occupied bands have p character. In the cubic state all p bands are degenerated at the Γ point, which is obvious from the zoom in figure 2.3 (c). The d bands are split due to the crystal field in t_{2g} and e_g bands. If the Ti atom is off-centered and the cell becomes tetragonal the degeneracy of p bands is lifted. Only the d_{xz} and d_{yz} bands are still degenerated after the distortion. The new arrangement of the p bands at the Γ point lowers the total energy corresponding

to the discussion above.

There are several other sources for ferroelectricity beside the Jahn-Teller effect. For example the stereochemical activity of ns^2 lone pairs of electrons [10]. In some materials lone pairs mix in some cation-anion p character, loosing their center of symmetry. In GeTe this alone leads to ferroelectricity, whereas in other cases it accompanies the Jahn-Teller effect to stabilize the ferroelectric phase. For example in $PbTiO_3$ [26, 35] the activity of the lead ion, causes strain that prevents a phase transition from the tetragonal phase towards a rhombohedral phase. This is in contrast to $BaTiO_3$, since barium has only $2p$ states which cannot hybridize. Another kind of driving mechanism takes place in geometrically driven ferroelectrics [34]. In these materials rotations called "Glazer tilts" of the oxygen octahedra occur. The distorted octahedrons still keep their corner-sharing connectivity. Hence, in cubic perovskites this cannot be the source of ferroelectricity because rotations of the octahedra cause counter rotations in their neighbor sites maintaining inversion symmetry. However, in a material with a different lattice and symmetry this may indeed lead to a ferroelectric ground state.

The three mechanisms discussed above explain the emergence of dipoles in a material. To create a macroscopic polarization it is necessary that all dipoles align in the same direction. The dipole-dipole interaction is the responsible force that drives this long-range ordering. [36]. However, in some cases competing forces overcome the dipole-dipole interaction. Since this depends strongly on the material, it cannot be discussed in general here. The competition between the forces may result in different alignments of the dipoles. Hence, beside the ferroelectric long-range order of dipoles two common other ones exist. If dipoles in a material face each other, the material is called antiferroelectric. Obviously, in an antiferroelectric the total polarization is zero. In some cases, also multiple distortions are present, which create local dipole moments of different size and opposite direction. The resulting polarization for such an alignment is usually small and the material is called ferrielectric.

The end of this section deals with thin ferroelectric films. Ferroelectricity is a collective phenomenon, arising between the long-range Coulomb interaction and the short-range covalent repulsion. It is a bulk intrinsic property and thus changes drastically, if the volume will be reduced. In the past, it was expected that ferroelectricity would disappear in thin films because of the depolarization field. However, after improving experimental techniques, in particular to grow structures on the nanometer scale and to probe their local properties, it turns out that ferroelectricity is preserved at the nanometer scale. Recently, theory predicted that ferroelectricity could exist in a film as thin as 1.2 nm [37]. So far, experimental observation shows that below 10 nm ferroelectricity is stabilized [38, 39]. The crucial question if there is a size limit for ferroelectricity is up to now unanswered. The response depends strongly on the mechanical, electrical and chemical boundary conditions around and in the film. Therefore this question can only be answered for each specific system [32, 37–42].

In the following, the main issues concerning thin ferroelectric films are listed. Firstly, the importance of surface effects should be considered. The missing neighboring atoms at the surface affect the bonding of nearest neighbors and thus lead to a new balance between long-

range and short-range forces. Secondly, mechanical effects should be taken into account. A ferroelectric film may be grown on a substrate with a different lattice constant. This lattice mismatch may cause a strain that can couple to the ferroelectric polarization. The coupling can result in a stabilization or suppression the electric polarization. The electrostatic boundary conditions have to be examined, too. A finite electric polarization normal to the surface always gives rise to a depolarization field in the ferroelectric film. From this field a huge electrostatic energy may originate that suppress the ferroelectric instability. The only way to preserve ferroelectricity from this is to screen the surface charge. The ability of screening depends on the chosen electrodes. Finally, the importance of defects, oxygen vacancies and fluctuations in the chemical composition are unknown. Oxygen vacancies may especially act as charge carriers and can make an insulating ferroelectric film becoming conducting.

2.1.3 Magnetic materials

In this section, the classification of magnetic materials will be presented by considering the material equation for magnets. First, the material equation will be derived from Maxwell's equations. The starting point for this is the total current density $\mathbf{j}$, which aggregates from three contributions,

$$\mathbf{j} = \mathbf{j}_f + \mathbf{j}_p + \mathbf{j}_m \quad . \tag{2.9}$$

$\mathbf{j}_f$ is the current density of the free unbound charges, while the two last terms are due to bound charges. The current density of the polarization-charges $\mathbf{j}_p$ is related to the electric polarization via

$$\mathbf{j}_p = \frac{\partial}{\partial t} \mathbf{P} \quad . \tag{2.10}$$

This is obtained by the continuity equation for the polarization charge density (2.3) and a comparison with equation (2.2). For static problems, the partial derivative vanishes and so does the current density.

The third current density $\mathbf{j}_m$ is important for magnetic materials. It arises from the motion of the electrons on stationary orbits around the cores of the atoms. Since a moving charge creates a magnetic field, any electron on an orbit is a magnetic dipole $\mathbf{m}$. The sum of these dipoles is considered to be the magnetization $\mathbf{M}$ of a solid,

$$\mathbf{M} = \frac{1}{V} \sum_i^N \mathbf{m}_i \quad . \tag{2.11}$$

The relation between the magnetization and the current density can be obtained as follows [43]. The current density is stationary, so that $\nabla \cdot \mathbf{j}_m = 0$ thus $\mathbf{j}_m$ may be written as the curl of a vector, which is the magnetization:

$$\mathbf{j}_m = \nabla \times \mathbf{M} \quad . \tag{2.12}$$

The two equations (2.10) and (2.12) can be used in Maxwell's equation for the magnetic induction. After some comprehensive simplification, one arrives at:

$$\nabla \times \mathbf{H} = \mathbf{j}_f + \dot{\mathbf{D}}, \tag{2.13}$$

with the magnetic field $\mu_0\mathbf{H} = \mathbf{B} - \mathbf{M}$. It is a derived field and the analogue to the electric displacement field.

The relation between magnetic field and magnetization can be discussed in the same manner as for dielectrics. The magnetization can be expanded in terms of the magnetic field $\mathbf{H}$

$$\mathbf{M} = \sum_i^3 \gamma_{ij}H_j + \sum_i^3 \beta_{ijk}H_jH_k + ... \qquad . \qquad (2.14)$$

If a solid is isotropic and shows linear response to a magnetic field, its magnetization will be $\mathbf{M} = \chi_M\mathbf{H}$, where χ_M is the magnetic susceptibility. Again, a relative permeability μ_r, $\mathbf{B} = (1 + \chi_M)\mu_0\mathbf{H} = \mu_r\mu_0\mathbf{H}$ may be introduced here, but in the following discussion only the susceptibility will be used.

The magnetic susceptibility ranks magnetic materials. This classification is similar to that of electric insulators in section 2.1.1. If within a material no magnetic dipoles exist, it is called diamagnetic. In diamagnets, a magnetization is caused by induction. An applied magnetic field creates magnetic dipoles, which following Lenz's law, are oppositely aligned to the external field. Hence, the magnetic susceptibility is negative; this is in contrast to dielectrics, in which the induced electric polarization points in the same direction as the external field. In diamagnetic materials χ_M is typically independent of temperature and applied field strength. Materials are only called diamagnetic in the absence of other forms of magnetism like paramagnetism or collective magnetism, since they overpowered it. Pronounced diamagnetism occurs for example in Cu, Hg and Si.

If there are permanent magnetic dipoles in a material that show no long-range order, it is called paramagnetic. A collective alignment can be forced by application of a magnetic field, like in paraelectrics. There are two origins for the appearance of the magnetic dipoles. They can be due to partially occupied valence of atoms. In this case, the dipoles are localized and the material is a magnetic insulator. However, the magnetic dipoles can also be due to the spin of the conducting electrons in solids. Therefore, the magnetic moments are nonlocal and the paramagnetism is called Pauli paramagnetism. In both cases, the effect of an external magnetic field on the magnetization is assumed linear.

Paramagnets and diamagnets do not show any magnetization without an external magnetic field. In analogy to dielectrics, one could expect pyromagnetism. Hence, a material in which the magnetization points along one certain direction and is only switchable with unphysical fields. However, there is no material with this property. Even more important is the fact that the multiple definitions of the term pyromagnetic made it uncommon in the 20th century. Thus, ferromagnetism will be introduced. A material is ferromagnetic if it exhibits a spontaneous magnetization, which has to be switchable between stable states. The switching is driven by the interaction of the magnetization with a magnetic field $(-\mathbf{H}\cdot\mathbf{M})$. A material can show this collective phenomenon, if there are permanent dipoles available that are aligned without any applied field. The driving force for the alignment in ferromagnets is the quantum mechanical exchange interaction, which will be discussed in the next section 2.1.4. The magnetic moments in ferromagnets are caused due to the same effects as in the paramagnets. They could be localized like for example in (Gd, EuO) or itinerant,
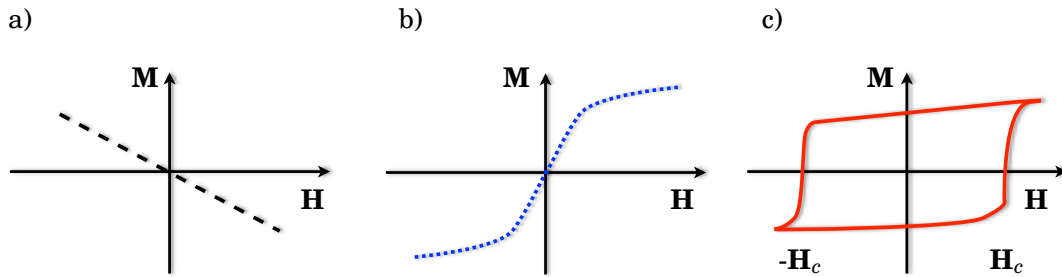
FIGURE 2.4: The magnetic polarization **M** (magnetization) is shown as a function of an applied external magnetic field **H** for different magnetic materials. Figure (a) depicts the linear decrease of a diamagnet, whereas (b) shows the situation for a paramagnet with two different slopes. The hysteresis loop of a ferromagnet is depicted in (c).

like in Fe, Co or Ni. Beside ferromagnetism, two other kinds of magnetic ordering are important. The first is the antiferromagnetism in which moments of same size are aligned in opposite directions, leading to a vanishing total magnetization. A more general case of this ordering is ferrimagnetism, where the magnetic moments have different sizes and line up in opposite direction, which finally causes a small magnetization.

To summarize this section on magnetic materials and to underline the similarity between dielectrics and magnets, figure 2.4 can be considered. It shows the response of the magnetization of the different classes discussed above as a function of an applied external field. All cases have their pendants to dielectrics, besides diamagnetism where the sign of the susceptibility is different. In particular, the paramagnetism and ferromagnetism shows saturation and the latter also hysteresis. In the next section, the mechanism causing the ordering of ferromagnets and antiferomagnets will be discussed.

2.1.4 Microscopic understanding of magnetism

In this section, two different theories that are capable to describe the origin of collective magnetic ordering are presented. They are the localized moment theory of Curie and Weiss and the Stoner band [44] theory. Within the theory of Curie and Weiss an internal molecular field is postulated, which aligns magnetic moments. At $T = 0$ the field is strong enough to line up all magnetic moments in one certain direction, and that causes a finite magnetization. If the temperature is raised the thermal energy $\kappa_B T$ will lead to fluctuations of the orientations of the moments, which decreases the total magnetization. The ordering will be completely lost above a critical temperature, the Curie temperature T_C. Above this temperature, the system will be in a paramagnetic state. Near the phase transition the theory leads to the observed Curie–Weiss law behavior of the susceptibility of many metals. However, besides the unsatisfactory fact that the postulated molecular field is not known the theory suffers some drawbacks. First, there is a large discrepancy between the theoretical predicted magnetic moments for metals and the experimentally observed ones. Furthermore,

the moments in the ferromagnetic and paramagnetic phase should be the same, which is as well not found. Due to these drawbacks, a more precise description had to be considered in metals, that is the Stoner model.

In the Stoner model the driving force for the alignment of magnetic moments is the exchange energy. The basis of the model is the minimization of the total energy because of a nonvanishing magnetization. To obtain a condition if this transition can take place, it is useful to consider a model density of states as shown in figure 2.5 (a). In the figure, a transfer of electrons between spin channels is illustrated. A finite magnetization occurs because of the unequal population of states. The spin channel with the larger population is called majority spin channel, whereas the other is called minority spin channel. The transfer is accompanied by two changes in the total energy. There is an increase of the kinetic energy of the system δE_{kin}=D(E$_F$)δE^2/2, and there is also a decrease of potential energy $\delta E_{pot} = -\frac{1}{2}I \ (D(E_F)\delta E)^2$, which is associated with the finite magnetization. The constant I is the Stoner parameter that measure the strength of the exchange correlation. The sum of both contributions

$$\Delta E_{tot} = \Delta E_{pot} + \Delta E_{kin} = -\frac{1}{2}D(E_F)(\delta E)^2(1 - I \ D(E_F)),$$ (2.15)

shows that there will be a gain of energy with a finite magnetization, if

$$I \ D(E_F) \geq 1 \ .$$ (2.16)

This is the Stoner criterion. It states that a material will have a finite magnetization, if the product of exchange correlation strength and density of states at the Fermi level are large. Furthermore, the magnetic moment must not be an integer number, in contrast to the Curie-Weiss theory.

In the following, the Stoner criterion is discussed for selected metals that are Zn, Cu and Ni. Figure 2.5 (b) shows schematically the density of states of these three metals. The main features are the broad s band density (dotted) and the narrow d state density (solid). In the case of Zn and Cu the Fermi energy lies within a region of pure s states.
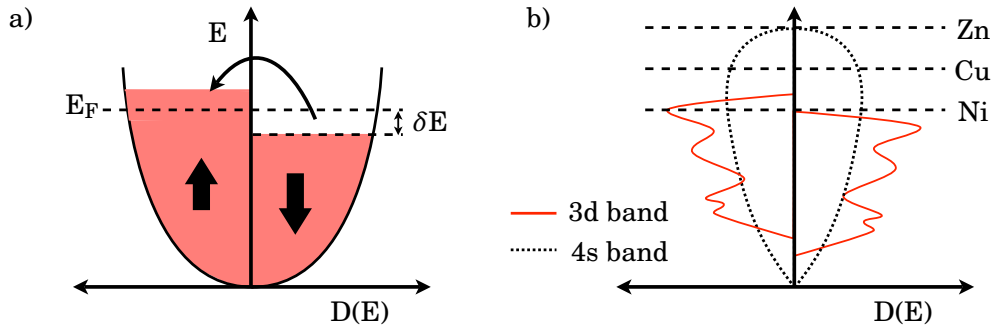

FIGURE 2.5: Figure (a) sketches the transfer of electrons from the minority to the majority band due to exchange interaction. In (b) the density of states for Zn, Cu and Ni is shown. The dashed line corresponds to the Fermi energy E_F.

Consequently, the energy needed, to promote electrons from one spin band to the other, is expensive with respect to the energy gain discussed above. Thus, these systems will show no ferromagnetism, in contrast to Ni, whose Fermi energy lies in a region of overlapping s and d bands. A high density of states around the Fermi energy is available and the Stoner criterion is fulfilled. Hence, there will be an energy lowering, if electrons are transferred between the spin channels and the metal becomes magnetic.

The two theories keep the main mechanisms that are essential in real systems. In particular the theory of Weiss and Curie describes well the magnetism in rare-earth magnets with localized f states, whereas the Stoner theory holds for the metallic ferromagnets. Nevertheless, in systems with complicated compositions more mechanisms have to be considered to explain the magnetic ordering. In these systems, the exchange energy is also minimized, but the minimization may be accompanied by different alignments of the magnetic moments with respect to each other. The behavior in such system can be derived by the Goodenough-Kanamori-Anderson rules [45] (**GKA**). These three rules explain the spin-spin orientation of electrons in two neighboring orbitals depending on their population and orientation. The first rule states that a 180° exchange between occupied or unoccupied orbitals will be strong antiferromagnetic. The second implies that the 180° exchange between a occupied and an unoccupied orbital will be weakly ferromagnetic, whereas the last rule is that the 90° exchange between filled orbitals is weak and ferromagnetic.

The magnetic structure is obviously very sensitive to the valence of the atoms. This can further be illustrated with the following example. Considering an oxygen atom with a 2^- valence surrounded by two Mn^{4+} atoms as shown in figure 2.6. For simplification the energetically highest d orbitals should be $d_{x^2-y^2}$ and d_{z^2}. This corresponds to the situation in $LaMnO_3$. To maximize the orbital momentum the four electrons of Mn occupy the three lowest d orbitals and the d_{z^2}, which is shown in figure 2.6 (a). Since the oxygen atom has a 2^- valence all its p orbitals are occupied. The system can reduce its total energy by kinetic exchange due to the covalent bond between the ions. The virtual transfer between the left-hand Mn and O requires that two electron spins have opposite directions, to fulfill Pauli's law. The same holds for the right-hand Mn and the oxygen. Consequently, the magnetic moments on the Mn sites align antiparallelly with respect to each other. If one Mn level has a different vacancy as shown in figure 2.6 (b), the situation changes. In this case, the electrons on both Mn sites have identical spin arrangements. The alignments of the spins in the examples are obtained from the GKA rules. The first example illustrates the superexchange, whereas the second one shows the double exchange.

The variety of magnetic ordering is large. Thus, the discussion here is restricted to examples with collinear alignment of the magnetic moments. Nevertheless, there are materials with non-collinear magnetic structure, where any magnetic moment can point in a different direction. Since the system under consideration in this work does not show such behavior, the discussion is restricted here. In the next part of this work, the ferroelectric and ferromagnetic properties will be brought together. Obviously, this is only possible under certain conditions.
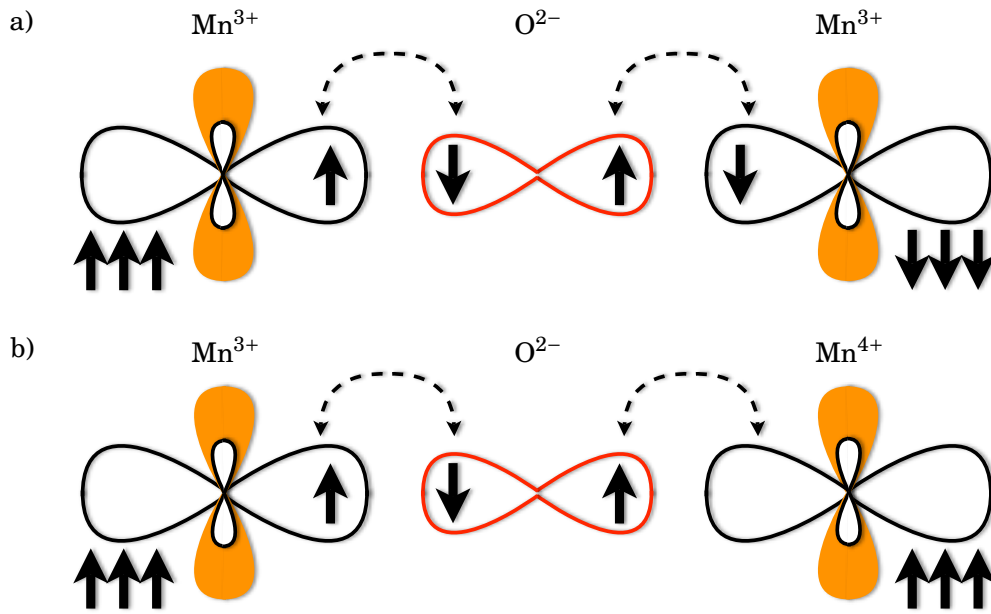
FIGURE 2.6: Sketched mechanism for superexchange in (a) and double exchange in (b). The arrows in the figure show the directions of the spin of the electrons. The $d_{x^2-y^2}$ of Mn are shaded orange, d_{z^2} are shown with black lines and the p_z orbitals of oxygen are colored red.

2.2 Magnetoelectrics and multiferroics

The second part of this chapter will bring the two topics of the first one together. In a first step the magnetoelectric coupling will be introduced, this is followed by a discussion on multiferroics. The relation between these two topics will as well be outlined in both parts.

2.2.1 Magnetoelectric coupling

Materials that exhibit a certain symmetry allow a coupling between electric, magnetic and strain fields [9]. Figure 2.7 (a) illustrates these interactions. All changes of the magnetization or the polarization by an electric or magnetic field are considered as magnetoelectric coupling or magnetoelectric effect. Interestingly, besides the direct modification of the magnetization/polarization via an electric/magnetic field, there is as well an indirect strategy. For example, the induction of a strain via an electric field may affect the magnetization via magnetostriction.

Röntgen was the first who observed the magnetoelectric effect in 1888 [46]. He found out that a moving dielectric shows a magnetization in an electric field. Röntgen already considered that the effect is related with symmetry aspects of the sample. Some years later Debye attempted to find a static magnetoelectric effect and introduced the term magnetoelectric [47]. Later Landau and Lifschitz revealed the symmetry requirements for the allowance of the magnetoelectric effect. It can only occur in materials in which time reversal
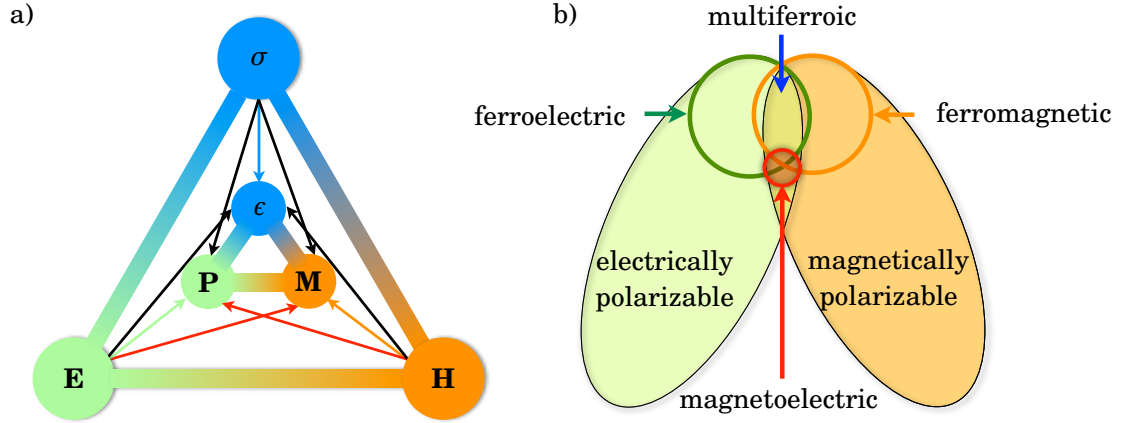
FIGURE 2.7: In (a) the cross-coupling of properties in a material are shown. The scheme in (b) shows the relation between ferroic properties and magnetoelectric coupling.

symmetry is broken. The violation may be achieved by applying a magnetic field, movement of the sample or by long range magnetic ordering. Dzyaloshinskii [48] then showed theoretically that Cr_2O_3 would allow the magnetoelectric effect, which was experimentally proven by Astrov [1] one year later.

An intuitive approach to the magnetoelectric effect is the expansion of the free energy [9] as a function of the electric and magnetic field:

$$
\begin{aligned}
F(\vec{E}, \vec{H}) \quad = \quad & F_0 - P_i^S E_i - M_i^S H_i \\
& - \frac{1}{2}\epsilon_0 \chi_{ij}^e E_i E_j - \frac{1}{2}\mu_0 \chi_{ij}^m H_i H_j - \alpha_{ij}^{me} E_i H_j \\
& - \frac{1}{2}\beta_{ijk} E_i H_j H_k - ....
\end{aligned}
\tag{2.17}
$$

P_i^S and M_i^S are the spontaneous polarization and magnetization respectively and χ^e and χ^m the corresponding electric and magnetic susceptibilities. The total polarization is obtained by taking the derivative of the free energy with respect to the electric field,

$$
\begin{aligned}
P_i(\vec{E}, \vec{H}) \quad = \quad & -\frac{\partial F}{\partial E_i} \tag{2.18} \\
= \quad & P_i^s + \epsilon_0 \epsilon_{ij} E_j + \alpha_{ij} H_j. \tag{2.19}
\end{aligned}
$$

For the magnetization it follows

$$
M_i(\vec{E}, \vec{H}) \quad = \quad M_i^s + \mu_0 \mu_{ij} H_j + \alpha_{ij} E_j . \tag{2.20}
$$

The total magnetization and polarization are composed of three terms: the spontaneous part, the induced part by the conjugated field, and the magnetoelectric part. The higher order terms may be neglected here. The constant α_{ij} is the linear magnetoelectric tensor, which is a second rank axial tensor. It was shown [19] that it is only nonzero if both inversion and time reversal symmetry are broken. However, the appearance of a combination of both symmetries is allowed.

The symmetry aspects can be used to encounter where linear magnetoelectric materials may be found. Considering the scheme in figure 2.7 (b), they are located in the overlap between the electric and magnetic polarizable materials. There are two distinct realizations for magnetoelectrics. The first includes materials that are ferroelectric and ferromagnetic in the same phase and thus multiferroic. In the second area, there are materials that are only polarizable and not ferroic. In the following, the expected strength of the magnetoelectric coupling in multiferroics and non-multiferroics will be discussed.

Symmetry considerations give only the necessary condition for the appearance of the magnetoelectric effect and cannot account for the strength of it. The size of α_{ij} can only be estimated by the investigation of interactions on a microscopic scale. Therefore, α may be decomposed into two parts,

$$\alpha = \alpha_{electronic} + \alpha_{ionic}. \tag{2.21}$$

The first part is the response of the pure electron system on an applied field, whereas the second part includes changes due to the movement of ions. In most systems α_{ionic} will be the largest contribution [49], since it is associated with structural distortions. These distortions influence strongly the interactions in a system as shown by the following considerations. First, the application of an electric field may cause a shift of the ions with respect to its ligands. Due to that the environment of the ion is slightly changed and thus is the ligand field. The orbital overlap can alter by the shift, too. Consequently, the exchange integrals and energies will be modified. Furthermore, the non-uniform shift of ions carrying a magnetic moment alter the dipolar field and thereby the magnetic anisotropy. However, in some systems $\alpha_{electronic}$ may also be considerable large. In particular within materials, where the application of an electric field, only shifts the electrons away from their equilibrium positions around the cores. The shift may change the orbital magnetic moment and thus the total magnetization.

The above-mentioned mechanisms have been used to explain the strength and behavior of α for several systems. For example Hornreich and Shtrikman [50], could describe the temperature dependence of α_{ij} of Cr_2O_3. However, the most important result was obtained by Brown et al. [4]. They showed that there is an upper limit of the magnetoelectric coefficient,

$$\alpha_{ij}^2 < \chi_{ij}^e \chi_{ij}^m, \tag{2.22}$$

by considering the free energy of a magnetoelectric material in the presence of an electric and magnetic field. From the equation above it is obvious that only materials with high electric and magnetic susceptibilities may show large magnetoelectric effects. High electric/magnetic susceptibilities occur in ferroelectric/ferromagnetic materials. Thus, the search for materials with large magnetoelectric effects is related to the search of materials, which show both ferroic properties in the same phase. Nevertheless, two points should be made clear here. Firstly, there are also some non-ferroic materials that exhibit high susceptibility as well, for example $SrTiO_3$. Therefore, a compound of non ferroic materials may show a large α_{ij} [51] as well. Secondly, the derivation of equation (2.22) was derived neglecting strain. Hence, a strained material can show large magnetoelectric response, too.

2.2.2 Multiferroics

Multiferroics are expected to show large magnetoelectric effects, which have become clear in the last section. In this section, there will be first a general introduction to multiferroics. This is followed by a classification of them. Furthermore, the strength of magnetoelectric coupling and ferroic properties in each class will be discussed.

The first definition of multiferroic materials was given by Hans Schmid [8]. He stated that a material is called multiferroic, if there are two or more primary ferroic order parameters present in one phase of the material. Within the framework of primary order parameters, he listed ferroelectricity, ferromagnetism, ferroelasticity and ferrotoroidicity. The definition is very strict, and consequently systems with antiferromagnetic/electric and ferrimagnetic/electric order were not included. Nowadays all materials will be accepted to be multiferroic, if they show any kind of long-range magnetic and electric ordering, but nevertheless so far a clear definition of multiferroics is not made. Thus in the following all materials exhibiting kind of a long-range magnetic and a long-range electric ordering are considered as multiferroic. Ferroelasticity and ferrotoroidicity can also be considered in a general definition but are skipped here because of the focus of the work on ferroelectric and ferromagnetic interfaces.

Multiferroics may be classified due to the mechanism leading to the appearance of both order parameters. In 2009 Khomskii [52] reviewed multiferroics with the result of a classification. He distinguished between two types of multiferroics. The first are the Type I multiferroics, which are materials that exhibit two independent order parameters. In these materials, the polarization and magnetization are independent from each other. The second are the Type II multiferroics, which have only one independent order parameter that induces a second one. Recently, Fiebig called the first type of multiferroics split- order parameter (Type I) and the second joint- order parameter (Type II) multiferroics. However, in the following the definition of Khomskii is used but with an additional class of component multiferroics. The necessity of the introduction of a third class will become clear later.

The appearance of both ferromagnetism and ferroelectricity in one phase requires certain symmetries of the crystal structure. They can be obtained by group theory of magnetic point groups. Following Landau and Lifschitz [19] a material can only be ferroelectric if its point group includes no inversion symmetry. Only 31 of all point groups fulfill this requirement and thus allow the existence of ferroelectric behavior [10, 53]. Ferromagnetism is only possible in the absence of the time-reversal symmetry. This is the case in 31 of the 122 Shubnikov magnetic point groups. The joint set of both consists of 13 point groups that allow the appearance of a ferroelectric polarization and ferromagnetic magnetization. These simple symmetry considerations show already that multiferroic behavior is nothing common.

Another important fact is that the mechanism causing ferroelectricity and ferromagnetism are contraindicated [10]. The problem is that ferroelectricity can only show up in electric insulators, whereas ferromagnetism is likely to appear in metals. The latter is obvious from the Stoner criterion (2.1.4). Consequently, multiferroics often show ferrimagnetic

and antiferromagnetic magnetic ordering, which is likely to appear in insulators. For ferroelectricity, the inverse issue exists. The structural distortion which ferroelectrics undergo (section 2.3), requires close shell atoms. Consequently, the cations have to be in a d^0 state, that makes magnetism unlikely to appear. The rareness of multiferroics originates from these facts. Nevertheless, there are workarounds for these issues that are mainly based on the search for alternative mechanisms for ferroelectricity.

Type I multiferroics

In Type I multiferroics two order parameters exist independently of each other. Due to that, magnetization and polarization have two different transition temperatures. Some examples of Type I multiferroics are shown in figure 2.8 and 2.9. The simplest Type I multiferroic is a mixed compound consisting of two ferroic materials with a compatible crystal structure. Alternatively, it is possible to dope a ferroelectric with magnetic ions. The resulting compound consists of a randomly patterned lattice with different units as shown in figure 2.8 (a). The main difficulty in these compounds is beside the synthesis to reach a large coupling between the ferroic subsystems.

Another approach is the usage of lone pairs of a cation to create ferroelectricity in a compound. As mentioned in section (2.1.2) lone pairs are unbound stereo chemically active s^2 electrons which favor a non-central charge density distribution. In $BiFeO_3$ [54] a cation with lone pairs on the A site is combined with a magnetic ion on the B site (figure 2.8 (b)). The lone pairs cause hybridization between the Bi $6p$ orbitals and the oxygen $2p$ orbitals, which drives the ferroelectricity. The same mechanism is present in $PbVO_3$. Since the magnetic interaction in these compounds is mainly through superexchange between magnetic ions with an interstitial oxygen, the magnetic ordering is antiferromagnetic or ferrimagnetic.

A third possibility is inversion symmetry breaking by charge ordering. In electrical insulating materials a variety of mechanisms [55] can cause that at least two cations have different valences. Charge ordering is accompanied by a distortion of the lattice. For example in $LuFe_2O_4$ the iron layers are charge ordered with alternating Fe^{3+}:Fe^{2+} valence

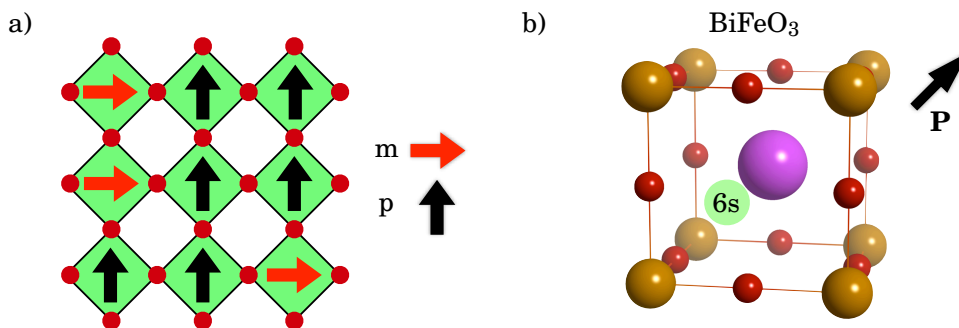**FIGURE 2.8:** Different realizations of a type I multiferroic. In (a) a mixed compound and in (b) the lone pair multiferroics are illustrated.

a) $LuFe_2O_4$ b) $YMnO_3$

$Fe^{2+} Fe^{3+}$

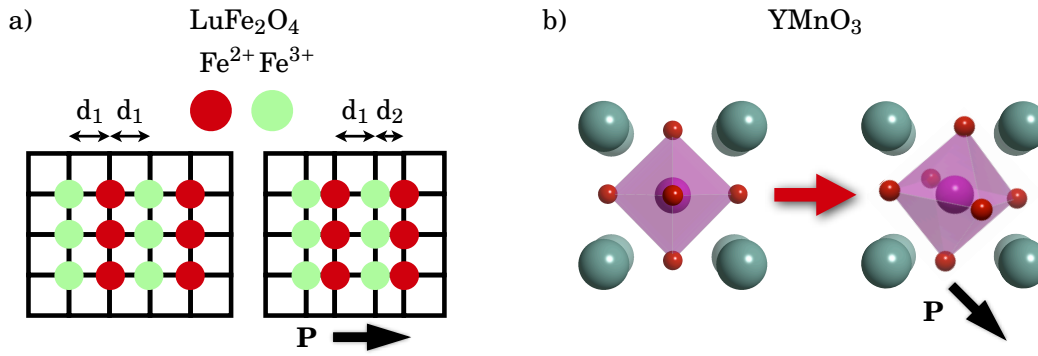d_1 d_1 d_1 d_2

P

P

FIGURE 2.9: Different realizations of a Type I multiferroic. In (a) and (b) charge ordering and geometrical multiferroics are shown.

(figure 2.9 (a)) and mutual shifted. The differently charged layers and the shift create a spontaneous polarization. However, the magnetic order in these materials is likely antiferromagnetic.

The last example for Type I are the geometrically driven multiferroics. In these materials, a distortion takes place that optimizes the space filling in the lattice. This is identical to the geometrically driven ferroelectrics. A famous example of this class is $YMnO_3$ [56], where the Mn atom is situated in a fivefold coordination between the oxygens. The MnO_5 cluster tilts below the transition temperature to achieve a closer packing (figure 2.9 (b)). Y displaces simultaneously and thereby breaks inversion symmetry. This process creates a spontaneous polarization that is mainly dominated by the dipolar Y-O pairs. The magnetic ordering is as well antiferromagnetic in this compound.

Type II multiferroics

In Type II multiferroic the magnetic ordering induces the electric polarization. The inversion symmetry is broken by a particular kind of magnetic ordering [6]. Hence, the ferroelectric and magnetic ordering appears simultaneously at a same transition temperature. Two general mechanisms are responsible for driving such a multiferroic. The first is a particular type of magnetic spiral, whereas the second one is a special type of collinear magnetic ordering.

The most known Type II multiferroics belong to the spin-spiral subclass. Magnetic spirals often appear in systems with magnetic frustration. The appearance of a polarization due to a spin spiral was observed first in $TbMnO_3$ [6]. There are two magnetic phase transitions in $TbMnO_3$, the first one at T_{N_1}=42 K and the second below T_{N_2}=28 K. The magnetic structure in the first phase is a sinusoidal spin-density wave as illustrated in figure 2.10 (a), where all moments are aligned along a specific direction but with different moments. The electric polarization appears at the second phase transition. The lowering of the temperature changes the magnetic structure towards a cycloidal spiral as shown in 2.10 (b). The cycloidal spiral has no inversion center and thus breaks the inversion symmetry of the system (figure 2.10 (b)). Mostovoy [57] found out within a phenomenological approach that
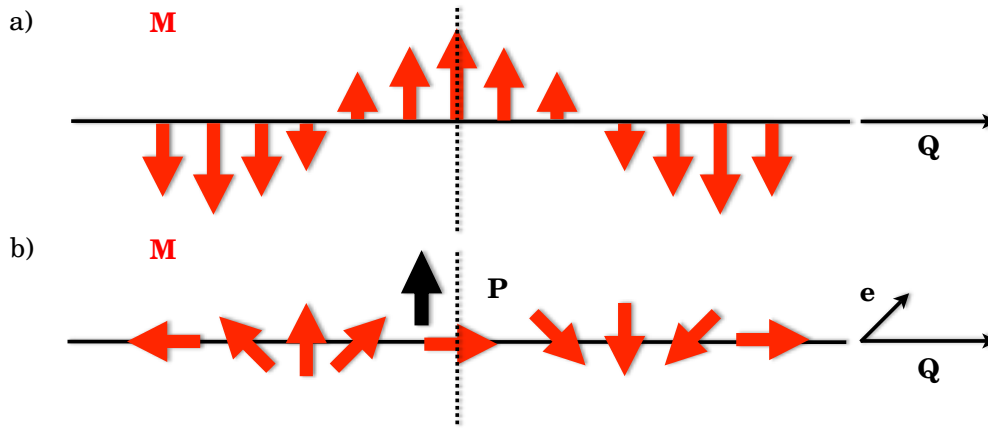
FIGURE 2.10: The figure shows the two types of spin spirals. In (a) a sinusoidal spin wave is illustrated, where the spins differ in magnitude but point along one certain direction. In (b) a cycloidal spin spiral is shown, which has no inversion center and causes an electric polarization in $TbMnO_3$.

due to a cycloidal spiral an electric polarization can appear which is directed along,

$$\mathbf{P} \sim \mathbf{r_{ij}} \times [\mathbf{S_i} \times \mathbf{S_j}] \sim [\mathbf{Q} \times \mathbf{e}] \ . \tag{2.23}$$

r_{ij} is the vector connecting neighboring spins S_i and S_j. Alternatively, the spiral can be described by a wave vector Q and a vector $\mathbf{e} \sim [\mathbf{S}_i \times \mathbf{S}_j]$ which is the spin rotation axis. The microscopic mechanism that drives the polarization in these systems is the spin-orbit coupling and the Dzyaloshinskii-Moriya [48,58] interaction. Interestingly, in these systems the polarization can easily be switched by a magnetic field. For example, if a magnetic field perpendicular to **e** is applied, the spin spiral will rotate until all sub-lattice moments are within a plane perpendicular to the field. The exchange energy is minimized in this alignment. Due to the rotation of the spin spiral the polarization rotates as well, which is a large magnetoelectric effect.

The second subclass consists of materials whose collinear magnetic order causes ferroelectricity like in Ca_3CoMnO_6 [59]. The breaking of inversion symmetry is due to exchange striction. The simplest example for such a system is a one-dimensional chain of alternating magnetic atoms, like in Ca_3CoMnO_6. Along the chain spins align in a ↑↑↓↓ arrangement. The exchange striction causes an imbalance between ferro- (↑↑) and antiferromagnetic (↑↓) bonds. Thus the system becomes distorted and the resulting structure is similar to the example shown in figure 2.9 (b). The origin of the exchange striction is a result of the different valency of the transition metal ions. Sometimes this kind of multiferroic is referred to as charge ordered multiferroics.

Two component multiferroics

If the ferroic properties and the magnetoelectric coupling, in Type I and II multiferroics, are considered, a general issue becomes obvious. Type I multiferroics exhibit good ferroelec-
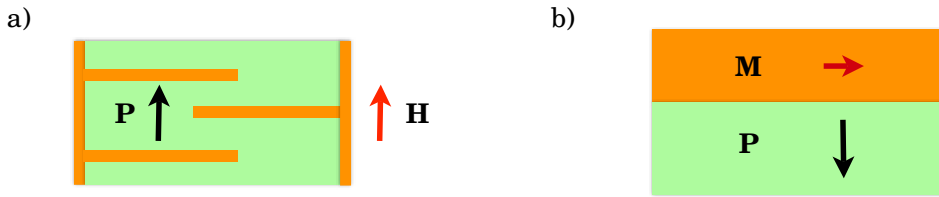
FIGURE 2.11: Possible realization of biferroic interfaces. (a) a ferroelectric film (green) embedded in a metallic system. (b) combination of a ferroelectric and ferromagnet in a layered structure.

tric properties but a rather poor magnetoelectric coupling. Type II multiferroics show the inverse problem. They exhibit a large coupling but poor ferroelectric properties. This problem can be bypassed by considering two-component multiferroics. They are a third type of multiferroics and similar to 2.8 (a) the mixed compounds.

The idea is to combine ferroelectric and ferromagnetic materials in such a way that each component still keeps its ferroic properties. In contrary to Type I multiferroics the combination takes place on a different length scale. In the Type I multiferroics the mixing is on the sub nm scale, whereas in the component multiferroics the scale is in the nm range. Thus, they are borderline cases of Type I multiferroics. In figure 2.2.2 (a) and (b) two examples of two-component multiferroics are illustrated [15, 60]. The first is an embedded ferroelectric within a magnet (a), whereas the second one is a superlattice structure. The main advantage of these multiferroics is that both components remain in their natural state. Consequently, there is no need for new mechanisms for ferroelectricity or ferromagnetism. Furthermore, there is a large degree of freedom to tune each ferroic component to gain a large magnetoelectric coupling.

However, there are also some difficulties to be faced for these compounds. For example, depending on the growth process chemical reactions at the interface may take place and cause a magnetic or ferroelectric dead layer. This obstacle can be avoided by deposition of an additional interface layer between both components [7].

The two examples illustrated in figure 2.11 (a) and (b) have been experimentally investigated. In figure 2.12 (a) and (b) the findings for the magnetoelectric coupling are shown. For (a) $BaTiO_3$ has been embedded within Ni electrodes. The application of a magnetic field causes a strain in the Ni electrodes, because of magnetostriction, which is transferred to $BaTiO_3$ and changes the polarization. Consequently, the voltage axis in figure 2.12 (a) shows the change of the electric polarization. Obviously, the magnetoelectric coupling is different if the magnetic field is applied to the easy and hard magnetic axis of Ni. The largest obtained magnetoelectric coupling coefficient is about $\alpha = 7$ mV/T, which is in the range of the Cr_2O_3 result, the first magnetoelectric. If the right composition is chosen like a sandwich structure of Terfenol-D and single-crystal $Pb(Mg,Nb)O_3$-$PbTiO_3$ for example, $\alpha=7000$ mV/T [61] can be obtained. This shows the large variation that is possible within these systems.
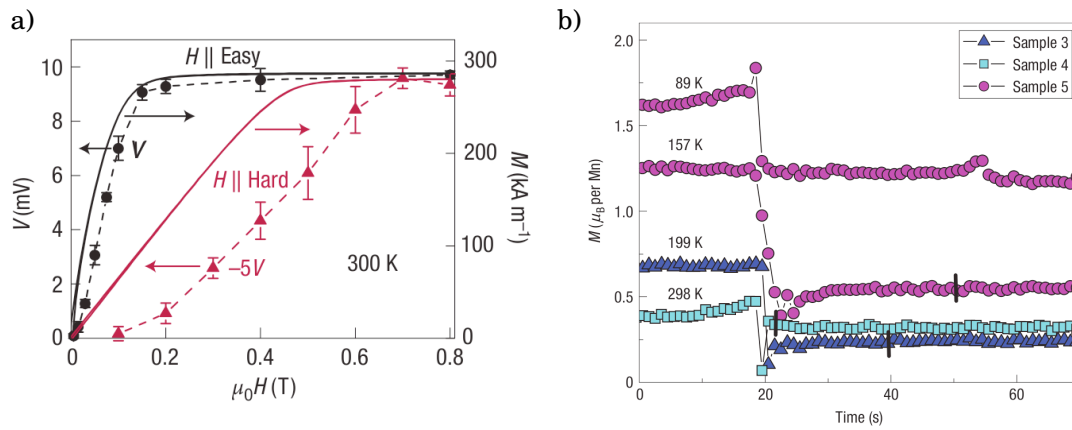
FIGURE 2.12: Experimental results for measurements of the magnetoelectric coupling for the two-component multiferroics are shown in figure 2.11 (a) and (b). The figures were taken from the articles of Isreal et al. [60] and Eerenstein et al. [15].

The example shown in figure 2.11 (b) was measured on a system consisting of a $BaTiO_3$ substrate covered with a ferromagnetic film of $La_{0.67}Sr_{0.33}MnO_3$. In the figure, the magnetoelectric response to an applied electric field is shown. The electric field was ramped, thus the time on the x-axis corresponds to the field strength. Depending on the temperature certain drops of the magnetization of $La_{0.67}Sr_{0.33}MnO_3$ are observed. They indicate that at such an interface magnetoelectric coupling occurs. Most probably, the coupling in this system is due to strain. Unfortunately, it was not possible to determine if the direction of the magnetization changed, too.

Consequently, theoretical calculations can reveal some properties that were not possible to obtain experimentally. The basis of these calculations will be discussed in the next chapter.

ELECTRONIC STRUCTURE

In this chapter, the theoretical background for the methods used in the calculations of the electronic structure will be introduced. Their presentation is organized in two parts. In the first part the pathway from the many-body problem to the density-functional theory and the associated approximations are shown. The second part focuses to the special methods that were applied, mainly based on a plane waves basis set, pseudo potentials and the projector-augmented-plane-wave-method (**PAW**).

3.1 Many-particle problem

The many-particle problem in condensed matter physics consists of solving the Schrödinger equation for a solid

$$H\Phi(\mathbf{r},\mathbf{R}) = E\Phi(\mathbf{r},\mathbf{R}). \tag{3.1}$$

In general, the wavefunction of the system depends on all coordinates of the nuclei and electrons,

$$\mathbf{r} \equiv \{\mathbf{r}_1,...,\mathbf{r}_{N_e}\}, \tag{3.2}$$

$$\mathbf{R} \equiv \{\mathbf{R}_1,...,\mathbf{R}_{N_n}\}, \tag{3.3}$$

where the associated Hamilton operator contains the following contributions

$$
\begin{aligned}
H \quad = \quad & T_n(\mathbf{R}) + V_{nn}(\mathbf{R}) + T_e(\mathbf{r}) + V_{ee}(\mathbf{r}) + V_{en}(\mathbf{r},\mathbf{R}) \\
& T_n \text{ kinetic energy of the cores,} \\
& T_e \text{ kinetic energy of the electrons,} \\
& V_{nn} \text{ core-core Coulomb repulsion,} \\
& V_{ee} \text{ electron-electron Coloumb repulsion,} \\
& V_{en} \text{ electron-core Coloumb attraction.}
\end{aligned}
\tag{3.4}
$$

To estimate the size of the problem, one can consider the number of particles in a solid, which is about $N \approx 10^{23}$ per cm^3. Hence, the wavefunction depends on the same number

of coordinates which makes it impossible to solve equation (3.1) analytically or numerically. However, approximations reduce the problem size and eventually allow a solution. The first step is the Born-Oppenheimer approximation [62]. It splits equation (3.1) into two sets of equations, one for the nuclei and one for the electrons in the potential of the nuclei.

3.1.1 Born-Oppenheimer approximation

The Born Oppenheimer approximation relies on the fact that the masses of an electron and a nucleus differ by three orders of magnitude. Owing to this difference, Born and Oppenheimer [62] showed that the total wavefunction of the system can be separated into two parts by considering the product *ansatz*

$$\Phi(\mathbf{r}, \mathbf{R}) = \psi(\mathbf{r}, \mathbf{R})\zeta(\mathbf{R}). \tag{3.5}$$

It results in two equations,

$$H_e \psi(\mathbf{r}) = [T_e + V_{ee} + V_{en}]\psi(\mathbf{r}) = E_e(\mathbf{R})\psi(\mathbf{r}) \tag{3.6}$$

$$H_n \zeta(\mathbf{R}) = [T_n + V_{nn} + \epsilon_e(\mathbf{R})]\zeta(\mathbf{R}) = E\zeta(\mathbf{R}). \tag{3.7}$$

The energy $\epsilon_e(\mathbf{R})$ is the total energy of the electron cloud for the nuclei configuration $\mathbf{R}$, whereas E is the total energy. Properties of the electron system are obtained by (3.6) in which the nucleus position enter as parameters. The total energy can be calculated from (3.7) allowing the investigation of nuclei motions and thereby structural optimization.

So far not much was gained by the approximation since the equation for the electron system (3.6) still contains the huge number of $3N_e$ degrees of freedom.

3.1.2 Density functional theory

A convenient way to solve equation (3.6) is the mapping onto an effective single-particle problem. This is done in Density-functional-theory (**DFT**). The idea goes back to Thomas and Fermi [63, 64], who suggested to use the electron density instead of the many-electron wavefunction. However, it took almost forty years until Hohenberg und Kohn [16, 17] found a convenient solution to do so. DFT is based on the theorems of Hohenberg and Kohn. The first states that the ground state energy is a unique functional of the ground-state density $n_0(\mathbf{r})$:

$$E_0 = E(n_0(\mathbf{r})) \qquad n(\mathbf{r}) = \langle \psi \mid \sum_i \delta(\mathbf{r} - \mathbf{r_i}) \mid \psi \rangle. \tag{3.8}$$

Furthermore, the potential V_{en} of the cores determines the ground-state density. Thus, two different external potentials will not give the same ground state density unless they differ only by a constant. Consequently, the ground-state energy can be obtained by varying the density according to the Ritz method

$$E_0 = E(n_0(\mathbf{r})) \le E(n(\mathbf{r})). \tag{3.9}$$

If the variation of the energy with respect to the density vanishes,

$$\delta E(n(\mathbf{r})) = 0, \tag{3.10}$$

the minimum of the energy is found.

At this point, the remaining task is to find the unknown dependence of the energy on the density. The Hamiltonian of the electron system (3.6) can be decomposed as follows

$$E(n(\mathbf{r})) = T_e(n(\mathbf{r})) + V_{en}(n(\mathbf{r})) + V_{ee}(n(\mathbf{r})), \tag{3.11}$$

or explicitly

$$T_e(n(\mathbf{r})) = \langle \psi \mid \sum_{i=1}^{N_e} \frac{p_i^2}{2m_e} \mid \psi \rangle, \tag{3.12}$$

$$V_{en}(n(\mathbf{r})) = \langle \psi \mid \frac{1}{4\pi\epsilon_0} \sum_{i}^{N_e} \sum_{I}^{N_n} \frac{-Z_I e}{|\mathbf{R}_I - \mathbf{r}_i|} \mid \psi \rangle \tag{3.13}$$

$$= \int d\mathbf{r} V(\mathbf{r}) n(\mathbf{r}), \tag{3.14}$$

$$V_{ee}(n(\mathbf{r}) = \langle \psi \mid \frac{1}{4\pi\epsilon_0} \sum_{i=1}^{N_e} \sum_{j=1, j\neq i}^{N_e} \frac{e^2}{|\mathbf{r}_i - \mathbf{r}_j|} \mid \psi \rangle. \tag{3.15}$$

To shorten the equations the potential of the cores is substituted with $V(\mathbf{r})$. The explicit functional dependence on the density is known only for the contribution of the cores. For the kinetic energy of the electrons and the electron-electron interaction it is necessary to make an *ansatz*. Kohn and Sham [65] suggested to consider the electron density to be produced by noninteracting electrons,

$$n(\mathbf{r}) = \sum_{i}^{N_e} |\psi_i(\mathbf{r})|^2, \tag{3.16}$$

with ψ_i a single-particle wavefunction. Hence, the functional for the kinetic energy,

$$T_e(n(\mathbf{r})) = \sum_{i}^{N_e} \langle \psi \mid \frac{p_i^2}{2m_e} \mid \psi \rangle + T_{xc}, \tag{3.17}$$

separates into a non-interacting and an interacting part, called exchange-correlation part T_{xc}. It contains all exchange and correlation effects. The electron-electron potential is,

$$V_{ee}(n(\mathbf{r})) = \frac{e^2}{2} \int d\mathbf{r} \int d\mathbf{r} \frac{n(\mathbf{r})n(\mathbf{r}')}{|\mathbf{r} - \mathbf{r}'|} + V_{xc}, \tag{3.18}$$

separated as well to a Hartree term and an unknown second term, that likewise accounts for exchange-correlation effects. The variation of ψ_i with respect to the constraint that the wavefunctions are normalized,

$$\int d\mathbf{r}\, n(\mathbf{r}) - N_e = \sum_{i=1}^{N_e} \left[\int d\mathbf{r} |\psi_i(\mathbf{r})|^2 - 1 \right] = 0 \tag{3.19}$$

leads to the Kohn-Sham equations:

$$\left(-\frac{\hbar^2}{2m_e} \nabla^2 + V_{eff}(\mathbf{r}) \right) \psi_i(\mathbf{r}) = \epsilon_i \psi_i(\mathbf{r}) \tag{3.20}$$

$$V_{eff}(\mathbf{r}) = V(\mathbf{r}) + \int d\mathbf{r} \frac{e^2 n(\mathbf{r}')}{|\mathbf{r} - \mathbf{r}'|} + \frac{\delta E_{xc}(n(\mathbf{r}))}{\delta n(\mathbf{r})} \tag{3.21}$$
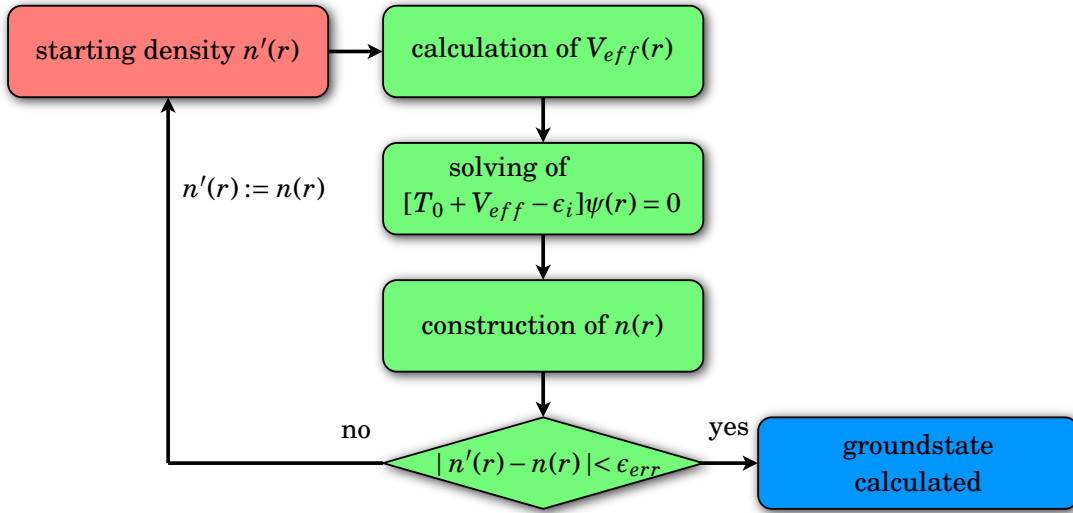
FIGURE 3.1: Scheme of the iterative solution of the Kohn-Sham equations

The energy E_{xc} consists of the exchange-correlation of the kinetic and the potential energy. Furthermore the ϵ_i are the single-particle energies which are related to E_e by

$$E_e = \sum_i \epsilon_i \quad . \tag{3.22}$$

Obviously, equation (3.20) is a single particle Schrödinger equation.

Finally, the many-body problem was projected onto a single-particle problem. A solution of the Kohn-Sham equations is found by iteration, with a scheme depicted in figure 3.1. However there are two tasks left. The first is the extension of DFT to spin-polarized systems and the second is to find an approximation for the unknown exchange-correlation potential. Both problems are discussed in the following. After that, the solution of the Kohn-Sham equation by using a plane-waves basis will be the topic of section 3.2

3.1.3 Spin-density functional theory

The equations derived in the last section can be extended to spin-polarized cases. This is required for magnetic systems, where the spin-degeneracy of the electronic states is lifted. The extension is done by decomposing the total charge density as,

$$n(\mathbf{r}) = n^{\uparrow}(\mathbf{r}) + n^{\downarrow}(\mathbf{r}), \tag{3.23}$$

where $n^{\uparrow}(\mathbf{r})$ is the density of the majority electrons and $n^{\downarrow}(\mathbf{r})$ the density of the minority electrons. This decomposition allows the introduction of a second variable,

$$m(\mathbf{r}) = n^{\uparrow}(\mathbf{r}) - n^{\downarrow}(\mathbf{r}). \tag{3.24}$$

the magnetization density. The theorem of Hohenberg and Kohn (3.9) now reads as the spin-density functional theorem [66]

$$E_0 = E\left(n_0^{\uparrow}(\mathbf{r}), n_0^{\downarrow}(\mathbf{r})\right) \le E\left(n^{\uparrow}(\mathbf{r}), n^{\downarrow}(\mathbf{r})\right). \tag{3.25}$$

As in the latter section, the variation of the spin-dependent wavefunction ψ_i^σ with the spin index $\sigma = (\uparrow, \downarrow)$, and the constraint that the wavefunctions are normalized lead to the Kohn-Sham equations:

$$\left(-\frac{\hbar^2}{2m_e}\nabla^2 + V_{eff}^\sigma(\mathbf{r})\right)\psi_i^\sigma(\mathbf{r}) = \epsilon_i^\sigma \psi_i^\sigma(\mathbf{r}),\qquad(3.26)$$

with a new spin-dependent effective potential

$$V_{eff}^\sigma(\mathbf{r}) = V(\mathbf{r}) + \int d\mathbf{r}\frac{e^2 n(\mathbf{r}')}{|\mathbf{r}-\mathbf{r}'|} + \frac{\delta E_{xc}(n^\uparrow(\mathbf{r}), n^\downarrow(\mathbf{r}))}{\delta n^\sigma(\mathbf{r})}.\qquad(3.27)$$

The equation (3.23) implies that there is a global magnetization axis for the whole system. This is a collinear treatment of the magnetization. Nevertheless, there is also an extension towards non-collinear magnetism [67, 68]. In non-collinear magnetism, any magnetic moment has its own magnetization axis and thus can point in any direction. Since the system under consideration in this work exhibits only collinear magnetism, the discussion is restricted to this case.

3.1.4 Exchange-correlation potential

In principle, the Kohn-Sham equations are exact within the framework of the adiabatic approximation. However, the form of the exchange-correlation potential is unknown. Thus, one has to rely on approximations for this part. The most often used is the local density approximation (**LDA**) or in the spin-polarized case, the local spin-density approximation (**LSDA**). In the LDA it is assumed that the exchange correlation energy depends only on a local density. By considering the uniform electron gas the functional can be obtained and has the form,

$$E_{xc}(n(\mathbf{r})) = -\frac{3e^2}{4\pi}(3\pi^2)^{\frac{1}{3}}\int d\mathbf{r}(n(\mathbf{r}))^{\frac{4}{3}}.\qquad(3.28)$$

Nowadays there exist advanced approaches, that may be used within the LDA for E_{xc}. They are found either on an empirical basis or by quantum Monte Carlo simulations [66, 69–73].

There are also extensions to the LDA. They are sometimes necessary, since LDA only gives reliable results under special conditions, in which the density varies slowly in space. If the density is far from homogeneous, the first derivative of the density has to be taken into account. This is done in the generalized gradient approximation [74] (**GGA**). Another issue of LDA is the fact that the functional contains the unphysical interaction of an electron with itself. Due to that, the electron may become delocalized. To overcome this problem an improved treatment of correlation effects is needed. One possibility is the LDA+U method, where the parameter U is used to localize certain atomic orbitals. This allows in some cases to obtain the band gaps as compared with experiment [75]. Unfortunately, LDA+U is not parameter free because of U. Another extension is the self-interaction correction (**SIC**), which is parameter free. In this method, the choice of localized orbitals is due to energy minimization [76] .

3.2 Plane Waves

Although, the many-body problem has been simplified to a set of single-particle equations, the remaining problem is to solve equation (3.9) for an extended or infinite system numerically. Considering the system to be generated by cells that are periodically repeated in all spatial directions does an intuitive simplification. Thus, the problem is reduced to the solution in a single unit cell.

In the following, way the periodicity may be involved. The effective potential in the Kohn-Sham equations is a lattice periodic function of $V_{eff}(\mathbf{r} + \mathbf{T}) = V_{eff}(\mathbf{r})$ for any lattice vectors $\mathbf{T}$. Hence, it can be expanded in a Fourier series,

$$V_{eff}(\mathbf{r}) = \sum_{\mathbf{G}} V_{eff}(\mathbf{G}) e^{\iota \mathbf{G} \cdot \mathbf{r}} \quad , \quad V_{eff}(\mathbf{G}) = \frac{1}{\Omega_e} \int_{\Omega_e} V_{eff}(\mathbf{r}) e^{-\iota \mathbf{G} \cdot \mathbf{r}} d\mathbf{r}, \tag{3.29}$$

where Ω_e denotes the unit cell volume and $\mathbf{G}$ a reciprocal lattice vector. The same can be done for the density. Secondly, the wavefunction is considered in a repeated unit cell. In a periodic potential a wavevector $\mathbf{k}$ can be assigned to each wavefunction $\psi(\mathbf{r})$ that hold

$$\psi(\mathbf{r} + \mathbf{T}) = e^{\iota \mathbf{k} \cdot \mathbf{T}} \psi(\mathbf{r}) \tag{3.30}$$

for every lattice vector $\mathbf{T}$. This is known as Bloch's theorem. Alternatively, the above statement can be written in the following way. All eigenfunctions $\psi_{\mathbf{k},v}$ of a single-particle Schrödinger equation within a periodic potential are composed as

$$\psi_{\mathbf{k},v}(\mathbf{r}) = u_{\mathbf{k},v}(\mathbf{r}) e^{\iota \mathbf{k} \cdot \mathbf{r}}, \tag{3.31}$$

where $u_{\mathbf{k},v}(\mathbf{r})$ is a lattice-periodic function. Due to the periodicity of $\psi_{\mathbf{k},v}$, it can be expanded into plane waves and, the wavefunction is given by

$$\psi_{\mathbf{k},v}(\mathbf{r}) = \sum_{\mathbf{G}} c_{\mathbf{k},v} e^{\iota(\mathbf{k}+\mathbf{G}) \cdot \mathbf{r}}. \tag{3.32}$$

The usage of equations (3.31), (3.29) and the Fourier transformation of the momentum operator allows to obtain the Schrödinger equation in reciprocal space,

$$\sum_{\mathbf{G}'} \left(\frac{\hbar^2}{2m_e} |\mathbf{k} + \mathbf{G}|^2 \delta_{\mathbf{G}\mathbf{G}'} + V_{eff}(\mathbf{G} - \mathbf{G}') \right) c_{v,\mathbf{k}+\mathbf{G}} = \epsilon_v(\mathbf{k}) c_{v,\mathbf{k}+\mathbf{G}}. \tag{3.33}$$

At this point, a numerical solution of the equation is impossible since the sum runs to infinit. Consequently, in practical calculations the Fourier expansion has to be done on a finite $\mathbf{G}$ grid. A convenient criteria to estimate the number of $\mathbf{G}$ points is to take only those which belong to plane waves whose energy is less than a given value,

$$E_{kin} = \frac{\hbar}{2m_e} |\mathbf{k} + \mathbf{G}|^2 \leq E_{cut}. \tag{3.34}$$

Apart from the infinite sum, there is a second issue for the numerical solution. A proper description of core electrons by plane waves requires a large number ($>10^6$) of expansion coefficients, which makes the numerical treatment expensive. To overcome this problem the core electrons may be handled differently, than the valence electrons. A possibility to do so is the pseudopotential approach, which will be introduced in the next section.

3.2.1 Pseudopotentials

Pseudopotential theory relies on the fact that core electrons do not take part in the chemical bonding. They are strongly localized and not affected when the atom is placed in another environment. Thus, the core electrons may be treated independently from the valence electrons.

A first step towards modern pseudopoentials is the frozen-core approximation. By solving the Schrödinger equation for the isolated atoms, the wavefunctions ψ_c and eigenenergies ϵ_c of the core electrons are obtained. These solutions are used, when placing the atom in a crystal by adding the density of the core electrons to the core potential. This procedure results in a new potential a pseudopotential [77],

$$\langle \mathbf{r} \,|\, V_{ps} \,|\, \mathbf{r}' \rangle = V(\mathbf{r})\, \delta(\mathbf{r} - \mathbf{r}') + \sum_c (\epsilon_v - \epsilon_c) \langle \mathbf{r} \,|\, \psi_c \rangle \langle \psi_c \,|\, \mathbf{r}' \rangle. \tag{3.35}$$

The use of $V_{ps}(\mathbf{r})$ instead of $V(\mathbf{r})$ has two advantages. First, the potential becomes smoother since the divergent Coulomb potential at the cores is removed. Secondly, only valence electrons have to be considered, and consequently less eigenstates to be calculated. Due to that, the energy range becomes smaller, since the very low-lying core electrons are removed. However, if the potential is replaced by a pseudopoential, it will become non-local which is obvious from equation (3.35). Thus, the calculation of some quantities may become expensive. Furthermore, the pseudopotenial (3.35) already contains the valence energy ϵ_v which has to be computed. Nevertheless, the frozen core approximation reduces the numerical cost of the solution of the Kohn-Sham equations. Although, the valence wavefunctions maintain their nodal structure because they have to be orthogonal to the core states, which requires a large $|\mathbf{G}|$-cut off. Therefore, it is much more practical to replace directly the ionic core potential by a pseudopotential that leads to node-less valence wavefunctions.

The basis for this is the logarithmic derivative

$$L_l(\epsilon) = \left. \frac{d}{dr} ln \Phi_l(r,\epsilon) \right|_{r_c} = \frac{\Phi'_l(r_c,\epsilon)}{\Phi_l(r_c,\epsilon)} \tag{3.36}$$

and the properties of second-order differential equations. For a given energy and angular momentum, the logarithmic derivative at r_c determines the wavefunction uniquely inside and outside a sphere with radius r_c. Consequently, if the potential inside the radius r_c is manipulated in that way that $L_l(\epsilon)$ is unchanged, the wavefunction outside the sphere will not change. Thus, the all-electron (**AE**) wavefunction, consisting of core and valence electrons, inside a sphere can be substituted with a node-less pseudo-wavefunction (**PS**) under the constraint

$$\left. \frac{d}{dr} ln \Phi_l^{PS}(r,\epsilon) \right|_{r_c} = \left. \frac{d}{dr} ln \Phi_l^{AE}(r,\epsilon) \right|_{r_c}. \tag{3.37}$$

The procedure of constructing the pseudopotential by using the logarithmic derivative is as follows. First, the AE wavefunction is calculated for an isolated atom. Then, a node-less PS wavefunction is constructed, inside a sphere with the same logarithmic derivative. For the node-less wavefunction the Schrödinger equation is inverted which is possible since

the wavefunction is node-less, and the corresponding pseudopotential calculated. The pseudopotential that is constructed by this recipe gives the same eigenvalues as the AE potential. Figure 3.2 shows an example of a pseudopotental and pseudowavefunction obtained by this way. Obviously there are many recipes for creating pseudopotentials [78–84]. However, to obtain a pseudopotential that is also transferable to another environment, certain requirements have to be fulfilled. First, the pseudopotential should reproduce the logarithmic derivative in a wide energy range. This is advantageous since an eigenstate could be shifted in energy when the atom is put in a different environment. The second requirement is that is should be norm-conserving [78]. Since, if both wavefunctions have the same norm inside a sphere, they will generate an identical electron density in the outside region as well. Another important aspect is that the function should be as smooth as possible to reduce the number of expansion coefficients. The smoothness implies a large r_c. Although, a small r_c gives good transferability. Therefore, one needs to find a compromise to fulfill both requirements. Usually an upper limit for r_c is around half the nearest-neighbor distance. Otherwise, if r_c is extended, no region for the AE wavefunction will remain. Hence, it cannot be expected that the pseudopotential leads to a accurate description of the chemical bonds between the atoms.

Nowadays, there exist two main branches of pseudopotentials. For the ultrasoft pseudopotentials of Vanderbilt [85], the norm-conservation has been relaxed for a very smooth decay of the potential. Due to that, the plane wave cutoff energy is substantially reduced in the calculation. However, the scheme of ultrasoft pseudopotentials requires the solution of a more complicated version of equation (3.9). Furthermore, the correct representation of the density is only obtained by adding artificial contributions at the lattice sites. The second branch is the PAW method to be introduced in the next section
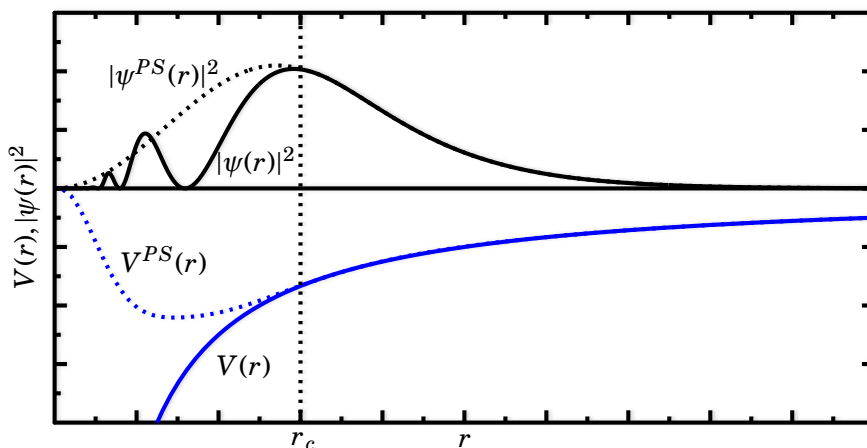

FIGURE 3.2: Difference between a pseudopotential and the corresponding wavefunction and the all-electron wavefunction.

3.2.2 Projected augmented plane waves

The projected augmented plane waves method (**PAW**) was introduced by Blöchl [18]. It is a special approach that combines pseudopotentials- with the augmented-plane-wave method (**APW**). In the PAW method a linear and invertible transformation between the real wave-function and the pseudo-wavefunction,

$$| \psi \rangle = \tau | \widetilde{\psi} \rangle, \tag{3.38}$$

is used. The transformation differs only from unity by a sum of local, atom-centered contributions $S_{\mathbf{R}}$

$$\tau = \mathbf{I} + \sum_{\mathbf{R}} S_{\mathbf{R}}, \tag{3.39}$$

where the sum runs over all atoms at sites $\mathbf{R}$. Moreover, each atom is situated in a sphere. The radius r_c of the spheres is chosen so that they are disjoint as in the muffin-tin approximation. Within r_c, the wavefunction $| \psi \rangle$ is expanded by using a set of partial waves $| \phi_i \rangle$,

$$| \psi \rangle = \sum_i | \phi_i \rangle c_i, \tag{3.40}$$

which are solutions of the isolated atom. The index i is a multi-index that refers to the atomic site $\mathbf{R}$ and to the angular momentum quantum numbers l, m. Furthermore the pseudo-wavefunction $| \widetilde{\psi} \rangle$ is expanded in the same fashion,

$$| \widetilde{\psi} \rangle = \sum_i | \widetilde{\phi}_i \rangle c_i, \tag{3.41}$$

where the pseudo-partial waves are constructed that they match $| \phi_i \rangle$ at r_c. Both partial wave sets are orthogonalized to the core states. By adding a zero to equation (3.40),

$$| \psi \rangle = | \widetilde{\psi} \rangle - \sum_i | \widetilde{\phi}_i \rangle c_i + \sum_i | \phi_i \rangle c_i \quad . \tag{3.42}$$

In comparison with equation (3.39), the $S_{\mathbf{R}}$ become

$$| \psi \rangle = | \widetilde{\psi} \rangle + \sum_i \left(| \phi_i \rangle - | \widetilde{\phi}_i \rangle \right) c_i. \tag{3.43}$$

The transformation is required to be linear. Therefore, the coefficients c_i have to be linear functions with respect to the PS wavefunction. Hence they read $c_i = \langle \widetilde{p}_i | \widetilde{\psi} \rangle$ where the auxiliary functions $\widetilde{p}_i$ are the projector functions. They have to fulfill $\sum_i | \widetilde{\phi}_i \rangle \langle p_i | = 1$ which implies that they orthogonal to the PS partial waves $\langle \widetilde{p}_i | \widetilde{\phi}_j \rangle = \delta_{ij}$. The projector functions are restricted to the augmentation region and eventually the wavefunction reads

$$| \psi \rangle = | \widetilde{\psi} \rangle + \sum_i \left(| \phi_i \rangle - | \widetilde{\phi}_i \rangle \right) \langle \widetilde{p}_i | \widetilde{\psi} \rangle. \tag{3.44}$$

Figure 3.3 shows the individual contributions of the transformation. The expectation values in the PAW method are obtained as follows

$$\langle A \rangle = \sum_n f_n \langle \psi_n | A | \psi_n \rangle = \sum_n f_n \langle \widetilde{\psi}_n | \tau^* A \tau | \widetilde{\psi}_n \rangle. \tag{3.45}$$

$$|\psi\rangle = |\widetilde{\psi}\rangle + \sum_i \left(|\phi_i\rangle - |\widetilde{\phi}_i\rangle\right)\langle\widetilde{p}_i \mid \widetilde{\psi}\rangle$$

plane wave part   true spherical part   pseudized spherical part
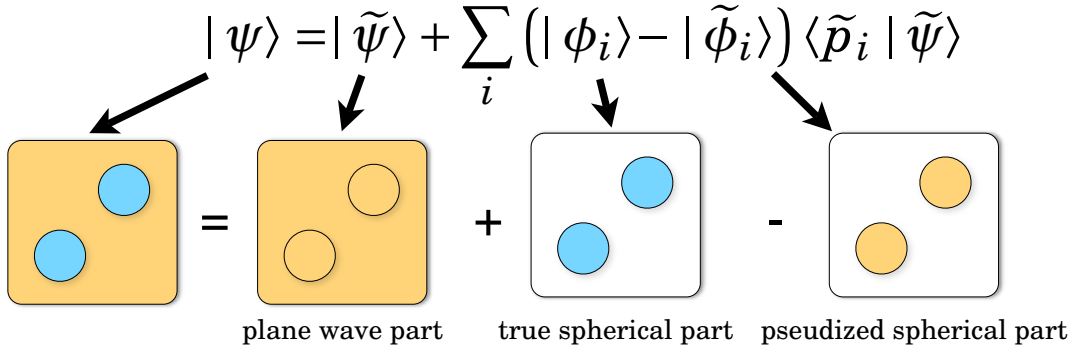
FIGURE 3.3: Composition of the wavefunction in the PAW method.

The total density and the energy read

$$n(\mathbf{r}) = \widetilde{n}(\mathbf{r}) + \sum_{\mathbf{R}} \left(n^1_{\mathbf{R}}(\mathbf{r}) - \widetilde{n}^1_{\mathbf{R}}(\mathbf{r})\right), \tag{3.46}$$

$$E = \widetilde{E} + \sum_{\mathbf{R}} \left(E^1_{\mathbf{R}} - \widetilde{E}^1_{\mathbf{R}}\right), \tag{3.47}$$

where the tilde marks soft objects obtained by pseudization, 1 is used to mark objects inside spheres and $\mathbf{R}$ are the atomic indices.

The recipe for generating a PAW pseudopotential is similar as described in the last chapter. Usually, the $|\phi_i\rangle$ are calculated for isolated atoms of a certain element by using an all-electron method. From the result of the calculation, a set of pseudo- and projectorfunctions is obtained. Finally, they are used as the pseudopotential. In principle, this procedure can be done for any element.

3.2.3 Forces and structural relaxation

The investigation of ferroelectric material requires knowledge of the equilibrium positions of the atoms. To obtain them it is necessary to calculate forces within the DFT. Forces acting on an atom γ can be calculated by

$$\mathbf{F}_\gamma = -\nabla_{\mathbf{R}_\gamma} E(\mathbf{R}_\gamma). \tag{3.48}$$

If the wavefunction $|\psi_i\rangle$ of the system is known, one obtains

$$
\begin{aligned}
\nabla_{\mathbf{R}_\gamma} E(\mathbf{R}_\gamma) &= \nabla_{\mathbf{R}_\gamma} \sum_i \langle\psi_i \mid H \mid \psi_i\rangle \tag{3.49} \\
&= \sum_i \langle\psi_i \mid \nabla_{\mathbf{R}_\gamma} H \mid \psi_i\rangle + \langle\nabla_{\mathbf{R}_\gamma}\psi_i \mid H \mid \psi_i\rangle + \langle\psi_i \mid H \mid \nabla_{\mathbf{R}_\gamma}\psi_i\rangle \\
&= \sum_i \langle\psi_i \mid \nabla_{\mathbf{R}_\gamma} H \mid \psi_i\rangle + E_i\langle\nabla_{\mathbf{R}_\gamma}\psi_i \mid \psi_i\rangle + E_i\langle\psi_i \mid \nabla_{\mathbf{R}_\gamma}\psi_i\rangle \\
&= \sum_i \langle\psi_i \mid \nabla_{\mathbf{R}_\gamma} H \mid \psi_i\rangle + E_i \underbrace{\nabla_{\mathbf{R}_\gamma}\langle\psi_i \mid \psi_i\rangle}_{=0},
\end{aligned}
$$

where the $H|\psi_i\rangle = E_i|\psi_i\rangle$ was used. The result is the Hellmann-Feynman force that reads here as

$$\mathbf{F}_\gamma = -\sum_i \langle\psi_i \mid \nabla_{\mathbf{R}_\gamma} H \mid \psi_i\rangle. \tag{3.50}$$

If the latter equation is evaluated for the Hamiltonian (3.4), all terms will cancel out except for the electron-core and core-core interactions. Hence, for the x component of the force acting on atom γ one obtains

$$F_{x_\gamma} = -Z_\gamma \left(\int d\mathbf{r} \rho(\mathbf{r}) \frac{x - X_\gamma}{|\mathbf{r} - \mathbf{R}|^3} + \sum_{\alpha \neq \gamma}^{N_n} \frac{X_\alpha - X_\gamma}{|\mathbf{R}_\alpha - \mathbf{R}_\gamma|^3} \right). \tag{3.51}$$

It is equivalent to an electric field caused by point charges at the position of the cores and a smooth distribution $\rho(\mathbf{r})$. Consequently, the calculation of the forces needs only the calculation of $\rho(\mathbf{r})$, which is done via equation (3.46). To do structural relaxation one needs to apply an iterative scheme, where in any step the forces are calculated for an alignment of the nuclei. The nuclei are then shifted with respect to directions given by the forces. This cycle is repeated until the forces are smaller than a given upper limit.

SELECTED RESULTS

In the last chapter of this work, the main results will be presented. Therefore, the important conclusions of the papers [E1,E2,E3,E4] and unpublished results are discussed from a general point of view within three parts. The first part is a short summary of the bulk properties of the considered $ATiO_3$ (A=Ba,Pb) ferroelectric materials. In this part, the properties of the clean ferroelectric surfaces [E1] will be discussed, too. The second part focuses on the magnetoelectric coupling at ferroelectric/ferromagnetic interfaces [E2,E3]. Accordingly, the magnetic order and the change of the magnetization by polarization reversal are investigated. In the last section the influence of oxygen impurities on the coupling mechanism is shown [E4].

Before discussing the results, notes on technical details of the calculations are necessary. All computations were done using the Vienna ab-initio simulation package (**VASP**) [86–88]. For some calculations the Koringa-Kohn-Rostocker method was used for crosschecking and investigation of properties, that were not accessible by VASP. The numerical parameters used in the calculation are given in the papers.

4.1 Free ferroelectric surfaces

The investigation and characterization of ferroelectric surfaces are a challenging task [89]. Their surface structures can be numerically characterized and understood by using first principle calculations. Furthermore, there are some evidences in literature [90] that the direction of the polarization **P** may affect the surface relaxation and thereby **P** at the surface. The functionality of a component multiferroic, made of a ferroelectric substrate and ferromagnetic film, depends on the reversal of **P**. Thus, it is worth to study the properties of a clean ferroelectric surface first.

The (001) surfaces of three $ATiO_3$ (A=Ba, Pb, Sr) perovskites have been investigated. The first two compounds are ferroelectric with moderate (P_{BaTiO_3}=26 $\mu C/cm^2$) and high (P_{PbTiO_3}=96 $\mu C/cm^2$) polarization values, whereas $SrTiO_3$ is a paraelectric material. Both ferroelectrics are driven by the Jahn-Teller effect, which is accompanied in $PbTiO_3$ by ac-

tive lone pairs of Pb. **P** is caused by the off-centering of the atoms from their ideal positions. This shift is characterized by the displacement $\delta = z_{oxygen} - z_{cation}$. In PbTiO$_3$ δ is about 0.3 Å for both TiO$_2$ and PbO layers and 0.08 Å for the respective layers in BaTiO$_3$. The size of the displacements reflects the values of the polarization in these materials.

There are three possible directions for **P** with respect to the (001) surface. **P** points either parallel, antiparallel or perpendicular to the surface normal. For technical application, the first two directions are significant. Furthermore, there are two distinct surface terminations that are AO and TiO$_2$. The different compounds and their terminations are modeled by supercells, that consist of 5 unit cells of ATiO$_3$ and 5 nm vacuum. An example is illustrated in figure 4.1. The two different polarization directions are mimicked by considering a positive or a negative δ of all layers. In the first case the system is denoted corresponding to the direction of **P** as P$_\downarrow$ and in the second case as P$_\uparrow$. Starting from these configurations, the topmost three layers are allowed to relax. The remaining system is kept in its bulklike optimized structure to simulate a thick ferroelectric film. Consequently, the chosen approach models polarization states of a system in remanence with no external electric field.

After structural relaxation the preferred surface termination can be deduced by using the approach of Eglitis et al. [91]. It turns out that the ferroelectric surfaces favor TiO$_2$ termination independent of the polarization direction. However, for the non-polar SrTiO$_3$ the termination with the lowest energy is SrO but the energy difference to TiO$_2$ is very small (0.02 meV). Hence, it might be expected that both terminations exist simultaneously. The obtained results for polar BaTiO$_3$ and PbTiO$_3$ agree with theoretical studies of non-polar surfaces [91]. Nevertheless, there are experimental reports [89] that in thin BaTiO$_3$ films the BaO termination is preferred. The disagreement can be explained with the chosen supercells which model thick films, whereas in the experiment thin films on SrRuO$_3$/SrTiO$_3$ (001) were studied.

The relaxed surface structure of PbTiO$_3$ is shown in figure 4.2 (a) and (b). For both directions of **P**, it is obtained that the displacement at the surface is positive. Thus in a point charge model the surface dipole points towards the bulk. For BaTiO$_3$ the same result is found. The alignment at the surface is caused by the changed coordination number of
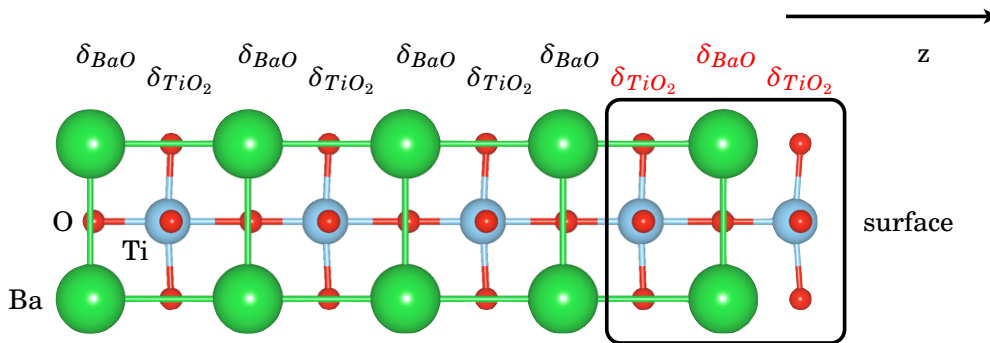

FIGURE 4.1: Illustration of a (001) TiO$_2$ terminated surface of BaTiO$_3$. The topmost layers were considered for structural relaxation.

the Ti atoms. In bulk PbTiO$_3$ (BaTiO$_3$) the Ti atom has a coordination number of six. If the length of the Ti-O bonds are considered, there is one of the two bond lengths along [001] that is rather short while another Ti-O bond in the vertical direction is significantly longer than the four other bonds stretching in the equatorial plane. If the longest Ti-O bond is excluded from the consideration using the electrostatic arguments then the environment for each Ti becomes fivefold-coordinated polyhedra. It is illustrated with isocharge lines in the lower part of figure 4.2 (a) and (b), where the Ti atoms have their nearest oxygen atom along the [00$\bar{1}$] or [001] direction, respectively. However, the nearest oxygen of the Ti atom at the surface is always along [00$\bar{1}$]. Thus, to saturate its bond Ti relaxes towards the bulk until it finds its position below the equatorial oxygens. Furthermore, in the case of P$_\uparrow$ this distortion causes a blockade of the charge transfer within the third layer, which decreases the displacement.

Further investigations showed [93] the large influence of this relaxation behavior on the ferroic properties in the surface area. By considering larger supercells, it is found that for P$_\uparrow$ polarized BaTiO$_3$ up to 24 atomic layers from the surface are needed until the bulk displacement is recovered. This large relaxation substantially decreases **P** at the surface. However, for the opposite polarization direction (P$_\downarrow$) the bulklike displacement is obtained after 4 layers. Hence, the P$_\uparrow$ state may become unfavored for BaTiO$_3$ and PbTiO$_3$ surfaces.

The next section will focus on the ferroelectric surfaces covered with Fe or Co. At these interfaces no decrease of **P** is obtained, which is due to the saturation of the Ti bond by the
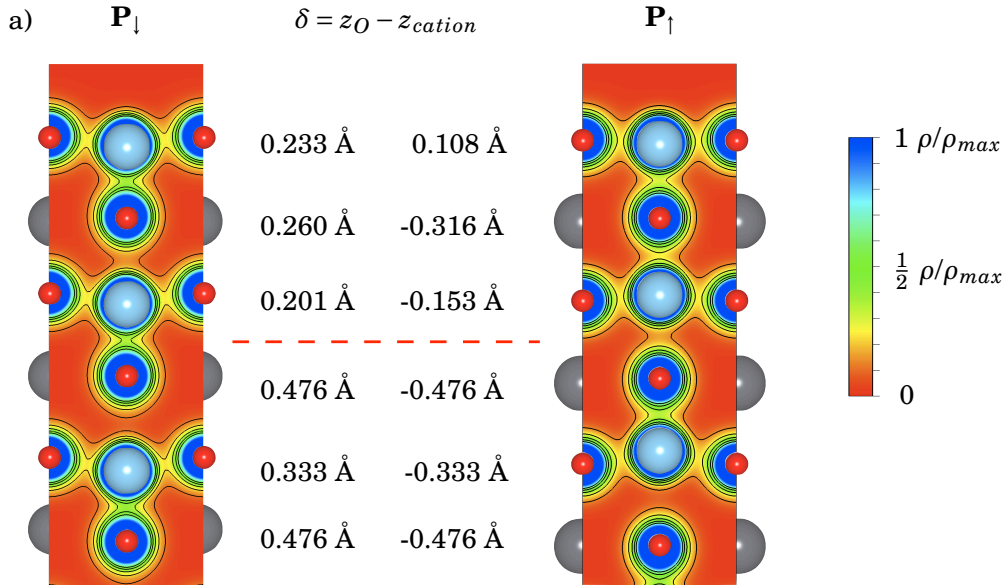

FIGURE 4.2: The charge density calculated for the top six layers of PbTiO$_3$ and projected on the x-z plane. The two polarization states P$_\downarrow$ (a) and P$_\uparrow$ (b) are shown, where the numbers in the center correspond to the displacement δ of each layer. In the case of P$_\uparrow$, the isocharge lines of the third layer from the interface show a blockade of the charge transfer along the [001] direction. The red line separates the bulklike and relaxed layers.

metal.

4.2 Magnetoelectric coupling at multiferroic interfaces

There are several experimental reports [15, 94–100] that show the existence of magnetoelectric coupling in component multiferroics. In most of these experiments a large coupling is obtained by strain engineering. However, theoretical studies [101–103] predict many other mechanisms that cause magnetoelectric coupling with the same size as strain. Hence, the investigations of the microscopic origin of the coupling give new directions for synthesizing magnetoelectric materials.

The focus here is on a multiferroic interface consisting of a ferroelectric substrate covered with a thin ferromagnetic film. A detailed look at the interface structure is shown in figure 4.3. The considered materials are a $BaTiO_3$ or $PbTiO_3$ (001) surface covered with a thin film of Fe or Co. The choice of ferromagnetic materials is based on the small lattice mismatch with the substrates, which allows epitaxial growth [104]. Furthermore, there are two possible interfaces $Fe(Co)/AO/ATiO_3$ and $Fe(Co)/TiO_2/ATiO_3$ for these materials. The comparison of the groundstate energy for both terminations shows that the $Fe(Co)/TiO_2/ATiO_3$ interface is preferred, where the Fe atoms are situated above the oxygens, as shown in 4.3 (b). This result is also in agreement with studies of superlattices [101].

The magnetoelectric coupling has been investigated by the same supercell approach as for the uncovered ferroelectric surfaces. Hence, two polarization directions $P_\uparrow$ and $P_\downarrow$ and their influence on the magnetic properties of the ferromagnet are studied.

The magnetic properties of the interfaces are shown in figure 4.4. For one monolayer (**ML**) Fe a ferromagnetic groundstate is obtained. Adding a second layer changes the magnetic ordering towards antiferrimagnetic, whereas the deposition of a third layer restores ferromagnetic ordering. The change of magnetic ordering originates in the structural relaxation at the interface. For two ML of iron the interlayer distance between the iron layers
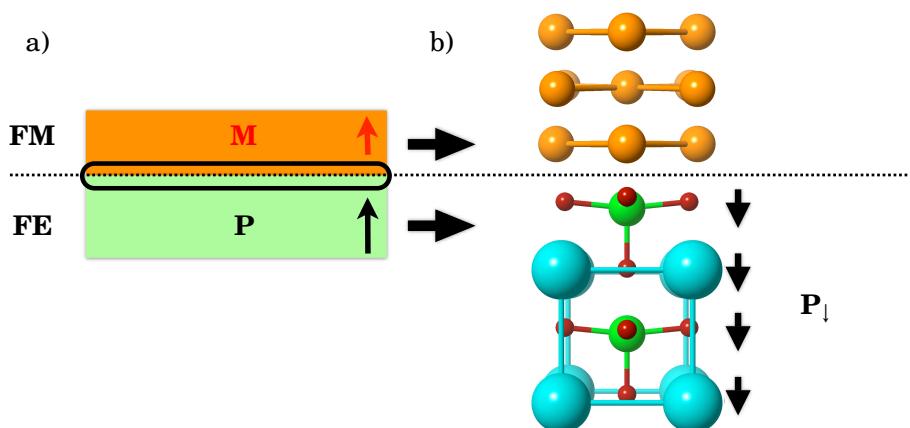

FIGURE 4.3: On the left-hand side, a general illustration of a magnetoelectric interface is presented. The right-hand side shows the realization of the interface by considering TiO_2 terminated $BaTiO_3$ covered with Fe layers.

becomes very small (about 1 Å). This compression leads to a frustrated magnetic state that consists of a ferrimagnetic layer at the interface and an antiferrimagnetic layer at the surface. For the analogous Co systems, this transition is not observed. The reason is the three times larger lattice mismatch ($\approx$10%) for Co, which hampered this transition. Furthermore, the magnetic ordering is unaffected by the polarization direction.

However, the polarization reversal causes a change of the magnetization at the interface. This is shown in the lower part of figure 4.4. For 1ML Fe on BaTiO$_3$ the change is small, whereas it is much more pronounced for PbTiO$_3$. The observed effect is due to the interaction [101] of Fe and Ti. At the interface Fe minority d-states hybridize with Ti d states, leading to an induced moment on Ti. Its size depends on the strength of hybridization, which is determined by the distance between Fe and Ti. For the two polarization directions the bond length between Ti and Fe change in Fe/BaTiO$_3$ by 0.05 Å producing the small change, whereas in Fe/PbTiO$_3$ the difference is six times larger about 0.3 Å. The same mechanism also occurs in Co/BaTiO$_3$.

Besides a change of the total magnetization, there is the possibility of a spin reorientation transition. The polarization reversal may cause a modification of the magnetic crystalline anisotropy (**MCA**). The MCA was calculated within the KKR method revealing that
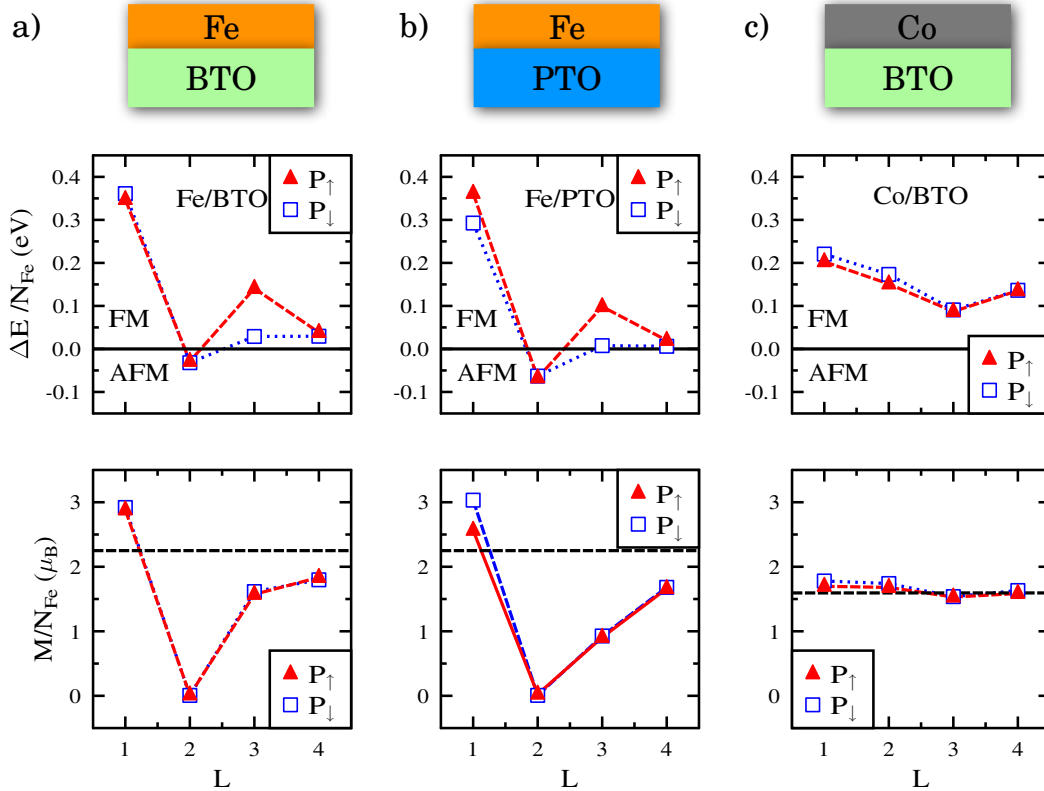

FIGURE 4.4: The upper panel shows the energy difference between a ferromagnetic and antiferrimagnetic groundstate as a function of the thickness of the ferromagnetic film in layers L. The lower panel shows the total magnetization for each thickness. In all figures, two curves are shown that correspond to the two distinct polarization directions.

out-of-plane anisotropy is always favored against in-plane anisotropy. Nevertheless, there is a net change of the absolute value of the MCA for 1 ML Fe on $BaTiO_3$, namely from 0.54 meV for $P_\uparrow$ towards 0.72 meV for $P_\downarrow$. The observed change is in agreement with other theoretical studies [92].

The analysis of the results leads to the conclusion that no control of the magnetization direction by polarization reversal is possible in these systems. However, further investigations show that already small modifications in the system with 2 ML Fe on $BaTiO_3$ allow to control the magnetic ordering by the polarization. Two different possibilities have been considered. The first is the substitution [93] of the TiO_2 layer at interface with CrO_2. This causes that for $P_\uparrow$ ferromagnetic ordering becomes favored, whereas for $P_\downarrow$ still the antiferrimagnetic ordering is present. The altering of the magnetization in this case is about 8 μ_B and thereby 8 times larger than for $Fe/PbTiO_3$. Another approach is alloying the $(Fe_2)_2/TiO_2/BaTiO_3$ with Co. The $Fe_{1-x}Co_x$ alloy was calculated by using the coherent-potential approximation [105]. The results are shown in figure 4.5. It turned out that 25 % of Co in the Fe stabilizes the ferromagnetic ordering for $P_\uparrow$ but not for $P_\downarrow$. Consequently, a change of the magnetization with a similar size as due to Cr doping is obtained.

The studies reveal new ways for large magnetoelectric coupling. However, some issues still have to be investigated, for example the influence of oxygen impurities on the ferroelectric as well as the ferromagnetic properties. A first approach will be shown in the next section.
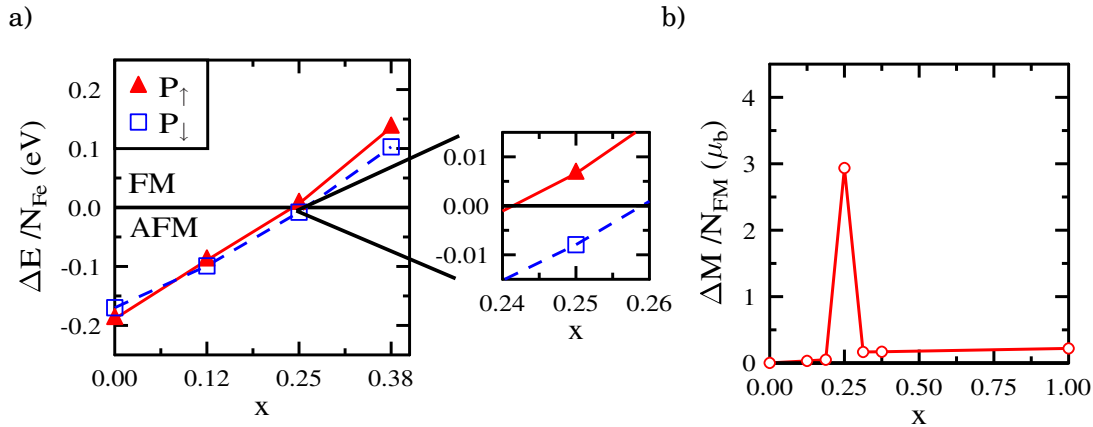

FIGURE 4.5: In (a) the energy difference for $Fe_{1-x}Co_x$ between a ferromagnetic and antiferromagnetic groundstate as a function of x is shown. The zoom reveals that for 25 % of Co a switch of the magnetic order is possible. The figure on the right-hand side shows the change of the magnetization for the whole concentration range.

4.3 Magnetoelectric coupling at O_x/Fe_x/BaTiO$_3$ interfaces

The oxidation of uncovered Fe films is unavoidable. Thus, it is necessary to investigate the influence of oxidation on the magnetoelectric coupling. To study the impact of oxygen an O_x/Fe$_2$/TiO$_2$/ATiO$_3$ ($x = 1 - 4$) interface was considered. The aims were to determine, which oxidation state is favored, as well as the expected strength of the magnetoelectric coupling. The considered oxygen concentrations $c = N(O)/N(Fe)$ range from 0.5 to 2.

To investigate the different concentrations various supercells have been considered, that are shown in figure 4.6 (a) and (b). In the case of $c = 0.5$ there is one additional oxygen, that can occupy the A, Ti or Fe site on the interface of Fe/ATiO$_3$. In the following these configurations are denoted with A, T and F, respectively. For $c = 1$ ($c = 1.5$) there are at least 4 (3) possible configurations. The largest concentration is modeled by two different settings, where either all sites (ATFF) or all interstitial sites (HO) are occupied. All twelve supercells were relaxed structurally in the same way like in the latter studies.

The comparison of the obtained groundstate energy after structural relaxation allows the determination of the favored positions of the oxygens. Figure 4.7 (a) shows the energy difference between the lowest energy configuration and all remaining ones. For $c = 0.5$ the A site is preferred. However, the oxygen on the Ti site is very close in energy, whereas the Fe site is ruled out. For higher concentrations, the positions can be deduced from the result for $c = 0.5$. Hence, in the case of $c = 1.0$ the energetically lowest configuration is the occupation of the Ti and A sites. Consequently, for $c = 1.5$ at least one Fe site has to be occupied which results in the favored configuration ATF. The highest concentrations favor the occupation
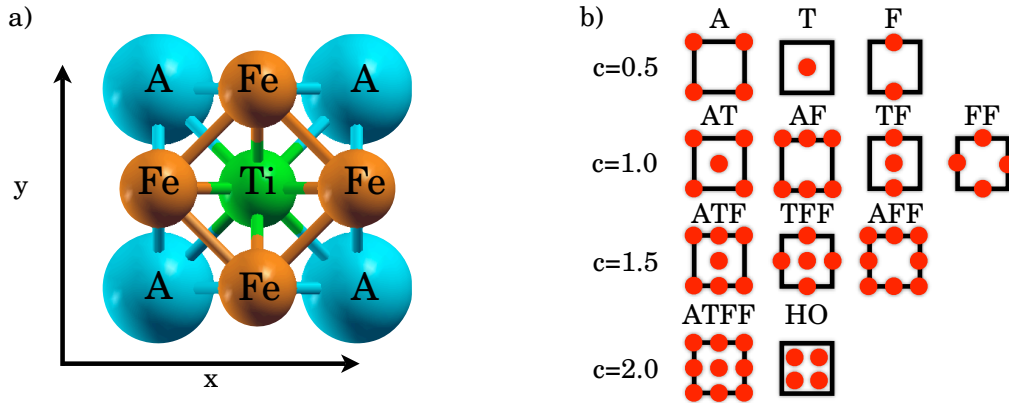

FIGURE 4.6: Unit cell of oxidized multiferroic interface O_x/Fe$_2$/TiO2$_2$/ATiO$_3$(001) (A=Ba,Pb). The top layers of the multiferroic system ($x = 0$) are plotted as top view in panel (a). On the right-hand side (b) shows the O adatom positions, which mimic the oxygen coverage, c=N(O)/N(Fe), ranging between $c = 0.5$ and two adsorbed O per Fe atom. For $c = 0.5$, the relaxed configurations are marked with the labels A, T, and F, where an oxygen adatom can occupy any site above A, Ti, or Fe, respectively. In the case of $c = 1$ ($c = 1.5$), there are four (three) such configurations and, finally, for $c = 2$ a pair of possibilities is considered, one of which marked as HO means that all four hollow sites are occupied by O.
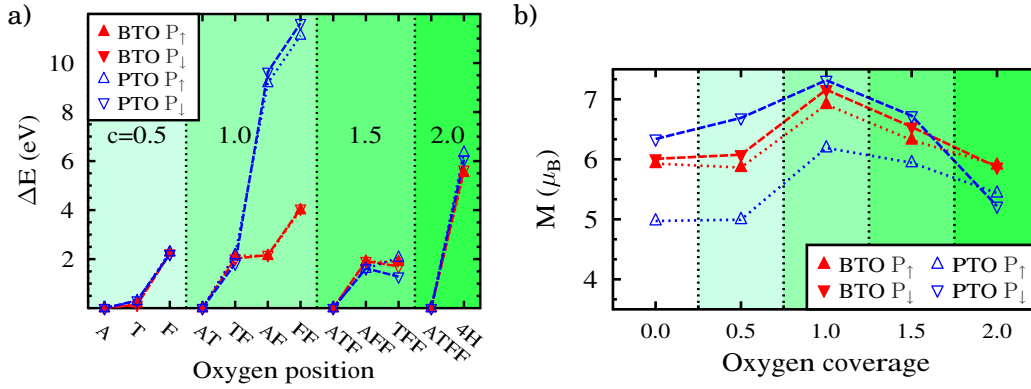
FIGURE 4.7: In (a) relaxed total energy of $O_x/Fe_2/ATO_3(001)$ (A=Ba, Pb and $1 \leq x \leq 4$) is plotted versus the twelve simulated O configurations which are labeled in figure 4.6. For each coverage c, the lowest energy configuration is the zero energy. In the right-hand side the total magnetization of the $O_x/Fe_2/ATiO_3(001)$ cell (A=Ba, Pb and $0 < x < 4$) is plotted as a function of oxygen coverage. For all coverages, the most favorable configuration was used.

of all sites instead of the interstitial sites.

The magnetic properties are investigated after having determined the favored oxygen positions. Figure 4.7 (b) shows the total magnetization for each concentration, where within the calculation the preferred state corresponding to 4.7 (a) was always used. Obviously, from the figure independent of the oxygen concentration, a ferromagnetic ordering is preferred. Furthermore, the total magnetization increases for $c = 0.5$ and 1. The increase is due to induced moments on the additional oxygens. For higher concentrations, the magnetization decreases. If the two polarization states are considered, the change of the magnetization value by the polarization is still observable. Only for $c = 2$ it vanishes. However, it should be kept in mind that this dense coverage is unrealistic since the highest oxidation state of iron seen in Fe_2O_3 is related to the coverage of $c = 1.5$. In conclusion, it turns out that the change of magnetization is robust against oxidation for moderate concentrations.

PUBLICATIONS

1. Effect of the surface polarization in polar
   perovskites studied from first principles

Effect of the surface polarization in polar perovskites studied from first principles

M. Fechner,[1] S. Ostanin,[1] and I. Mertig[1,2]

[1]*Max-Planck-Institut für Mikrostrukturphysik, Weinberg 2, D-06120 Halle (Saale), Germany*
[2]*Martin-Luther-Universität Halle-Wittenberg, Fachbereich Physik, D-06099 Halle, Germany*
(Received 7 December 2007; published 11 March 2008)

The (001) surfaces of polar perovskites $BaTiO_3$ and $PbTiO_3$ have been studied from first principles at $T = 0$ K. For both cases of polarization, the most stable TiO-terminated interfaces show intrinsic ferroelectricity. In the topmost layer, where the O atoms are >0.1 Å above Ti, this leads to metallic instead of the insulating behavior of the electronic states that may have important implications for multiferroic tunneling junctions.

Epitaxial growth technique opens the way to combine ferroelectrics (FEs) and ferromagnets into multicomponent multiferroics, which are inaccessible by traditional synthesis.[1,2] Currently, many laboratories across the world work on a prototypical device, consisting of a few nanometer thick ferroelectric sandwiched between a ferromagnet and another metallic contact. External electric field applied to the FE phase causes a switching of its polarization **P** that, in turn, through the magnetoelectric coupling may change the magnetic order in the ferromagnetic phase.[3] Altering **P** and magnetization independently for encoding information in multiferroics, the smallest quaternary logical memory might be obtained. Fundamentally new multiferroics require a better understanding of the FE order parameters; especially, in the case of thin films here the symmetry is reduced.

Since direct measurements of atomic displacements, occurring in FE near the interface, are extremely challenging, their structures can be understood and numerically characterized from first principles. Recently, much work has been conducted to study bare FE surfaces using the *ab initio* density functional theory (DFT) calculations.[4–12] It has been found that the critical thickness down to 3 unit cells (1.2 nm) is enough to enable the existence of ferroelectricity at room temperature.[13–15] However, there are only some convincing evidences in the literature, i.e., the work by Cohen[5] that the direction of **P** may affect the surface relaxation. The functionality of multiferroics assumes that **P** must be reversible and parallel to the surface normal. Hence, it is worthwhile to carry out *ab initio* calculations which model the reaction of the (001) surface of polar ferroelectric surfaces upon the change of its reversible **P**.

In this paper, we study the (001) surface of ABO_3 perovskites (A=Sr, Ba, Pb and B=Ti), which represent a wide class of ferroelectrics ranging from paraelectric $SrTiO_3$ (STO) to highly polar $PbTiO_3$ (PTO), while $BaTiO_3$ (BTO), with its moderate spontaneous polarization P_s, is an example of a typical FE. The study is based on extensive calculations, using the Vienna *ab initio* simulation package[16] (VASP), in which the effects of relaxation of atomic positions are included. Nowadays, many FE properties can be successfully calculated from first principles.[17] Table I collects the experimental data for the lattice parameters and atomic positions, obtained for the room-temperature tetragonal phase of PTO and BTO (with space group symmetry $P4mm$) and for cubic STO (Pm-$3m$), in comparison with our calculation. Overall,

there is a good agreement between the measured and theoretical structure parameters for the three systems. For polar BTO and PTO, their values of **P**, calculated by the Berry phase approach,[22,23] are in reasonably good agreement with the experiment. The minor differences, seen in Table I between our and some other recent DFT results,[6,12,24] can be attributed to the choice of pseudopotentials and/or to the approximation used for the exchange and correlation potentials. We used the local density approximation (LDA), while the electron-ion interactions were described by the PAW pseudopotentials. After relaxation, the calculated forces are always less than 0.5×10^{-2} eV/Å. The electron pseudo-wave-functions were represented using plane waves, with a cutoff energy of 650 eV. For the Brillouin-zone integration, a dense Monkhorst-Pack[25] mesh was used.

We calculated a 5 unit cell (∼2 nm) thick ABO_3 film. The atoms of the two upper or, alternatively, two lower unit cells were allowed to relax, while all other atoms in the supercell were fixed at their bulklike and previously optimized posi-

TABLE I. The lattice parameters a, c/a, fractional atomic coordinates, z/a, and polarization, calculated for the room-temperature PTO, BTO, and STO phases, are shown in comparison with the corresponding experimental data.

		PTO	BTO	STO
a (Å)	Expt.	3.892[a]	3.991[b]	3.898[b]
		3.858	3.943	3.885
c/a	Expt.	1.071[a]	1.011[b]	1.0
		1.071	1.013	
Ti	Expt.	0.542[a]	0.489[b]	0.5
		0.542	0.492	
O-1, 2	Expt.	0.629[a]	0.511[b]	0.5
		0.622	0.513	
O-3	Expt.	0.124[a]	0.018[b]	0.0
		0.115	0.021	
P_s ($\mu C/cm^2$)	Expt.	75[c]	26[d]	
		94.3	22.9	

[a]Reference 18.
[b]Reference 19.
[c]Reference 20.
[d]Reference 21.

TABLE II. The surface energy E_{surf} (in eV) for the TiO$_2$- and AO-terminated (001) surfaces and the cation-anion displacements δ (in Å) calculated for the top five layers of the perovskite (001) surfaces.

	PTO		BTO		STO
	$P_\uparrow$	$P_\downarrow$	$P_\uparrow$	$P_\downarrow$	$P=0$
E_{surf} (AO)	2.21	2.46	1.49	1.63	1.36
E_{surf} (TiO$_2$)	2.07	2.20	1.31	1.32	1.34
ML					
(1) O-Ti	0.108	0.233	0.102	0.129	0.072
(2) O-A	−0.316	0.260	−0.086	−0.030	0.118
(3) O-Ti	−0.153	0.201	−0.002	0.067	0.018
(4) O-A	−0.476	0.476	−0.082	0.082	0.0
(5) O-Ti	−0.333	0.333	−0.086	0.086	0.0

tions, which are shown in Table I. A vacuum spacer of 2 nm was used to separate the copies of the periodic structures in the direction perpendicular to the surface. The ABO_3 perovskite structures possess a strong anisotropy resulting in the AO (A=Pb, Ba) and TiO$_2$ layers alternating in the [001] direction. The (001) surface of an ABO_3 can be terminated by a AO or a TiO$_2$ layer. Recently, Eglitis and Vanderbilt[12] have reported for the cubic structure of BTO and PTO that the TiO$_2$-terminated surface is more stable. Using the same approach,[12] we calculated the surface energy for the both terminations of ABO_3. The results are shown in Table II. For each perovskite, its TiO$_2$-terminated (001) surface is energetically favorable, indeed. Thus, we consider the (001) surface of ABO_3 to be TiO$_2$ terminated in the following.

In polar PTO and BTO, the displacements of the Ti and O atoms occur along the z axis so that **P** is considered to be directed along the [001] direction as well. First, we must formally set up the direction of electric dipole in the unrelaxed supercell assuming, for instance, that O is always above the corresponding cations in each layer along [001], as given in Table I. Then, we can model the two distinct situations alternatively placing the bulklike 3 unit cell thick substrate and relaxed layers against each other along the z axis. In the first case, which we denote as $P_\downarrow$, the direction of P is antiparallel to the surface normal. The second model labeled by $P_\uparrow$ corresponds to the case where all cations are above O before relaxation and, therefore, P is parallel to [001]. In the tetragonal FE structure, both configurations may coexist in the random state as $P_\downarrow$ and $P_\uparrow$ domains separated by a domain wall of <2 nm. To quantify the process of relaxation, we use the cation-anion displacements $\delta=z_O-z_{cation}$ calculated for each AO and TiO layer near the interface. In the bulklike substrate of polar PTO and BTO, the model $P_\uparrow$ means that $\delta<0$ and, vice versa, the case of $P_\downarrow$ models the situation where $\delta>0$.

Figure 1 shows several top monolayers (MLs) of PTO(001) after relaxation. The case $P_\uparrow$ ($P_\downarrow$) is shown on the left (right) side of Fig. 1. The arrows indicate the direction of the dipoles in each ML, while the numbers at the arrows give the intralayer displacements δ in angstroms, calculated between the O and metal atoms along [001]. In state $P_\downarrow$, all
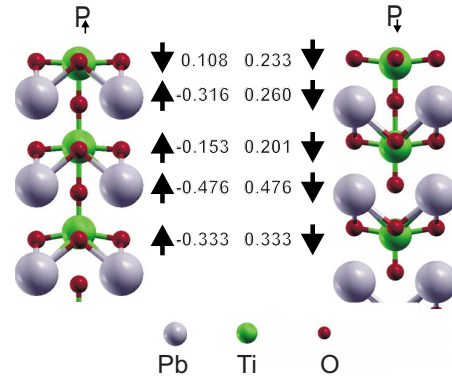

FIG. 1. (Color online) The relaxed top layers of the PTO(001) surface, with polarizations $P_\uparrow$ (left) and $P_\downarrow$ (right). The arrows indicate the direction of the dipole within each layer, while the numbers show the displacements δ in Å between O and Ti/Pb along [001]. For the case of $P_\uparrow$, the sign of δ in the topmost TiO layer is reversed.

dipoles possess the same orientation, which means that O is always above the cation within each layer. In bulk PTO, the intralayer displacement δ is 0.333 Å for the TiO layer and 0.476 Å for the PbO layer. For the three top MLs near the interface, their δ are reduced by 30%–45% with respect to the corresponding bulk values. In the topmost TiO layer, the reduction of δ is ~30%. For the second (PbO) and third (TiO) layers from the interface, we find that their δ is reduced by 45% and 40%, respectively. In the case of $P_\uparrow$, shown in the left panel of Fig. 1, the result of relaxation is rather different. In the third ML, the separation between Ti and O along [001] is 0.153 Å, which is reduced by 54% against the corresponding bulk value. For the second ML, we obtain the reduction of 33%. However, the most significant changes occur in the topmost TiO layer, whose δ is largely reduced by 68%, whereas the dipole is reversed compared to all others. Thus, using the $P_\uparrow$ model and placing all O below the cations, we obtained in the topmost layer the relaxed configuration where O is above Ti. This is similar to the case of $P_\downarrow$.

To investigate the effect of the surface rumpling in perovskites, we repeat the calculations for STO(001) and BTO(001). In Table II, the corresponding results of our zero temperature calculation are listed. For paraelectric STO, we obtain that its TiO-terminated (001) surface after relaxation becomes marginally polar, with a positive rumpling normal to the surface in the top three MLs, where the O atoms are above the cations by <0.12 Å. This is in good agreement with the most recent experimental studies.[26] The positive rumpling predicted for bare surfaces of perovskites leads to a relatively low catalytic activity. With increasing temperature, the rumpling is distorted and it may stimulate further potential catalysis. For the TiO-terminated BTO surface, we have found the details of relaxation similar to those of PTO. In fact, all our results are in good agreement with those reported by Eglitis and Vanderbilt.[12] In the case of $P_\uparrow$, the topmost BTO rumpling of ~0.1 Å, being larger than the corresponding bulk value, is similar to that of highly polar PTO. The sign of δ in the topmost ML of BTO is reversed with respect
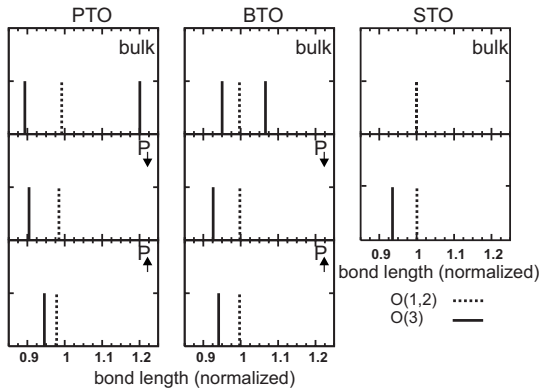
FIG. 2. Ti-O bond lengths in the fivefold coordinated polyhedra of the topmost layer of PTO(001), BTO(001), and STO(001) compared to those obtained in the corresponding bulk structures, with the sixfold coordinated environments.

to all others calculated for the layers situated far down from the interface. In the third ML, δ is 0. The $P_\downarrow$ model yields for BTO(001) the reversal dipole in the second ML, with marginal δ. Thus, we find for the three systems and different arrangements of **P** that the TiO-terminated (001) surfaces prefer the configuration where O is above Ti. In the cubic ABO_3 perovskite structure, each Ti^{4+} ion sits in the regular sixfold coordinated site with all of the Ti-O bonds of equal length, as shown in Fig. 2 for bulk STO.

In the tetragonal perovskite structure, such as t-PTO, the relaxed cluster of O atoms about the sixfold coordinated Ti forms a distorted octahedron, where one of the two bond lengths along [001] is rather short, while another Ti-O bond in the vertical direction is significantly longer than the four other bonds stretching in the equatorial plane. If we exclude the longest Ti-O bond from the consideration using the electrostatic arguments, then the environment for each Ti becomes the fivefold coordinated polyhedra, which is similar to that of Ti at the interface. The left three panels of Fig. 2 compare the Ti-O bond lengths in bulk PTO, normalized to the value of the ideal octahedron in the cubic structure, to those in the polyhedron around fivefold coordinated Ti in the topmost layer. Using the $P_\downarrow$ model for the PTO(001) surface, we obtain the Ti-O bonds whose lengths are similar to those of t-PTO and, hence, nothing dramatic happens in the environment of the topmost Ti. In the case of $P_\uparrow$, the bond length distribution around the topmost Ti is restricted so that the equatorial and vertical bond lengths tend to be equal to each other. Moreover, the closest O atom to the surface Ti is attached along [001] from the opposite side compared to all Ti placed below the surface in the regular crystal structure within $P_\uparrow$. It is clear that the O-Ti-O bond angles for the equatorial Ti-O bonds of the topmost ML must be dramatically changed to compensate the charge distribution around Ti. It appears that these bond angles become $>90°$, as shown in Fig. 1. Therefore, whatever the state of **P** modeled in t-PTO is, the O atoms must relax above Ti on the Ti-O-terminated (001) surface. Regarding BTO, the same conclusions may be drawn.
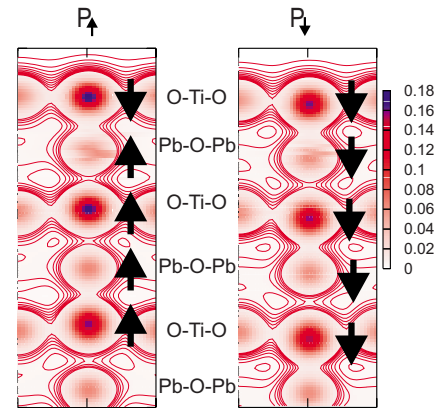
Figure 3 shows the view of the charge density along [010]

FIG. 3. (Color online) The charge density calculated for the top six layers of $PbTiO_3$(001) and projected on the x-z plane. The two opposite polarization states are shown: $P_\uparrow$ (left) and $P_\downarrow$ (right) where the dipole directions within each layer are labeled by the arrows. In the case of $P_\uparrow$, the isocharge lines of the third TiO layer from the interface show a blockade of the charge transfer along [001].

calculated for the top six MLs of PTO and projected on the x-z plane of the supercell. The isocharge lines plotted in Fig. 3 for both cases of **P** illustrate the charge transfer across the cell, while the arrows indicate the dipole directions within each ML. In the case of $P_\downarrow$, which is shown in the right panel of Fig. 3, there are three bridges seen between Ti and nearest O. The shortest bond with O, which is always below Ti along [001], has the large population value. In the $P_\uparrow$ state, the charge transfer picture is similar to that of $P_\downarrow$ for the topmost Ti only. Far below the interface (starting from the fifth ML), all Ti have the most populated bond with O which is above Ti. In the third ML, however, the Ti ion is strongly bonded to equatorial oxygens, showing some sort of blockade for the charge transfer along the [001] direction. This may reveal the key electronic state factors behind the surface relaxation of polar FE.
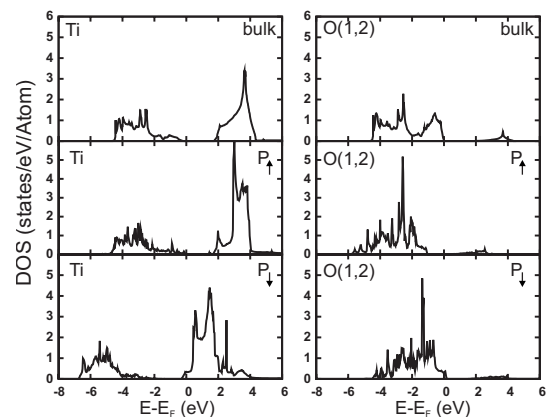

FIG. 4. The Ti- and O_1-resolved DOSs of t-BTO are plotted in the two upper panels where the top of the valence band is taken as zero energy. In the lower panels, the corresponding local DOS of the TiO-terminated (001) surface are plotted for the $P_\uparrow$ and $P_\downarrow$ states.

Recently, Urakami *et al.*[27] have observed the surface conductance of $BaTiO_3$ single crystals in ultrahigh vacuum below T_C. It has been shown that the in-plane conductance is the result of an intrinsic surface electron-hole layer that is due to the surface polarity and not due to O vacancies or some other defects. The *I-V* characteristics show a pronounced difference of conduction between the poled states in BTO. We can explain this difference in a simple way using our *ab initio* results. To reveal the differences between $P_\downarrow$ and $P_\uparrow$, we plot in Fig. 4 the Mulliken site-projected density of states (DOS) of the BTO(001) surface for both cases of polarization. The Ti and O DOSs for the topmost ML are shown in comparison with the corresponding DOS of *t*-BTO. For bulk BTO, Fig. 4 shows a pronounced insulating band gap of 2 eV. The value is typically underestimated by the LDA approximation of DFT. Comparing the Ti and O DOSs of *t*-BTO and the topmost ML of BTO(001), we see a spectacular change of the electronic states occurring due to the surface relaxation and variation of **P**. The major DOS features can be summarized as follows. In the case of $P_\uparrow$, a few O states appear in the band gap, while the Ti DOS is not affected. For the $P_\downarrow$ poled state, the Ti lower conduction band, being shifted downward in energy by ~ 2 eV, significantly contributes to the DOS in the band gap region. This causes the metallic behavior of the topmost ML in the case of $P_\downarrow$, yielding a rather large in-plane conductance. In the case of $P_\uparrow$, the Ti states have a gap at E_f, which is related to a tiny in-plane conductance. Depending on the polarization direction the topmost ML undergoes, a transition from metallic to oxide behavior shows metallic or oxide behavior. As a consequence, the in-plane conductance changes drastically, which is a reasonable explanation of the experimental results by Urakami *et al.*[27]

In summary, from the *ab initio* basis of our work, we have shown that the intrinsic ferroelectricity in polar perovskites is suppressed by $\sim 30\%$ in the surface region. For both cases of polarization direction, the TiO-terminated surface of BTO and PTO forms an electric dipole where the O atoms are shifted >0.1 Å above Ti. Nevertheless, the electronic structure of the surface layer changes from metallic to oxide behavior under the reversal of polarization, which changes the surface conductance drastically.[27] This may have important implications in the design of multiferroic nanodevices.

[1] M. Dawber, K. M. Rabe, and J. F. Scott, Rev. Mod. Phys. **77**, 1083 (2005).

[2] H. Zheng, J. Wang, S. E. Lofland, L. M.-A. Z. Ma, T. Zhao, L. Salamanca-Riba, S. R. Shinde, S. B. Ogale, F. Bai, and D. Viehland, Science **303**, 661 (2004).

[3] W. Eerenstein, N. D. Mathur, and J. F. Scott, Nature (London) **442**, 759 (2006).

[4] J. Padilla and D. Vanderbilt, Phys. Rev. B **56**, 1625 (1997).

[5] R. E. Cohen, Ferroelectrics **194**, 323 (1997).

[6] G. Sághi-Szabó, R. E. Cohen, and H. Krakauer, Phys. Rev. Lett. **80**, 4321 (1998).

[7] E. Heifets, R. I. Eglitis, E. A. Kotomin, J. Maier, and G. Borstel, Phys. Rev. B **64**, 235417 (2001).

[8] J. B. Neaton and K. M. Rabe, Appl. Phys. Lett. **82**, 1586 (2003).

[9] Y. Umeno, T. Shimada, T. Kitamura, and C. Elsässer, Phys. Rev. B **74**, 174111 (2006).

[10] Y. X. Wang, M. Arai, T. Sasaki, and C. L. Wang, Appl. Phys. Lett. **88**, 091909 (2006).

[11] S. Lisenkov and L. Bellaiche, Phys. Rev. B **76**, 020102(R) (2007).

[12] R. I. Eglitis and D. Vanderbilt, Phys. Rev. B **76**, 155439 (2007).

[13] J. Junquera and P. Ghosez, Nature (London) **422**, 506 (2003).

[14] N. A. Spaldin, Science **304**, 1606 (2004).

[15] D. D. Fong, G. B. Stephenson, S. K. Streiffer, J. A. Eastman, O. Auciello, P. H. Fuoss, and C. Thompson, Science **304**, 1650 (2004).

[16] G. Kresse and J. Furthmüller, Phys. Rev. B **54**, 11169 (1996).

[17] P. Ghosez and J. Junquera, *Handbook of Theoretical and Computational Nanotechnology*, edited by M. Rieth and W. Schommers (American Scientific Publisher, Stevenson Ranch, CA, USA, 2006), Vol. 7, Chap. 134.

[18] H. Mestric, R.-A. Eichel, T. Kloss, K.-P. Dinse, So. Laubach, St. Laubach, P. C. Schmidt, K. A. Schonau, M. Knapp, and H. Ehrenberg, Phys. Rev. B **71**, 134109 (2005).

[19] T. Toshio, K.-H. Hellwege, H. Landolt, R. Börnstein, and O. Madelung, in *Ferro- and Antiferroelectric Substances*, edited by K.-H. Hellwege and A. M. Hellwege, Landolt-Börnstein, Group III, Vol. 3 (Springer-Verlag, Berlin, 1981).

[20] V. Gavrilyachenko, R. Spinko, M. Martynenko, and E. Fesenko, Sov. Phys. Solid State **12**, 1532 (1970).

[21] H. H. Wieder, Phys. Rev. **99**, 1161 (1955).

[22] R. D. King-Smith and D. Vanderbilt, Phys. Rev. B **47**, 1651 (1993).

[23] R. Resta, Rev. Mod. Phys. **66**, 899 (1994).

[24] R. D. King-Smith and D. Vanderbilt, Phys. Rev. B **49**, 5828 (1994).

[25] H. J. Monkhorst and J. D. Pack, Phys. Rev. B **13**, 5188 (1976).

[26] P. A. W. van der Heide, Q. D. Jiang, Y. S. Kim, and J. W. Rabalais, Surf. Sci. **473**, 59 (2001).

[27] Y. Urakami, M. Yamato, and Y. Watanabe, Ferroelectrics **346**, 32 (2007).

2. Magnetic phase transition in two-phase multiferroics predicted from first principles

Magnetic phase transition in two-phase multiferroics predicted from first principles

M. Fechner,[1] I. V. Maznichenko,[2] S. Ostanin,[1] A. Ernst,[1,3,*] J. Henk,[1] P. Bruno,[4] and I. Mertig[1,2]

[1]*Max-Planck-Institut für Mikrostrukturphysik, Weinberg 2, D-06120 Halle, Germany*
[2]*Institut für Physik, Martin-Luther-Universität Halle-Wittenberg, D-06099 Halle, Germany*
[3]*Donostia International Physics Center (DIPC), Paseo de Manuel Lardizabal 4, 20018 San Sebastin/Donostia, Basque Country, Spain*
[4]*European Synchrotron Radiation Facility, Boîte Postale 220, F-38043 Grenoble Cedex, France*

On the basis of first-principles electronic-structure calculations we predict that epitaxial multiferroic films—fabricated as ultrathin Fe films deposited on TiO_2-terminated (001) surfaces of $ATiO_3$ perovskites (A=Pb,Ba)—exhibit an unexpected change in their magnetic structure with increasing Fe-film thickness. The magnetic order changes from ferromagnetic, with a magnetization of about $3\mu_B$/atom for the 1 ML system, to ferrimagnetic with almost vanishing magnetization upon deposition of a second Fe layer. Ferromagnetic order is restored for thicker Fe films but with significantly reduced magnetization as compared to Fe bulk. The effect is understood in terms of hybridization of electronic states and geometric structure. The magnetoelectric coupling affects the size of the magnetic moments moderately; a spin-reorientation transition is not found.

Epitaxial growth techniques open paths to assemble two-phase multiferroic films from ferroelectrics and ferromagnets (FMs). Inaccessible by conventional synthesis, they exhibit specific properties which are superior to those of customary materials.[1] Especially switching and spin filtering make them excellent candidates for next-generation magnetoelectronic devices, such as magnetic-field sensors and memories. Current efforts focus on the realization of prototypical devices which consist of a few-nanometer thick ferroelectric sandwiched between a ferromagnet and a metallic contact.[2,3]

The key feature of multiferroic devices is the magnetoelectric coupling. In a simple picture, the coupling between the electric polarization P (a result of atomic displacements) in the ferroelectric component and the magnetization M in the FM component is mediated by the hybridization of spin-polarized electronic states at the common interface. If the coupling is sufficiently strong, M can be modified by an external electric field. Analogously, P can be changed by an external magnetic field. This mechanism allows to store information in nanometer-sized memories[4,5] with four logic states, ($\pm P$, $\pm M$). The quest for fundamentally different multiferroics requires evidently thorough understanding of the mechanisms which mediate the magnetoelectric coupling.

Prototypical two-phase multiferroic systems are heterojunctions of Fe and polar $ATiO_3$ perovskites, e.g., $BaTiO_3$ (BTO) and $PbTiO_3$ (PTO). The stable TiO_2-terminated (001) surface of the latter forms an electric dipole.[6] With the surface oxygen atoms displaced outward with respect to the Ti atoms for both P orientations, the intrinsic ferroelectricity is notably suppressed at the surface.[7] Hence, a critical thickness (typically 1 nm) is required to maintain ferroelectricity at room temperature.[8] Please note that little is known about the magnetic properties of Fe/$ATiO_3$ heterojunctions, in particular about the Fe-thickness dependence.[9,10]

Considering ultrathin Fe films on an $ATiO_3$ perovskite we are confronted with a delicate interplay between geometry, electronic properties, and magnetic structure. Since Fe has a tendency toward antiferromagnetism if the volume is reduced,[11] we expect a complex magnetic structure in Fe/$ATiO_3$ in dependence on the Fe-film thickness. Questions to be answered concern the magnetic order, the size of the magnetization, and the magnetic anisotropy. Further, one can ask for differences if a ferroelectric substrate (BTO, PTO) is replaced by a paraelectric, e.g., $SrTiO_3$ (STO). To predict the properties of these multiferroics reliably, sophisticated first-principles methods of computational materials science are inevitable.

In this Brief Report we report on a first-principles investigation of the magnetic order and the magnetoelectric effect in $(Fe_2)_L$/$ATiO_3$(001) multiferroics with Fe-film thickness L=1,...,4 monolayers (ML) on top of the TiO_2-terminated (001) surfaces of BTO, PTO, and STO. This choice of perovskite substrates allowed to model a variety of nanostructures, ranging from paraelectric to highly polar interfaces, with different in-plane misfits. The (001) surface was chosen TiO-terminated, according to its superior stability.[6] As striking result we find an unexpected change in the magnetic order from ferromagnetic (L=1) to ferrimagnetic order upon adding a second Fe layer (L=2). A sizable change in the magnetic structure appears due to reversal of P, making these multiferroics very appealing for device applications.

The delicate interplay of geometric, electronic, and magnetic structures necessitates a multicode approach, which already proved successful.[12] The geometric relaxations were obtained by VASP,[13] well known for its precise determination of energetics and forces. The atomic positions serve as input for multiple-scattering calculations of the electronic and magnetic structure [scalar-relativistic Korringa-Kohn-Rostoker (KKR)].[14] The magnetocrystalline anisotropy was computed with a relativistic layer-KKR code.[15] In all steps, we applied the local spin-density approximation (LSDA) to density-functional theory. Various quantities were carefully cross-checked among the three computer codes to obtain consistent results. Reliability is achieved by numerous convergence tests.

The AO and TiO_2 planes in $ATiO_3$ perovskites (A=Ba,Pb,Sr) alternate in the [001] direction. In BTO and PTO, the atoms in each layer are mutually displaced along [001] (z axis); hence P is along that axis. For O atoms dis-
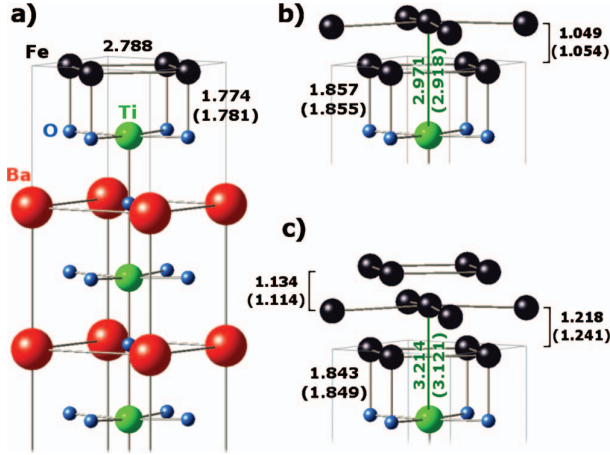
FIG. 1. (Color) Geometry of $(Fe_2)_L/BaTiO_3(001)$ for [left; (a)] $L=1$ and [right; (b) and (c)] $L=2,3$. Selected interatomic distances are given in angstroms for the $P_\downarrow(P_\uparrow)$ configuration without (within) brackets. Spheres represent Fe (black), Ba (red), Ti (green), and O (blue) sites. For $L=1$ (a), layers **S**$+1,\ldots,$**S**-4 are shown, while for $L=2$ (b) and $L=3$ (c) **S**$+2,\ldots,$**S** and **S**$+3,\ldots,$**S** are displayed, respectively.

placed along [001] with respect to the cations (Ba, Pb, and Ti), **P** points toward [00$\bar{1}$], denoted $P_\downarrow$ here. For $P_\uparrow$, one has **P** pointing along [001] and opposite relaxations (for details, see Ref. 6). The intralayer buckling is defined for each layer l by $\delta_l = z_O - z_{cation}$. δ is positive (negative) for $P_\downarrow$ ($P_\uparrow$). For paraelectric STO, the displacements δ_l are zero.

The outermost TiO_2 layer in Fe/ATiO$_3$ is denoted **S**. Layers toward the perovskite bulk are labeled **S**-1, **S**-2, etc., whereas Fe layers are indicated as **S**$+1$, **S**$+2,\ldots,$**S**$+L$. As expected for $(Fe_2)_L/A$TiO$_3$, Fe forms a distorted body-centered tetragonal lattice, with the sites in layer **S**$+1$ on top of the O sites in layer **S** (Fig. 1). In the following we focus on Fe on BTO.

The atomic positions deduced by VASP serve as input for the first-principles KKR calculations of the electronic and magnetic properties. Considering $L=1$, the Fe magnetic moments ($\approx 3\mu_B$) are significantly enhanced with respect to the Fe bulk value of $2.26\mu_B$ (Table I). The hybridization between the Fe $3d$, Ti $3d$, and O $2p$ states at the interface [layers **S** and **S**$+1$; cf. the associated spin-resolved density of states in

TABLE I. Local magnetic moments of $(Fe_2)_L/BaTiO_3(001)$, $L=1,2,3$, for $P_\uparrow$ and $P_\downarrow$ obtained by KKR (in μ_B).

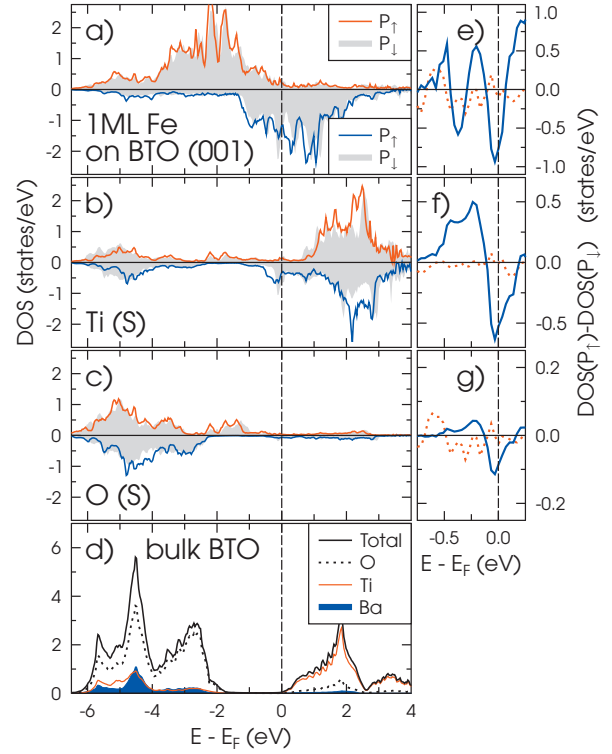|		$L=1$		$L=2$		$L=3$	
		$P_\uparrow$	$P_\downarrow$	$P_\uparrow$	$P_\downarrow$	$P_\uparrow$	$P_\downarrow$
Fe	**S**$+3$					1.80	1.94
Fe	**S**$+2$; Ti			-2.49	-2.40	1.91	1.93
Fe	**S**$+2$; Ba			2.28	2.18	1.04	0.95
Fe	**S**$+1$	3.02	3.05	0.22	0.26	1.05	0.94
O	**S**	0.10	0.10	0	0	0.01	0.01
Ti	**S**	-0.10	-0.04	-0.03	-0.02	-0.12	-0.05

FIG. 2. (Color) Electronic structure at the surface of $(Fe_2)_1/BaTiO_3(001)$. [(a)–(c)]: spin-resolved density of states (DOS) of Fe in layer **S**$+1$ (a) as well as of Ti (b) and O (c) in layer **S** for $P_\uparrow$ (lines) and $P_\downarrow$ (gray). (d) Total and partial DOS of bulk BaTiO$_3$, with the bottom of the conduction band taken as energy reference. [(e)–(g)] Spin-resolved difference of the DOS for $P_\uparrow$ and $P_\downarrow$ of Fe, Ti, and O [as in (a)–(c)] close to the Fermi energy E_F (majority: red dotted; minority: blue solid).

Figs. 2(a)–2(c)] induces magnetic moments in the interfacial O and Ti atoms. In particular the Ti moments, aligned antiparallel to those of Fe and O, originate from the hybridization of Ti $3d$ with minority-spin Fe $3d$ states.[9,10] Reversal of **P** affects the magnetic moments mildly (less than $0.06\mu_B$).

Adding a second Fe layer changes the magnetic order considerably (Table I, $L=2$): the magnetic moments in the Fe layer **S**$+1$ are almost quenched while the sizable moments in the surface layer **S**$+2$ are ordered antiparallel. Please note that the two Fe sites in **S**$+2$ are inequivalent [Fig. 1(b)]; Fe(**S**$+2$; Ti) [Fe(**S**$+2$; Ba)] is on top of Ti (Ba) sites in layer **S**. The different magnetic moments reflect the environment of these atoms, in particular the atomic volumes and the hybridization. Polarization reversal affects mainly the positions of Ti atoms and consequently those of the Fe atoms atop. For example, the z position of Fe(**S**$+2$; Ti) is changed by 0.053 Å, while that of Fe(**S**$+2$; Ba) is with about 0.005 Å less influenced [Fig. 1(b)]. The surface-layer buckling is 0.02 Å (0.04 Å) for $P_\downarrow$($P_\uparrow$).

Deposition of a third Fe layer restores the ferromagnetic order (Table I, $L=3$). The distance between Fe layers at the surface is about 1.1 Å, i.e., less than in bcc Fe(001) (1.43 Å). Reversal of the polarization attracts the upper two Fe layers with respect to Ti(**S**) about 0.03 Å, which is larger

than for $L=2$. Again, the position of the atom Fe($\mathbf{S}+2$; Ti) is subject to polarization switching: its z position is changed by 3% or 0.1 Å. Layers $\mathbf{S}+3$ and $\mathbf{S}+2$ contribute most to the total magnetization with a remarkable "magnetic imbalance" of the two inequivalent Fe sites in layer $\mathbf{S}+2$. Layer $\mathbf{S}+1$ contributes about $1\mu_B$. The largest change upon polarization switching shows up in the surface layer $\mathbf{S}+3$ ($0.14\mu_B$).

As is obvious from the preceding, the positions and the magnetic moments of the Fe atoms in the entire Fe films are determined in a complex manner by the Fe/BTO interface. We obtain two counteracting trends. First, the reduced coordination number at the Fe surface layer causes an increase in the magnetic moments. Second, the reduced atomic volume due to epitaxial strain of the BTO substrate and a drastic tetragonal distortion in comparison with Fe bulk, following Pauling's rule,[16] quench the magnetic moments.

For layer $\mathbf{S}+1$, the Fe-O distances which range from 1.78 to 1.85 Å for $L=1-3$ are substantially smaller than the interatomic distance in bulk bcc Fe. Hence, the diminished volume of interfacial Fe can lead to reduced local magnetic moments.[11] The magnetic moments for $L=1$ are still considerable due to the reduced dimensionality at the surface. For $L=2$, the volume of interfacial Fe is reduced even further and leads to the very small magnetic moments. The small size of Fe atoms in layer $\mathbf{S}+2$ explains as well the antiferromagnetic (AFM) ordering of their local magnetic moments.[11] Adding the third Fe layer increases both the coordination numbers and the atomic volumes and consequently restores ferromagnetic order.

While the magnetic moments do not change sign upon $\boldsymbol{P}$ reversal (only their sizes are moderately affected; Table I), we consider a spin-reorientation transition as another—possible—kind of magnetoelectric switching. Using relativistic layer KKR, the magnetic anisotropy for $(\text{Fe}_2)_1$/BTO(001) is computed within the framework of the magnetic force theorem.[17] For both $\boldsymbol{P}$ orientations, perpendicular anisotropy is favored to in-plane anisotropy, namely, by 0.72 meV ($P_\downarrow$) and 0.54 meV ($P_\uparrow$) per Fe atom. Note that these uniaxial anisotropies are almost twice as large as that of a chemically disordered FePt alloy.[18,19]

The magnetoelectric coupling in $(\text{Fe}_2)_1$/BTO(001) is further illustrated by the density of states at the interface [Figs. 2(e)–2(g)]. A prominent effect is evident in the minority-spin channel of the Fe- and Ti-electronic states while there is no significant effect in the majority channel. Thus, reversal of $\boldsymbol{P}$ leads to a substantial transfer of minority-spin charge at the interface.[20] Because the Fe-Ti distance for $P_\downarrow$ is smaller than for $P_\uparrow$, the overlap between the Fe and Ti d orbitals is larger, leading to an increased charge density in the surface layer $\mathbf{S}+1$ (Fig. 3). The excessive electrons result in a slightly larger magnetic moment of Fe for $P_\downarrow$ (Table I).

To address the effects of polarizability and lattice misfit on the magnetic structure of the Fe films, additional calculations were performed for Fe-covered PTO and STO. For all perovskite substrates and Fe-film thicknesses, total energies of three magnetic configurations were computed: besides FM and paramagnetic (PM) Fe films, AFM films were considered. In the latter case, the magnetic moments of the two Fe sites in each layer are oppositely oriented. The peculiarity of the case of $L=2$ becomes apparent by the fact that the con-
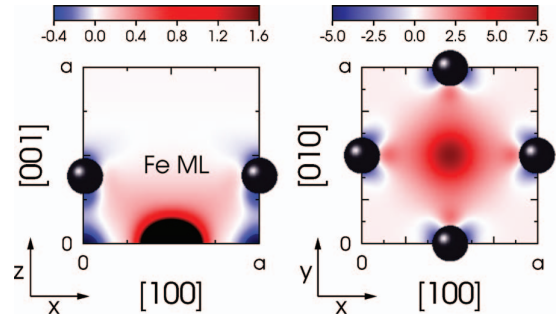

FIG. 3. (Color) Charge redistribution of minority-spin electrons at the surface of $(\text{Fe}_2)_1$/BTO(001) upon reversal of the electric polarization $\boldsymbol{P}$ with respect to the surface normal. The difference of the charge densities for $P_\uparrow$ and $P_\downarrow$ is depicted in a perpendicular (left) and an in-plane cut through the Fe atoms (size a^2; color scales in arbitrary units). The Fe atoms are represented by spheres.

strained self-consistent calculations did not converge for the complete AFM configuration; forcing the top layer $\mathbf{S}+2$ to be antiferromagnetic, the layer $\mathbf{S}+1$ shows ferromagnetic order.

In almost all cases, the hierarchy $E_{\text{FM}} < E_{\text{PM}} < E_{\text{AFM}}$ is observed. An exception is again $L=2$ for which a ferrimagnetic order with small (absolute) magnetic moments is favored (Fig. 4; cf. Table I for Fe/BTO). Even in the case of paraelectric STO, both the magnetization and the total-energy hierarchy are similar to those of the polar substrates. Thus, the magnetic order of the two-phase multiferroics can be tuned by the Fe-film thickness independently of the perovskite substrate. Strain and electric polarizabilities are of minor importance. For each of the systems with $L=1$, the magnetoelectric coefficient α is estimated. α is defined as $\mu_B \Delta M/(VE_c)$ in terms of the magnetization change ΔM per volume V and strength of the coercive electric field E_c of the substrate. For the surface bilayer of Fe/BTO, $\mu_B \Delta M/V$
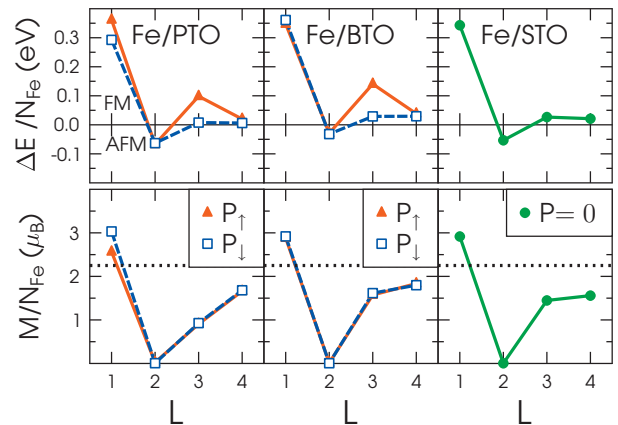

FIG. 4. (Color) Magnetism of $(\text{Fe}_2)_L$/$A\text{TiO}_3$(001) for PbTiO_3, BaTiO_3, and SrTiO_3 versus Fe-film thickness L. Top: total-energy difference $\Delta E \equiv E_{\text{AFM}} - E_{\text{FM}}$ of the antiferromagnetic and ferromagnetic configurations (see text) normalized with respect to the number N_{Fe} of Fe atoms in the film unit cell. Bottom: magnetization per Fe atom for the lowest-energy configuration. Dotted lines indicate the magnetic moment of Fe bulk.

$\approx 1.6 \times 10^2$ G and, assuming $E_c = 10$ kV/cm, $\alpha \approx 0.016$ G cm/V, which is comparable with α measured in epitaxial $BiFeO_3/CoFe_2O_4$ nanostructures.[21] For Fe/PTO with $E_c = 33$ kV/cm, $\mu_B \Delta M/V \approx 2.4 \times 10^3$ G yields $\alpha \approx 0.073$ G cm/V, which is significantly larger than that of Fe/BTO.

In conclusion, the magnetic structure of two-phase multiferroics, realized as ultrathin Fe films on $ATiO_3$ perovskites ($A = Ba, Pb, Sr$), is found to exhibit a rich and peculiar structure, as is predicted from first-principles computational materials science. A ferromagnetic-to-ferrimagnetic transition which is accompanied by a strong reduction in the Fe magnetic moments could be used in device applications to tailor the properties of the magnetic subsystem. This effect mainly originated from the magnetovolume instability of Fe. In our opinion, a similar effect may occur as well in other materials, which exhibit the magnetovolume instability such as manganese[22] and gadolinium.[23] Significant magnetoelectric coupling via the Fe/$ATiO_3$ interface is predicted; a spin-reorientation transition under switching is not found. In view of device applications it appears highly desirable to investigate theoretically and experimentally the thickness-dependent magnetic properties of Fe films sandwiched between ferroelectric perovskites.

*aernst@mpi-halle.de

[1] M. Dawber, K. M. Rabe, and J. F. Scott, Rev. Mod. Phys. **77**, 1083 (2005).

[2] N. Hur, S. Park, P. A. Sharma, J. S. Ahn, S. Guha, and S.-W. Cheong, Nature (London) **429**, 392 (2004).

[3] M. Gajek, M. Bibes, S. Fusil, K. Bouzehouane, J. Fontcuberta, A. Barthélémy, and A. Fert, Nature Mater. **6**, 296 (2007).

[4] W. Eerenstein, N. D. Mathur, and J. F. Scott, Nature (London) **442**, 759 (2006).

[5] S.-W. Cheong and M. Mostovoy, Nature Mater. **6**, 13 (2007).

[6] M. Fechner, S. Ostanin, and I. Mertig, Phys. Rev. B **77**, 094112 (2008).

[7] J. Junquera and P. Ghosez, Nature (London) **422**, 506 (2003).

[8] D. D. Fong, G. B. Stephenson, S. K. Streiffer, J. A. Eastman, O. Auciello, P. H. Fuoss, and C. Thompson, Science **304**, 1650 (2004).

[9] C.-G. Duan, S. S. Jaswal, and E. Y. Tsymbal, Phys. Rev. Lett. **97**, 047201 (2006).

[10] J. P. Velev, C.-G. Duan, K. D. Balashchenko, S. S. Jaswal, and E. Y. Tsymbal, J. Appl. Phys. **103**, 07A701 (2008).

[11] T. C. Leung, C. T. Chan, and B. N. Harmon, Phys. Rev. B **44**, 2923 (1991).

[12] C. R. Ast, J. Henk, A. Ernst, L. Moreschini, M. C. Falub, D. Pacilé, P. Bruno, K. Kern, and M. Grioni, Phys. Rev. Lett. **98**, 186807 (2007).

[13] G. Kresse and J. Furthmüller, Phys. Rev. B **54**, 11169 (1996).

[14] M. Lüders, A. Ernst, W. M. Temmerman, Z. Szotek, and P. J. Durham, J. Phys.: Condens. Matter **13**, 8587 (2001).

[15] J. Henk, H. Mirhosseini, P. Bose, K. Saha, N. Fomynikh, T. Scheunemann, S. V. Halilov, E. Tamura, and R. Feder, OMNI— Fully relativistic electron spectroscopy calculations, 2008; the computer code is available from the authors.

[16] L. Pauling, *The Nature of the Chemical Bond* (Cornell University Press, Ithaca, 1960).

[17] J. Henk, A. M. N. Niklasson, and B. Johansson, Phys. Rev. B **59**, 9332 (1999).

[18] S. Ostanin, S. S. A. Razee, J. B. Staunton, B. Ginatempo, and E. Bruno, J. Appl. Phys. **93**, 453 (2003).

[19] J. B. Staunton, S. Ostanin, S. S. A. Razee, B. L. Gyorffy, L. Szunyogh, B. Giatempo, and Ezio Bruno, Phys. Rev. Lett. **93**, 257204 (2004).

[20] R. D. King-Smith and D. Vanderbilt, Phys. Rev. B **47**, 1651(R) (1993).

[21] F. Zavaliche, H. Zheng, L. Mohaddes-Ardabili, S. Y. Yang, Q. Zhan, P. Shafer, E. Reilly, R. Chopdekar, Y. Jia, P. Wright *et al.*, Nano Lett. **5**, 1793 (2005).

[22] V. L. Moruzzi, P. M. Marcus, and J. Kübler, Phys. Rev. B **39**, 6957 (1989).

[23] I. D. Hughes, M. Däne, A. Ernst, W. Hergert, M. Lüders, J. Poulter, J. B. Staunton, A. Svane, Z. Szotek, and W. M. Temmerman, Nature (London) **446**, 650 (2007).

3. Magnetoelectric coupling at biferroic interface studied from first principles

Magnetoelectric coupling at biferroic interface studied from first principles

Michael Fechner[1], Sergey Ostanin[1] and Ingrid Mertig[1,2]

Max-Planck-Institut für Mikrostrukturphysik, Weinberg 2, D-06120 Halle (Saale), Germany

Martin-Luther-Universität Halle-Wittenberg, Fachbereich Physik, D-06099 Halle, Germany

E-mail: `fechner@mpi-halle.mpg.de`

Abstract. We present an *ab initio* study of a prospective composite multiferroic $L \cdot \mathrm{Fe_2/PbTiO_3}(001)$, with a Fe-film thickness of $L \leq 4$ monolayers. The change in magnetization induced by the electric polarization reversal is discussed. Our calculations imply a strong magnetoelectric coupling for $L = 1$ and a dramatic change of the magnetic order with increasing the Fe-film thickness between $1 \leq L \leq 3$.

In the absence of space-inversion and time-reversal symmetry, the occurrence of ferroelectricity and magnetism in the same phase of a so called multiferroic (MF) material [1] permits both a switchable electric polarization, $\vec{P}$, and a switchable magnetization, $\vec{M}$. This phenomenon, in principle, allows to store information in nanometer-sized memories with four logic states [2]. Although some MFs, such as $\mathrm{BiFeO_3}$ and $R\mathrm{MnO_3}$ (R rare earths), were known since mid of the seventies, the search for novel multiferroics is not finished yet. In multiferroics, an applied electric field, $\vec{E}$, displacing the magnetic ions, affects the magnetic exchange coupling or, vice versa, the external magnetic field, $\vec{H}$, induces the electric polarization: $P_i \sim \alpha_{ij} H_j$, where α is the magnetoelectric tensor and $(i, j = x, y, z)$. According to Landau theory, the linear magnetoelectric (ME) contribution to the Gibbs free energy is $E_i \alpha_{ij} H_j$. It should be kept in mind that magnetoelectricity is a volume effect for which the induction of $\vec{M}$ depends linearly on $\vec{E}$. In a single-phase MF, $\vec{P}$ and $\vec{M}$ interact weakly and, therefore, α is marginal there. Besides, all single-phase MFs possess a hierarchy of phase transformations [3], in which ferromagnetism disappears far below room temperature.

Ab initio calculations based on density functional theory (DFT) predict that a more robust scenario of magnetoelectricity occurs in epitaxially grown composite MF [4] where the ME effect is mediated by strain across the ferroelectric/ferromagnet interface. Obviously, the quest for fundamentally new MF requires a better understanding of the mechanisms which mediate the ME coupling. In this work, we perform the DFT calculations of the electronic and ferroic properties of $L \cdot \mathrm{Fe_2/PbTiO_3}(001)$, with Fe film thickness, L, ranging between one and four monolayers (ML). This is a prototype system of composite MF. Its $\mathrm{PbTiO_3}$ (PTO) substrate is highly polar, with a spontaneous polarization of $75 \mu \mathrm{C/cm^2}$. Besides, the body-centered cubic Fe and PTO(001) have a good match of their in-plane lattice constant when the bcc-Fe [110] axis is aligned to the [100] axis of PTO. The mismatch of $<3\%$ allows epitaxial growth. This has been recently demonstrated for another composite MF, $\mathrm{BaTiO_3/Fe}$ [5]. All calculations were performed by the Vienna Ab initio Simulation Package (VASP) [6], using the projector-augmented wave pseudopotentials and a planewave basis cutoff energy of 650 eV. The relaxation
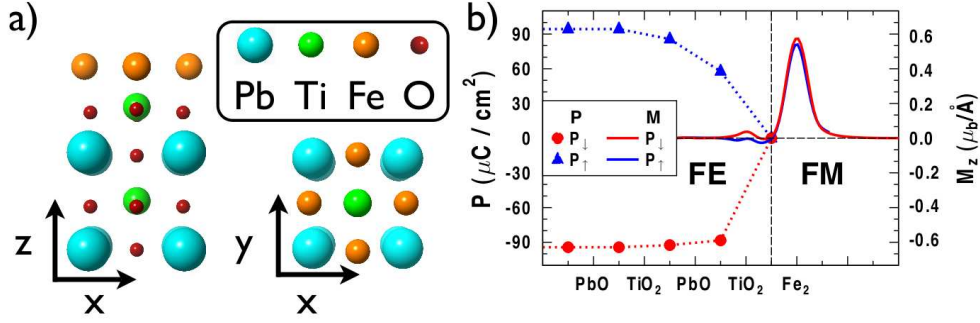
Figure 1. (a): The side- and top view of the TiO-terminated $PbTiO_3(001)$ substrate covered by a single Fe layer. (b): The ferroic properties of 1-ML Fe on PTO are plotted near the interface along [001]: $P_\uparrow$ (blue dotted), $P_\downarrow$ (red dotted) and the corresponding z-projected magnetization densities $M_z^{P_\uparrow}$ (blue solid) and $M_z^{P_\downarrow}$ (red solid). The largest change in M_z induced by the P-reversal comes from interfacial Ti.

in a slab geometry and further calculation of the ferroic properties were performed within the local spin-density approximation to DFT.

1. Results and Summary

To model the (001) surface of PTO, we used the 5-unit-cell ($\sim$2-nm) thick supercell, with a vacuum spacer of 2 nm in the [001] direction. The lattice parameters were set to the equilibrium values of tetragonal PTO [7]. The Ti/O displacements cause the direction of **P** along [001]. When **P** is antiparallel to the surface normal ($P_\downarrow$), oxygen is placed above the cations in each ML, and *vice versa*, the configuration $P_\uparrow$ means that all intralayer displacements $\delta = z_O - z_{cation} < 0$. Since PTO(001) is TiO_2 terminated [7] for both directions of **P**, we calculated, first, $Fe_2/TiO_2/PTO(001)$ where the Fe atoms find their relaxed positions atop oxygen, as shown in Fig. 1(a). This is in agreement with previous *ab initio* calculations [4]. We relaxed the three top PTO layers and Fe layers until the forces are less than 5 meV/Å.

In Fig. 1b, we plot the layer-resolved electric polarization of $1 \cdot Fe_2/PTO(001)$, which was calculated as $P_i = \delta_i \cdot q_{Born}$, where q_{Born} is the Born effective charge. $P_\downarrow$ approaches its bulk value within the first PTO unit cell whereas the state $P_\uparrow$ needs the thickness two times larger than that of $P_\downarrow$. For each P, its magnitude vanishes at the interface. As the result, the two z-projected magnetization densities, which are plotted in Fig. 1b, show no significant difference above the interface. Nevertheless, the total change in magnetization: $\Delta M = M(P_\downarrow) - M(P_\uparrow)$ for this system is about $1\mu_B$. This effect can be explained by a detailed analysis of the electronic density of states. The hybridization between the d-minority states of Fe and Ti d-states leads to an induced magnetic moment on the Ti site, which is oriented opposite to m_{Fe}. This is shown in detail in Fig. 2a for $P_\uparrow$ and $P_\downarrow$. For $P_\uparrow$, the Fe-Ti distance is shorter and, therefore, the corresponding m_{Ti} is larger than that of the $P_\downarrow$ state. The induced and antiferromagnetically oriented magnetic moment of interfacial Ti contributes significantly to the $1\mu_B$-value of ΔM.

We suggest that the magnetic structure may change from strongly ferromagnetic to nearly zero-M ferrimagnetic when a second Fe layer is added (see, Fig. 2b). In the second layer, one Fe sits atop the Ti site of PTO while another Fe atom finds its relaxed position above Pb. For $L=2$, the magnetic moments of interfacial Fe are suppressed while the two environmentally different Fe sites of the surface layer, which show rather significant moments of $2.3\mu_B$ and $2.1\mu_B$, are ordered antiferromagnetically to each other. This is mostly due to a relatively short separation of 1 Å between the Fe layers. The surface Fe atom atop Ti obeys the largest magnetic moment
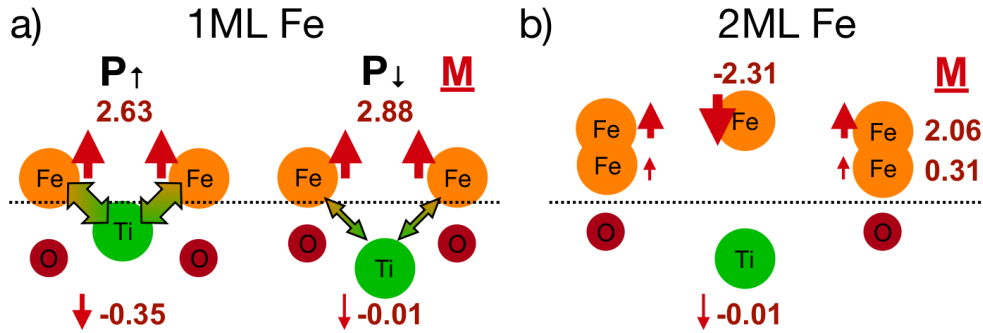
Figure 2. (a): Magnetic structure of dually polar $1\cdot Fe_2/PTO(001)$ is shown as the side view. Here, the numbers indicate the Fe and Ti magnetic moments while their directions are shown by arrows. (b): Nearly zero-M and ferrimagnetically ordered structure of $2\cdot Fe_2/PTO(001)$ is sketched for $P_\downarrow$ only.

for this configuration. This Fe atom and underlying Ti are most affected to the polarization reversal. Regarding the 2-ML Fe film, the issue of reduced atomic volume of interfacial Fe and its suppressed magnetic moment as well as the antiferromagnetic ordering in the topmost Fe layer were discussed in the literature [8]. Ferromagnetic order is restored for thicker Fe films but with significantly reduced magnetization as compared to Fe bulk.

For all $L \leq 4$, the total energies of both the ferromagnetic (FM) and antiferrimagnetic (AFM) configurations of $L\cdot Fe_2/PTO(001)$ were calculated for each P. The energy difference, $\Delta E \equiv E_{AFM} - E_{FM}$, is plotted in the left panel of Fig. 3. When $L=1$ the system is always ferromagnetic whereas the reversal of P shows minor effect. For $L=2$, the AFM order is energetically preferable. In this case, however, we detected some sort of ferrimagnetic structure with nearly zero-M, which is shown in Fig. 2b. When $L \geq 3$ we obtained $E_{FM} < E_{AFM}$ for both polarization directions that means that ferromagnetism is restored.

Fig. 3b shows the magnetization of $L\cdot Fe_2/PTO(001)$ as a function of L. It was calculated for
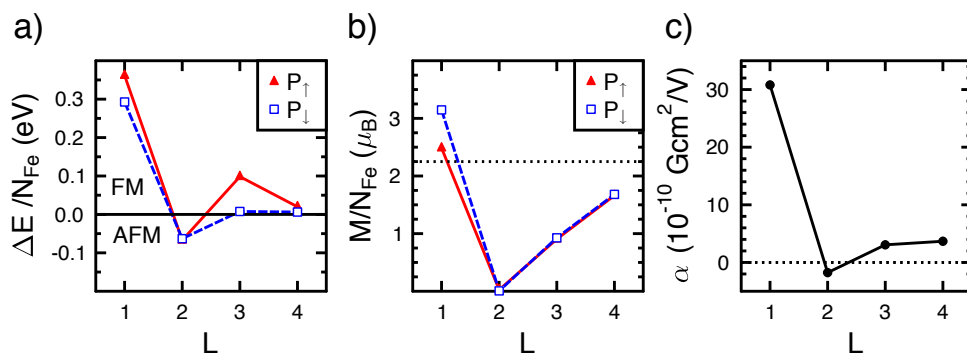

Figure 3. Magnetism and magnetoelectricity of $L\cdot Fe_2/PTO(001)$ versus the Fe-film thickness, L. (a): the total-energy difference $\Delta E \equiv E_{AFM} - E_{FM}$ between the antiferrimagnetic (AFM) and ferromagnetic (FM) configurations. ΔE is normalized with respect to the number N_{Fe} of Fe atoms in the supercell.(b): the magnetization per Fe atom for the lowest-energy configuration. Here, the dotted line indicates the magnetic moment of Fe bulk. (c): The magnetoelectric coupling coefficient α is plotted versus L.

each P and energetically favorable magnetic solution, which is always ferromagnetic except $L=2$. The M is normalized to the number of Fe atoms in the supercell to allow a comparison between the different Fe thicknesses. The two curves in Fig. 3b correspond to dually polar substrate, and their difference is the change in magnetization, ΔM, with respect to the P reversal. For $L=1$, the large $m_{Fe} \approx 3\ \mu_B$ enables the large value of M while the $1\ \mu_B$-ΔM is due to the Ti-moment variation induced by a strong magnetoelectric coupling. For $L=2$, when the system becomes magnetically soft, M drops down to almost zero as shown in Fig. 3b. Then, with increasing the Fe film thickness $L>3$, M gradually approaches the bulk Fe magnetization. In Fig. 3c, we plot the interface ME coupling coefficient α versus L. It was defined as $\alpha = \Delta M/(E_c \cdot A)$, where A is the surface area and E_c is the coercive field needed to switch the polarization. Here, the experimental $E_c = 33$ kV/cm of PTO was used. In fact, α quickly decays with increasing L. This is obvious since the ME effect in composite multiferroic is confined to its interface.

In summary, we computed from first-principles the ferroic properties of $L \cdot Fe_2/PbTiO_3(001)$ near its ferromagnet/ferroelectric interface. We find the interface ME coupling rather strong in this prototype MF. The change in magnetic order seen between $1 \leq L \leq 3$, is understood in terms of hybridization of the electronic states. Our preliminary calculations suggest also that intrinsic oxidation [9] of composite MF may not significantly damage their magnetoelectricity.

2. Acknowledgment

References
[1] Schmid H 2008 *J Phys-Condens Mat* **20** 434201
[2] Eerenstein W, Wiora M, Prieto J L, Scott J F and Mathur N D 2007 *Nat Mater* **6** 348–351
[3] Fiebig M 2005 *J Phys D Appl Phys* **38** R123–R152
[4] Fechner M, Maznichenko I V, Ostanin S, Ernst A, Henk J, Bruno P and Mertig I 2008 *Phys Rev B* **78** 212406
[5] Yu C, Pechan M J, Srivastava S, Palmstrom C J, Biegaslski M, Brooks C and Schlom D 2008 *J Appl Phys* **103** 07B108
[6] Kresse G and Furthmüller J 1996 *Phys Rev B* **54** 11169–11186
[7] Fechner M, Ostanin S and Mertig I 2008 *Phys Rev B* **77** 094112
[8] Leung T, Chan C and Harmon B 1991 *Phys Rev B* **44** 2923–2927
[9] Fechner M, Ostanin S and Mertig I *submitted*

4. Effect of oxidation of the ultrathin Fe electrode material on the strength of magnetoelectric coupling in composite multiferroics

Effect of oxidation of the ultrathin Fe electrode material on the strength of magnetoelectric coupling in composite multiferroics

M. Fechner,[1,][*] S. Ostanin,[1] and I. Mertig[1,2]

[1]*Max-Planck-Institut für Mikrostrukturphysik, Weinberg 2, D-06120 Halle, Germany*
[2]*Fachbereich Physik, Martin-Luther-Universität Halle-Wittenberg, D-06099 Halle, Germany*
(Received 13 May 2009; revised manuscript received 23 July 2009; published 11 September 2009)

We present an *ab initio* study of the effect of iron oxidation on magnetoelectric coupling which appears at the ferromagnet/ferroelectric interface, such as $Fe_2/ATiO_3(001)$ (A=Ba,Pb). The oxygen coverage, c, ranging between one half and two adsorbed O per each Fe atom was simulated within a slab geometry. Since the change in magnetization induced by electric polarization reversal remains robust below $c < 3/2$, we suggest that the surface oxidation of composite multiferroics will not significantly damage their switchable magnetoelectricity.

I. INTRODUCTION

When any two of all four primary ferroic properties, i.e., ferroelectricity, ferromagnetism, ferroelasticity, and ferrotoroidicity coexist in the so-called multiferroic material[1] (MF), its symmetry is dramatically restricted.[2] In the absence of space-inversion and time-reversal symmetry, the occurrence of ferroelectricity and ferromagnetism in the same phase of a MF allows the observation of both a switchable electric polarization, **P**, and a switchable magnetization **M**. This phenomenon, in principle, allows to store information in nanometer-sized memories with four logic states.[3–5]

Although some single-phase MFs, such as $BiFeO_3$ and $RMnO_3$ (R: rare earths), were studied since the seventies, the search for novel multiferroics is not finished.[6] Moreover, their classification, which is based on the different mechanisms of induced polarity, has been revised since 2003 (see Ref. 7, and references therein) when the type-II class of magnetic MF was established. The type-I class of multiferroics contains numerous perovskitelike materials in which ferroelectricity and magnetism appear independently of one another and where **P** appears at higher temperatures than **M**. One can find several subclasses of type-I MF depending on the mechanism of their ferroelectricity.[7] In a type-II MF, ferroelectricity is driven by the electronic order degrees of freedom related to spin arrangements which break inversion symmetry. This symmetry breaking occurs due to a spin-orbit-related mechanism in conjunction mostly with the spin-spiral magnetic structure. For instance, this happens in $TbMnO_3$ below 28 K when the Mn spin tips sweep out a cycloid. Such cycloidal spin arrangement via the Dzyaloshinskii-Moria antisymmetric exchange creates a polarization: $\mathbf{P} \sim \mathbf{r_{ij}} \times [\mathbf{S_i} \times \mathbf{S_j}]$, where $\mathbf{r}_{ij}$ is the vector connecting neighboring spins $\mathbf{S}_i$ and $\mathbf{S}_j$. There is another subclass of the type-II multiferroics where ferroelectricity may appear for some collinear antiferromagnetic structures below the Néel temperature due to the Heisenberg-type symmetric exchange. Thus, ferroelectricity of the type-II MF is caused by a particular type of magnetic order, which exists only at low temperature and which is predominantly antiferromagnetic.

In multiferroics, no matter what its class is, an applied electric field, **E**, displacing the magnetic ions, may affect the magnetic exchange coupling or, vice versa, the external magnetic field, **H**, induces the electric polarization: $P_i \sim \alpha_{ij} H_j$, where α_{ij} is the magnetoelectric tensor and $(i,j)=x,y,z$. According to the Landau theory, the linear magnetoelectric[1] (ME) contribution to the Gibbs free energy is $\alpha_{ij} E_i H_j$. If α is sufficiently strong then **M** can be easily modified by **E**. It should be kept in mind that magnetoelectricity is an intrinsic bulk property for which the induction of **M** depends linearly on **E**. In the type-I single-phase MF, **P** and **M** weakly interact with each other and, therefore, α is marginal there. Besides, all these multiferroics possess a hierarchy of phase transformations,[8] where the magnetism disappears far below room temperature. In a type-II MF, the magnitude of **P** is never large. However these materials disclose a relatively large ME coupling. For instance, the direction of **P** in $TbMnO_3$ may flop by 90° when an applied magnetic field forces the plane of a magnetic cycloid to rotate by 90°. Obviously, the quest for fundamentally new multiferroics requires a better understanding of the mechanisms which mediate the ME coupling.

Ab initio calculations based on the density-functional theory (DFT) predict that a ~30 meV voltage, applied across the $SrRuO_3/SrTiO_3$ interface, with no magnetic cations, can induce a net magnetic moment.[9] Since the space-inversion symmetry is broken between the two unlike terminations, the ME effect results entirely from spin accumulation at the interface. The effect might be enhanced by the use of materials with higher spin polarization. Indeed, a more robust scenario of magnetoelectricity occurs in epitaxially grown two-phase MF consisting of ferroelectric and ferromagnetic components where the ME effect is mediated by strain across the biferroic interface. Inaccessible by conventional synthesis, composite MF exhibit specific properties which are superior to those of customary materials. The *ab initio* studies suggest that chemical bonding at the $Fe/BaTiO_3(001)$ interface is the source of strong ME coupling.[10,11] The interfacial Ti atoms show an induced magnetic moment of about 0.3 μ_B. Moreover, for the two opposite directions of **P** ($P_\downarrow$ and $P_\uparrow$), there are rather noticeable differences of 0.1–0.2 μ_B in the magnetic moments of Fe and Ti at the interface. This is a very promising phenomenon, which is entirely confined to the ferroelectric/ferromagnetic

interface and which is different from the bulk ME effect. The interface ME effect defines the change in magnetization at the coercive field E_c: $\mu_0 \Delta M \approx \alpha E_c$. The α of $\sim 2 \times 10^{-10}$ G cm^2/V estimated for Fe/BaTiO$_3$(001) from first principles, is two orders of magnitude larger than that predicted for SrRuO$_3$/SrTiO$_3$.

Epitaxial growth of the two-phase MF thin films of high quality continues to be very challenging. A 30-nm-thick Fe(001) film has been grown recently on a ferroelectric BaTiO$_3$(001) substrate.[12] For this MF composite, the interface ferromagnetic resonance mode is characterized by a large out-of-plane magnetic anisotropy comparable and opposite in sign to the shape anisotropy, which favors the in-plane easy axis for the thick-film interiors. The trends of magnetic anisotropy detected for Fe/BaTiO$_3$ are in a good agreement with the corresponding *ab initio* calculations.[11,13] In the case of one Fe monolayer (ML), the DFT predicts that perpendicular anisotropy is favored to in-plane anisotropy by 0.72 meV (0.54 meV) per Fe atom for $P_\downarrow$($P_\uparrow$).[11] Although the spin reorientation transition under switching of **P** is not found from first principles, the ME coupling alters the magnetocrystalline anisotropy energy by $\sim 50\%$. The magnetic order of Fe/BaTiO$_3$ can be tuned by the Fe layer thickness to almost zero-**M** ferrimagnetic upon deposition of a second Fe ML.[11] Ferromagnetic order is restored for the Fe films thicker than 3 ML where the shape anisotropy energy favors in-plane alignment of **M**.[13]

Recently, Niranjan *et al.*[14] modeling the two different Fe$_3$O$_4$/TiO$_2$/BaTiO$_3$(001) interfaces, within the DFT, have found that ME coupling is stronger for the O-deficient type of the Fe$_3$O$_4$ interface. The O-deficient termination of Fe$_3$O$_4$ contains Fe cations on tetrahedron sites, whereas the FeO$_2$-terminated magnetite surface contains Fe on octahedron sites in addition to oxygen anions. These interface O atoms reduce the hybridization between Fe and Ti thus decreasing the magnetic moment induced on Ti. This leads to the reduction in the ME effect for the O-rich Fe$_3$O$_4$/TiO$_2$ interface since its magnetoelectricity is primarily controlled by the Ti magnetic moments. Therefore, the presence of extra oxygen or oxygen vacancies at the biferroic interface plays an important role. The temperature-dependent magnetization curves of epitaxial magnetite films grown on BaTiO$_3$(001) demonstrate[15] a strong perpendicular magnetic anisotropy, which is modified by the piezoelectric response of the substrate.

So far, the *ab initio studies* of composite MF were focused on their perfect interfaces with no oxidants. However, the strength of the ME interface effect may be very sensitive to the degree of oxidation. The Fe oxidation is unavoidably motivated, first, by the growth process of the ferroelectric since oxygen remaining in the chamber will react with iron during its growth. Second, for the uncovered Fe films further oxidation occurs when the sample is removed from the chamber. These two possible scenarios may result in some particular Fe-O compositions, which vary from highly oxidized Fe to an almost clean surface. Thus, the *ab initio* based modeling would be extremely useful. In this work, we study from first principles the key electronic, magnetic, and structure factors behind the oxidation process of the 1 ML Fe grown on BaTiO$_3$(001) and PbTiO$_3$(001). We demonstrate in

which positions oxygen adatoms sit above the Fe layer and that the ME coupling is robust against the O adsorption.

II. METHOD

Our DFT calculations were performed within the local spin-density approximation, using the projector-augmented wave (PAW) pseudopotentials and a plane-wave basis cutoff energy of 650 eV, as implemented within the Vienna *ab initio* simulation package (VASP).[16,17] To model the (001) surface of BaTiO$_3$ (BTO) and highly polar PbTiO$_3$ (PTO), we constructed the 25-atom and 5-unit-cell (~ 2-nm)-thick perovskite supercell, with a vacuum spacer of 2 nm in the [001] direction. The lattice parameters were set to the equilibrium values of tetragonal ABO_3 (A=Ba and Pb and B=Ti).[18] For BTO (PTO), the in-plane lattice parameter, a, is 3.943 Å (3.858 Å) and c/a=1.013 (1.071). The corresponding bulk polarization values, calculated by the Berry phase approach[19,20] for BTO and PTO, are 0.23 and 0.94 C/m^2, respectively. The Ti/O displacements occurring in tetragonal PTO and BTO cause the direction of **P** along [001]. When **P** is antiparallel to the surface normal ($P_\downarrow$), oxygen is placed above the cations in each ML, and vice versa, the configuration $P_\uparrow$ means that all intralayer displacements $\delta = z_O - z_{cation} < 0$. Since the (001) surface of ABO_3 is TiO$_2$ terminated[18] for both directions of **P**, we study the Fe$_2$/TiO$_2$/BTO(001) and Fe$_2$/TiO$_2$/PTO(001) interfaces where the Fe atoms find their relaxed positions atop oxygen, as shown in Figs. 1(a) and 1(b). This is in agreement with previous *ab initio* calculations.[10,11]

The equilibrium bond length calculated for molecular O$_2$ is 1.23 Å. For Fe$_2$/TiO$_2$/ATiO$_3$(001), the in-plane lattice parameter is about 3.9 Å while the Fe-Fe separation is ~ 2.75 Å. The latter is two times larger than that of the O$_2$ dissociation. Thus, to model the Fe oxidation of Fe/BTO and Fe/PTO we consider O coverages, $c(O_x:Fe_2)$, ranging between $c = 1/2$ and two adsorbed O atoms per Fe atom ($c = 2$). There are 12 possible configurations shown in Fig. 1(c). For $c = 0.5$, one oxygen adatom per unit cell can occupy the site either above A or above Ti or, alternatively atop Fe. For $c = 1$, the two O adatoms form four configurations marked in Fig. 1(c) as AT, AF, TF, and FF. In the case of $c = 1.5$, we relax the ATF, TFF, and AFF configurations and, finally, for $c = 2$ there are two more possibilities to distribute four adatoms, such as ATFF (the case of full coverage) and 4H, which means that all four hollow sites are occupied by O. Using the $10 \times 10 \times 6$ Monkhorst-Pack[21] k-point mesh for the Brillouin-zone integration, we relaxed the O adatoms and Fe atoms plus all atoms of the two top ABO_3 unit cells until the forces were less than 1.0×10^{-2} eV/Å. After relaxation we found that oxygen adatoms for all coverages except $c = 2$ form an overlayer above the Fe layer with the distance depending on the coverage and direction of **P**. The total and site-projected partial density of states (DOS) as well as the local magnetic moments were calculated within the PAW option of VASP using the tetrahedron method and a dense k-point mesh. Additionally, to verify the calculated magnetic moments we varied the Wigner-Seitz radii of each atomic species in the cell. For $c = 0$, the local moments calculated by
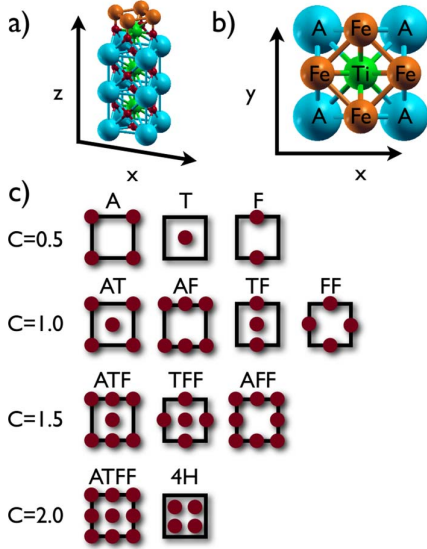
FIG. 1. (Color online) Unit cell of oxidized biferroic $O_x/Fe_2/TiO_2/ATiO_3(001)$ ($A=Ba,Pb$), with a 2-nm-thick vacuum layer. The top layers of the clean biferroic system ($x=0$), are plotted as side view and top view in panel (a) and (b), respectively. The lower panel (c) shows the O adatom positions, which mimic the oxygen coverage, $c(O_x:Fe_2)$, ranging between $c=1/2$ and two adsorbed O per Fe atom. For $c=1/2$, we relaxed the configurations marked with the labels A, T, and F, where an oxygen adatom can occupy any site above A, Ti, or Fe, respectively. In the case of $c=1$ ($c=3/2$), there are four (three) such configurations and, finally, for $c=2$ we consider a pair of possibilities, one of which marked as 4H means that all four hollow sites are occupied by O.

VASP are in good agreement with those of our previous work[11] in which another DFT code, the multiple-scattering Korringa-Kohn-Rostoker method, was used.

III. RESULTS AND DISCUSSION

In our study of an uncovered ML Fe on $ABO_3(001)$, we have found[11] a strong ferromagnetic order of the Fe layer with a magnetic moment of ≈ 3 μ_B. The reversal of the electric polarization induces a change in the total magnetization $\Delta M=M(P_\downarrow)-M(P_\uparrow)$ of 1 μ_B (0.05 μ_B) for Fe/PTO (Fe/BTO). This is mostly due to the interfacial-Ti magnetic moment, aligned antiparallel to that of Fe and originated from the hybridization of Ti $3d$ with minority-spin Fe $3d$ states. Reversal of **P** affects the hybridization making it stronger for $P_\downarrow$ when the distance between Fe and Ti becomes slightly shorter.

A. Structural optimization

In Fig. 2, we plot the total energy of $O_x/Fe_2/ATiO_3$ ($A=Ba,Pb$ and $1\leq x\leq 4$) for the two polarization directions and for each of the oxygen coverages between $c=0.5$ ($x=1$) and $c=2$ ($x=4$). The O configurations are labeled as shown in Fig. 1. For each c between 0.5 and 2, the lowest energy configuration is the zero energy. In the case of $c=0.5$, the most favorable is the configuration A. The differ-
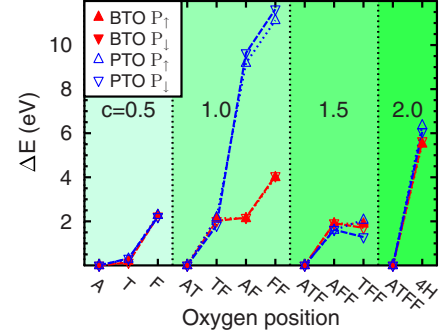

FIG. 2. (Color online) The total energy of $O_x/Fe_2/ATO_3(001)$ ($A=Ba,Pb$ and $1\leq x\leq 4$) is plotted for the 12 relaxed O configurations which are shown in Fig. 1. For each coverage c, the lowest energy configuration is the zero energy.

ence in energy between the configurations A and T for this O coverage is $E_T-E_A\sim 0.2$ eV. For the two ABO_3 substrates, the energetics are almost the same while the **P** reversal yields the energy differences compatible with that of E_T-E_A. When the O atom relaxes above Fe this results in the highly unfavorable configuration F, with the energy of 2.1 eV above that of case A. It can be understood by inspecting the relaxed structure of the A and T configurations. We find them very similar to that of a O/Fe(001) film, which were debated many times in the literature[22] and where the O adatom is relaxed at the hollow site ~ 0.3 Å above the Fe ML. The configurations A and T show no significant change with respect to each other and with respect to an uncovered ML Fe on ABO_3. In the case of configuration F, the coverage $c=0.5$ makes the two Fe sites nonequivalent and, as a result, the Fe atom below oxygen moves outward the Fe layer, displacing therefore the O atoms of the interface TiO_2 layer in the same way. The structural distortions make the configuration F energetically unfavorable.

The energetics which is calculated for the coverage $c=1$ can be explained using our findings for $c=0.5$. We expect the two O adatoms occupy the positions above A and Ti. Here, the **P** reversal gives a change in energy of about 0.2 eV for both systems. Any of the three other configurations: TF, AF, or FF always includes at least one energetically unfavorable position atop Fe that drastically increases the corresponding surface energy. The configuration FF after relaxation represents the case of the most distorted system, which energy is larger by 12 eV (4 eV) compared to that of the AT configuration of PTO (BTO). For the same reason, the energetically favorable scenario of $c=1.5$ is the configuration ATF when one site above Fe is empty. Regarding $c=2$, we have inspected two configurations: ATFF and 4H, which are shown in Fig. 1. It turns out that the 4H configuration, with all four hollow sites occupied by O, is unfavorable.

In Fig. 3 we plot the intralayer separation between the perovskite O and A/B cation along [001]: $\delta=z_O-z_{cation}$, obtained after relaxation in $O_x/Fe_2/ABO_3(001)$ for the most favorable configuration of each coverage. The adatom configurations A, AT, ATF, and ATFF were chosen for $0.5\leq c\leq 2$. The layers toward the perovskite bulk, starting from the outermost TiO_2 layer, are labeled I, I-1, I-2, etc. The δ ob-
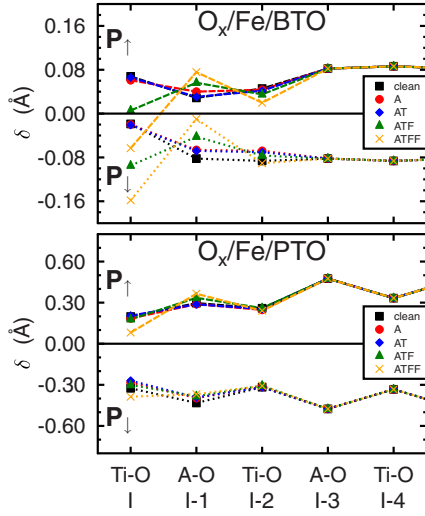
FIG. 3. (Color online) Intralayer atomic displacements $\delta = z_O - z_{cation}$ (in Å) are plotted for several perovskite layers of $O_x/Fe_2/ATiO_3(001)$ ($A = Ba, Ti$ and $x = 0, 1, 2, 3, 4$). The outermost TiO_2 layer of the ferroelectric is denoted I and the layers toward the perovskite bulk are labeled I-1, I-2, etc. For each O coverage $c \leq 2$ the lowest energy configuration (A, AT, ATF, and ATFF) was chosen.

tained for $c = 0$ are shown in Fig. 3 for comparison. The asymmetry of δ seen between $P_\downarrow$ and $P_\uparrow$ for the layers I, I-1, and I-2 as well as the magnitude of δ, which gradually decreases toward the interface, demonstrate the effect of the depolarizing field and its screening. The effect of oxidation which, in general, should provide less screening, may allow for a depolarizing field to reduce the magnitude of polarization. Here, we detect that for highly polar PTO the effect of oxidation is insignificant, except the O coverage $c = 2$. For BTO, this effect also plays no significant role when we exclude the two scenarios of excessive coverage: $c = 3/2$ and $c = 2$. When $c \leq 1$, the reduction in **P** is noticeable near the interface, however, the ferroelectrically dead layer is not seen there.

The most favored O coverage can be estimated using the calculation of adsorption energy,[23] which is defined as $E_{ad} = (E_{oxid} - E_{clean} - c \cdot E_{O_2})/x$. Here, $E_{oxid} - E_{clean}$ is the energy difference between the oxidized and clean surfaces of Fe_2/ABO_3, E_{O_2} is the energy of the O_2 molecule and x is the

number of oxygen adatoms. In Fig. 4, we plot the adsorption energy of $O_x/Fe_2/ATO_3(001)$ ($A = Ba, Pb$ and $1 \leq x \leq 4$) versus the O coverage, $c = x/2$, between 0.5 and 2. For the PTO substrate, there is a pronounced minimum of E_{ad} seen in Fig. 4 at $c = 1$. The **P** reversal shows a minor effect regardless of the substrate. However, in the case of $O_x/Fe_2/BaTiO_3(001)$,

FIG. 5. (Color online) Ionic bond lengths between Fe and oxygen adatoms in $O_x/Fe_2/BTO$ and $O_x/Fe_2/PTO$. The configurations with adatoms above A, Ti, and Fe were used. When $c = 2$ the O_A and O_T adatoms find their relaxed positions below the Fe layer.
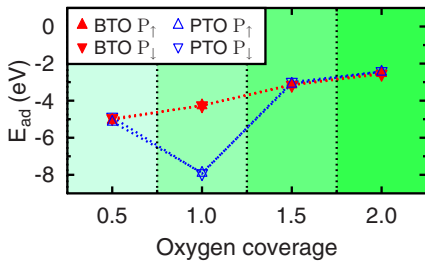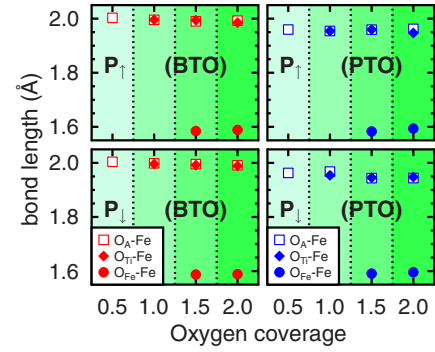

FIG. 4. (Color online) Adsorption energy of $O_x/Fe_2/ATiO_3(001)$ ($A = Ba, Pb$ and $x = 1, 2, 3, 4$) plotted as a function of $c = x/2$.
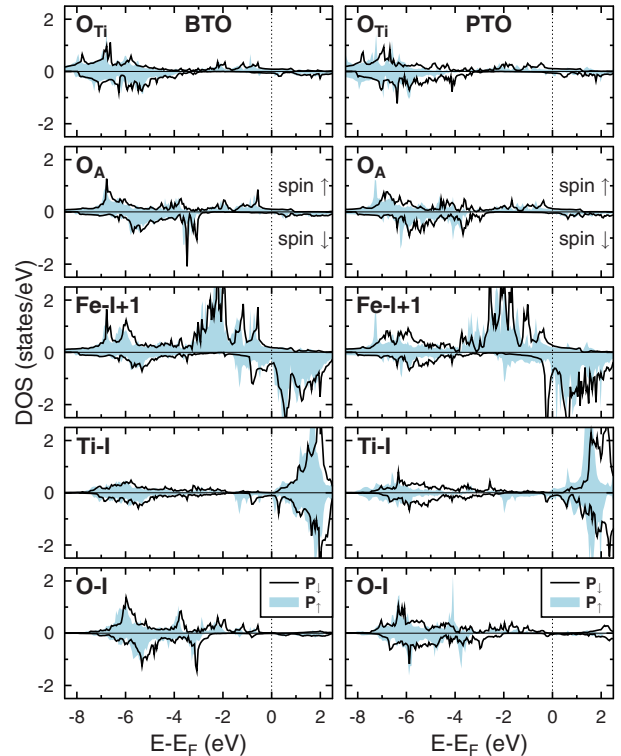

FIG. 6. (Color online) The spin-resolved DOS at the TiO_2-terminated interface of $O_2/Fe_2/BTO(001)$ (left) and $O_2/Fe_2/PTO(001)$ (right). The DOS projected on the O adatoms O_A and O_{Ti} are plotted in the two top panels. The middle panel shows the Fe local DOS while the two lower panels show the DOS calculated for the interfacial Ti and O atoms. Solid lines and shaded plots are the DOS for the polarization $P_\downarrow$ and $P_\uparrow$, respectively. The vertical line indicates the Fermi energy.

TABLE I. Local magnetic moments m_i (in μ_B) calculated for the Fe atom, interfacial Ti-I and O-I and O adatoms of $O_x/Fe_2/TiO_2/ATiO_3(001)$ ($A=$Ba,Pb and $x=0,1,2$). The two O adatoms above the Ti and A sites are labeled as O_T and O_A.

m_i	$x=0$		$x=1$		$x=2$	
	$P_\downarrow$	$P_\uparrow$	$P_\downarrow$	$P_\uparrow$	$P_\downarrow$	$P_\uparrow$
			$O_x/Fe_2/BTO$			
O_T					0.21	0.19
O_A			0.20	0.20	0.26	0.27
Fe	2.81	2.83	2.91	2.85	3.21	3.18
Ti-I	−0.22	−0.30	−0.24	−0.34	−0.18	−0.26
O-I	0.08	0.09	0.11	0.10	0.11	0.11
			$O_x/Fe_2/PTO$			
O_T					0.23	0.13
O_A			0.22	0.19	0.24	0.24
Fe	2.87	2.63	3.03	2.66	3.13	2.91
Ti-I	0.00	−0.35	−0.01	−0.39	−0.01	−0.29
O-I	0.10	0.04	0.14	0.07	0.12	0.08

the adsorption energy is rather smooth with no minimum between $0.5<c<2$. It seems that the BTO substrate tends to favor the low c values, namely, $c=0.5$.

The dissimilar behavior of PTO and BTO at the metal interface has been recently studied from first principles by Stengel *et al.*,[24] who analyzed the structure with the use of the ionic bond lengths. Concerning the difference seen in Fig. 4 between the two substrates, a simple explanation can be done by inspecting the O-Fe bond lengths for the O adatoms.

In Fig. 5, we plot the equilibrium O-Fe distances calculated for $O_x/Fe_2/ATiO_3(001)$. Comparing the two systems, the O-Fe separation is always shorter in O/Fe/PTO than in O/Fe/BTO, indicating that the O-Fe bond is stronger in the former system. In particular, for the PTO substrate and coverage $c=1$, the bond length of 1.96 Å between oxygen adatom and Fe is about 0.04 Å shorter than that of the BTO substrate. It seems that oxygen adatom on top of Fe/BTO is weakly bonded to Fe as compared to the Fe/PTO system. This can cause the dissimilarity of PTO and BTO seen in their E_{ad}. The effect of **P** reversal on the O-Fe bond is minor, as shown in Fig. 5. When the O coverage becomes denser, some visible variations in the bond lengths may occur. It should be noted that for the coverages $c=1.5$ and $c=2$, i.e., when extra O adatoms occupy the sites above Fe, this results in relatively short bond lengths of about 1.6 Å. This bond length also varies insignificantly with increasing $c>1.5$. Interestingly, in the case of $c=2$ oxygen atoms, which might occupy the positions above A and Ti, move inward and find their relaxed positions below the Fe layer at nearly the same distance of ∼1.95 Å to Fe as those of O_A/O_T adatoms of less dense c.

B. Magnetic properties and magnetoelectric coupling

The spin-resolved and site-projected DOS of $O_2/Fe_2/$ BTO and $O_2/Fe_2/$PTO for the coverage $c=1$ are plotted in Fig. 6. We show the local DOS calculated for the interfacial Fe, Ti-I, O-I, and two O adatoms. At the interface, we detect metallic behavior. The electronic hybridization between the Fe $3d$, Ti $3d$, and O $2p$ states induces magnetic moments at the interfacial Ti-I and O-I. In particular, the Ti moments, aligned antiparallel to those of Fe and O-I, originate from the hybridization of Ti $3d$ with minority-spin Fe $3d$ states. For bulk BTO/PTO as well as for BTO/PTO blocks distant from the interface, we obtained a fundamental band gap of about 2 eV while the unoccupied Ti d states form the lower conduction band. It is well known that *ab initio* calculations within the LDA tends to underestimate the band gap of polar perovskites. When theory goes beyond LDA this does not affect the empty conduction band whereas the metalliclike DOS at the interface together with the band gap can be quantitatively affected. As the result, the magnetic contributions to the ME effects coming from the Ti-I and Fe atoms might be slightly disproportionally changed compared to those of the LDA calculation. We believe, however, that the impact of electronic correlations is minor here.

For the two dually polar $O_x/Fe/ATiO_3(001)$ systems and $x\leq4$, the energy difference calculated between the ferromagnetic (FM) and antiferrimagnetic configurations indicates that the FM order is always preferable. Table I collects the local magnetic moments of $O_x/Fe_2/TiO_2/ATiO_3(001)$, which were calculated for the Fe atom, interfacial Ti-I and O-I and oxygen adatoms (O_{ad}). The number of adatoms varies in Table I from $x=0$ to $x=2$. We show the data for the most favored atomic configuration of each coverage $c\leq1$. For $x=1$ the O_A configuration is preferable. When $x=2$ there are two oxygen adatoms which occupy the sites O_T and O_A above Ti and A, respectively. Considering the Fe magnetic moments, which all are significantly enhanced with respect to the Fe bulk value, one can notice that m_{Fe} increases with increasing c. For $P_\downarrow$, the Fe magnetic moment of $O_x/Fe/PTO$ is larger than that of $O_x/Fe/BTO$ (with one ex-
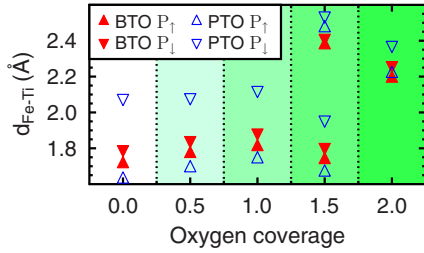
FIG. 7. (Color online) The distance between the Fe and Ti-I layers in $O_x/Fe_2/ATiO_3(001)$.

ception for $x=2$) and, vice versa, $m_{Fe}(PTO) < m_{Fe}(BTO)$ for $P_\uparrow$. As a result, the change in m_{Fe} due to the polarization reversal is always larger for PTO compared with the BTO system. For all x and both **P**, the O magnetic moments induced on O-I and O_{ad} are parallel to those of Fe. For the O adatoms at $x=1,2$ we obtained an averaged magnetic moment of 0.2 μ_B, which is two times larger than that of interfacial O from the TiO$_2$ layer. Reversal of P affects the O magnetic moments less significantly than m_{Fe} and m_{Ti}. We analyzed the magnetic moments of some energetically unfavored configurations. In particular, the energy splitting between BTO and PTO, seen in Fig. 2 at $c=1$, originates mostly from the magnetism of $O_2/Fe_2/BTO$, which is significantly suppressed for the two highly unexpected configurations AF and FF. The total magnetization of $O_2/Fe_2/BTO$, for instance, may drop below 0.1 μ_B per cell when both oxygen adatoms relax above Fe.

The hybridization between the $3d$ states of Fe and Ti leads to an induced magnetic moment on the Ti-I site, which is oriented opposite to m_{Fe}. This is shown in Table I. The antiferromagnetically oriented magnetic moment of interfacial Ti contributes significantly to ΔM. Surprisingly, for the $P_\downarrow$ state of $O_x/Fe/PTO$, we get $m_{Ti} \rightarrow 0$. This needs a careful analysis of the structure. In Fig. 7, we show the distance, $d_{Fe\text{-}Ti}$, between the Fe and Ti-I layers in $O_x/Fe_2/ATiO_3(001)$ for each coverage. When $c \leq 1$, the Fe-Ti distance is systematically shorter for $P_\uparrow$ and, therefore, the corresponding m_{Ti} is larger than that of the $P_\downarrow$ state. In $O_x/Fe/PTO$, the magnitude of $d_{Fe\text{-}Ti}$ increases noticeably for $P_\downarrow$, as shown in Fig. 7. This weakens the d-state hybridization of Fe and Ti leading to marginal m_{Ti}. For the coverage $c=1.5$, one oxygen adatom relaxed above Fe yields the second set of $d_{Fe\text{-}Ti}$, with the magnitudes ~ 0.6 Å larger than that of uncovered Fe. For $c=2$, when both Fe are covered by O adatoms we obtained again a single set of $d_{Fe\text{-}Ti}$. In the case of $c=1.5$ and $c=2$, the magnetic moment of Ti-I changes not so dramatically as the magnetic moments of a pair of covered Fe and its shortly distanced O adatom. For the former, we obtained a 1 μ_B reduction from ~ 3 to 2 μ_B per m_{Fe}, while the topmost O adatom above Fe shows the moment of ~ 0.5 μ_B. Meanwhile all other O adatoms of these configurations, which are labeled as O_A and O_T, show the magnetic moment of 0.12 μ_B or even less than 0.06 μ_B that happens at $c=2$ when O_A/O_T is positioned below the Fe layer. Since both high coverages $c=1.5$ and $c=2$ are energetically not preferable, we do not focus on their magnetic properties.

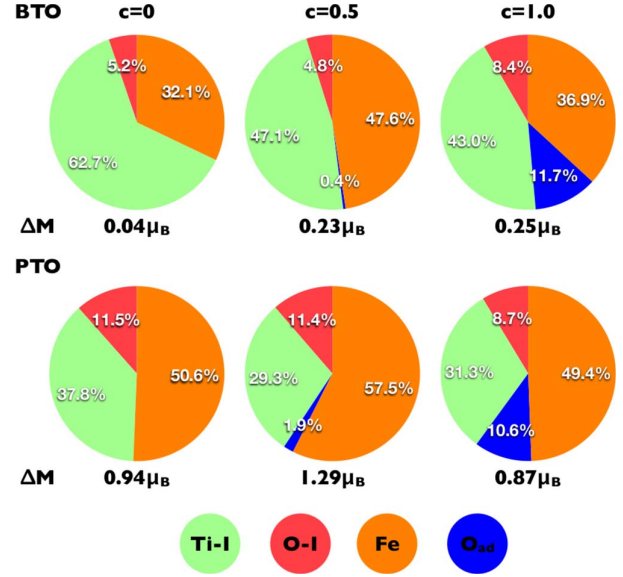The magnetic contributions of each species of $O_x/Fe/ATiO_3(001)$ to the total magnetization change, ΔM,

FIG. 8. (Color online) Relative contributions of each magnetic species to the magnetization change, ΔM, induced in $O_x/Fe_2/ATiO_3(001)$ ($A=Ba, Pb$ and $x=0,1,2$) due to the polarization reversal. The contributions from the two Fe atoms, one interfacial Ti (Ti-I), two interfacial O (O-I) and oxygen adatoms (O_{ad}) were counted. There are two O adatoms for the coverage $c=1$ and one adatom for $c=0.5$. The total ΔM values are shown below each diagram.

induced by the **P** reversal are shown in Fig. 8. We counted there the contributions from the two Fe atoms, one interfacial Ti, two O-I, and a number of oxygen adatoms. There are two oxygen adatoms for $c=1$ and one O adatom per cell for $c=0.5$. Figure 8 clearly illustrates the dissimilar behavior of BTO and PTO. For an uncovered ML Fe on BTO, we find that almost two-thirds of $\Delta M \approx 0.04$ μ_B comes from Ti-I while the two Fe atoms bring one-third only. With increasing $c \leq 1$, the Ti contribution to ΔM in this system gradually decreases whereas all ferromagnetically ordered Fe and O contribute $>50\%$. As a result, ΔM in $O_x/Fe/BTO$ increases to the value of 0.25 μ_B per cell at $c=1$. In Fe/PTO with no oxygen adatoms, one half of its $\Delta M=1$ μ_B comes from Fe. In $O_x/Fe/PTO$, the **P**-induced change in its M follows the Fe proportion: first, ΔM reaches the 1.3 μ_B maximum at $c=0.5$ and then, with increasing c from 1/2 to 1, it diminishes below 0.9 μ_B. Nevertheless, the effect may result in rather strong ME coupling.

In the top panel of Fig. 9 we show the total **M**, calculated including the interstitial contributions for the lowest energy configuration of $O_x/Fe_2/ATiO_3$ for each O coverage. There are the configurations A, AT, ATF, and ATFF obtained for $c=0.5, 1, 1.5,$ and 2, respectively. The magnetization of uncovered Fe/PTO and Fe/BTO is also shown in Fig. 9. The increase in **M** seen for $c=0.5$ and $c=1$, as compared to that of $c=0$, is partially due to an induced magnetic moment of the O adatom, which is aligned parallel to the Fe magnetic moment. Besides, for $c=0.5$ and $c=1$, the Fe moment value is enhanced by the presence of the adatom. Contrarily, when the O adatom relaxes above Fe in the configurations ATF and
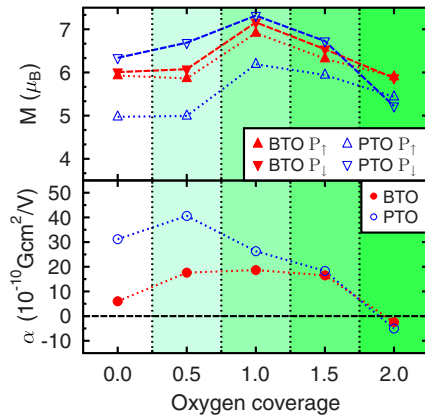
FIG. 9. (Color online) Total magnetization of the $O_x/Fe_2/ATiO_3(001)$ cell ($A = $ Ba,Pb and $0 < x < 4$) is plotted as a function of oxygen coverage in the top panel. For each coverage the most favorable configuration was used. The corresponding magnetoelectric coupling coefficient is plotted in the lower panel.

ATFF, the Fe magnetic moment is decreased by ~ 1 μ_B. This is mostly due to a relatively short separation between the O adatom and Fe along [001]. As a result, the value of **M** gradually decreases with increasing $c > 1$. For the magnetoelectric coupling the change in the magnetization induced by polarization reversal: $\Delta M = M(P_\downarrow) - M(P_\uparrow)$ is an important quantity. Previously, we have found[11] that for the uncovered 1 ML Fe on PTO (BTO) its $\Delta M \sim 1.2$ μ_B (~ 0.1 μ_B). Here it is obvious that in the case of O/Fe/BTO the magnitude of ΔM remains rather stable for O coverages < 1.5 and then with further increase in c, $\Delta M \rightarrow 0$ at $c = 2$. For the PTO substrate, the trends of ΔM computed for $c > 1.5$ are similar to those of BTO. It should be kept in mind that the dense coverage of $c = 2$ is unrealistic since the highest oxidation state of iron seen in Fe_2O_3 mimics the coverage $c = 1.5$.

The interface ME coupling coefficient, α, can be evaluated as the ratio of the surface magnetization change $\mu_0 \Delta \mathbf{M}/S$ and the coercive field E_c, where S is the interface area. The experimental $E_c = 10$ kV/cm and $E_c = 33$ kV/cm were used for Fe/BTO and Fe/PTO, respectively. In Fig. 9, we plot the calculated α vs c. In general, α, as a function of c, follows the trends of ΔM. We find that the two systems obey almost the same strength of α when $1 < c < 1.5$. However, for the most favorable O coverage, $c = 1$, the use of the

highly polar PTO substrate may result in the largest ME effect. Niranjan *et al.*[14] reported that for the O-rich interface between magnetite and BTO, which formally corresponds to $c = 2$, the value of α is smaller by a factor of 3, compared to that of the oxygen-free-type interface of Fe_3O_4. For a single Fe layer on BTO, we detect very similar trends of ME coupling seen in Fig. 9 comparing the results between the O coverage $c = 2$ and $c = 0$.

Since this work uses the local spin-density approximation to DFT, one can speculate that the model can incorrectly prescribe spin polarization to the p orbitals of oxygen adatom. Indeed, for any Fe-O system there are two competing phenomena: the electronic correlation and hybridization of their Fe $3d$ and O $2p$ orbitals. The electronic correlation effects can quantitatively contribute to the magnetic properties of ultrathin composite multiferroics. To deal with the on-site Coulomb correlations of $O_x/Fe/TiO_2$ more flexibly, it is worthwhile, therefore, to carry out more *ab initio* calculations beyond the conventional LDA.

IV. CONCLUSIONS

In summary, we present an *ab initio* study of the effect of oxidation on the strength of magnetoelectric coupling seen at the ferromagnet/ferroelectric interface in epitaxial multiferroics. The oxygen coverage, ranging between $c = 0.5$ and two adsorbed O per Fe atom were simulated for $O_x/Fe_2/$ $BaTiO_3(001)$ and $O_x/Fe_2/PbTiO_3(001)$ multiferroics. We suggest that oxygen adatoms may find their relaxed positions atop the Ba(Pb) and/or Ti sites. For $c > 1$, the magnetic properties computed for the Fe layer gradually degrade with increasing O coverage. However, when $c < 1.5$ the change in magnetization induced by polarization reversal is robust for all energetically preferable compositions. On the basis of our calculations we, therefore, suggest that intrinsic oxidation of biferroics may not significantly damage their magnetoelectricity. In the case of realistic oxygen coverage ($c = 1$), we expect that the strength of magnetoelectric coupling remains rather strong for both MF systems under consideration.

ACKNOWLEDGMENTS

*fechner@mpi-halle.mpg.de

[1] K. F. Wang, J. M. Liu, and Z. F. Ren, Adv. Phys. **58**, 321 (2009).

[2] H. Schmid, J. Phys.: Condens. Matter **20**, 434201 (2008).

[3] W. Eerenstein, M. Wiora, J. L. Prieto, J. F. Scott, and N. D. Mathur, Nature Mater. **6**, 348 (2007).

[4] S.-W. Cheong, Nature Mater. **6**, 927 (2007).

[5] F. Zavaliche, T. Zhao, H. Zheng, F. Straub, M. P. Cruz, P.-L. Yang, D. Hao, and R. Ramesh, Nano Lett. **7**, 1586 (2007).

[6] M. Dawber, K. M. Rabe, and J. F. Scott, Rev. Mod. Phys. **77**,

1083 (2005).

[7] D. Khomskii, Phys. **2**, 20 (2009).

[8] M. Fiebig, J. Phys. D: Appl. Phys. **38**, R123 (2005).

[9] J. M. Rondinelli, M. Stengel, and N. A. Spaldin, Nat. Nanotechnol. **3**, 46 (2008).

[10] C.-G. Duan, S. S. Jaswal, and E. Y. Tsymbal, Phys. Rev. Lett. **97**, 047201 (2006).

[11] M. Fechner, I. V. Maznichenko, S. Ostanin, A. Ernst, J. Henk, P. Bruno, and I. Mertig, Phys. Rev. B **78**, 212406 (2008).

[12] C. Yu, M. J. Pechan, S. Srivastava, C. J. Palmstrøm, M. Biegalski, C. Brooks, and D. Schlom, J. Appl. Phys. **103**, 07B108 (2008).

[13] C.-G. Duan, J. P. Velev, R. F. Sabirianov, W. N. Mei, S. S. Jaswal, and E. Y. Tsymbal, Appl. Phys. Lett. **92**, 122905 (2008).

[14] M. K. Niranjan, J. P. Velev, C.-G. Duan, S. S. Jaswal, and E. Y. Tsymbal, Phys. Rev. B **78**, 104405 (2008).

[15] C. A. F. Vaz, J. Hoffman, A.-B. Posadas, and C. H. Ahn, Appl. Phys. Lett. **94**, 022504 (2009).

[16] G. Kresse and J. Furthmüller, Phys. Rev. B **54**, 11169 (1996).

[17] J. Hafner, J. Comput. Chem. **29**, 2044 (2008).

[18] M. Fechner, S. Ostanin, and I. Mertig, Phys. Rev. B **77**, 094112 (2008).

[19] D. Vanderbilt and R. D. King-Smith, Phys. Rev. B **48**, 4442 (1993).

[20] R. Resta, Rev. Mod. Phys. **66**, 899 (1994).

[21] H. J. Monkhorst and J. D. Pack, Phys. Rev. B **13**, 5188 (1976).

[22] R. Wu and A. Freeman, J. Magn. Magn. Mater. **127**, 327 (1993).

[23] P. Blonski, A. Kiejna, and J. Hafner, Surf. Sci. **590**, 88 (2005).

[24] M. Stengel, D. Vanderbilt, and N. A. Spaldin, Nature Mater. **8**, 392 (2009).

SUMMARY

The aim of this work was to investigate the magnetoelectric effect at multiferroic interfaces. It was motivated by recent experiments on composite multiferroics made of $BaTiO_3$ and $La_{0.67}Sr_{0.33}MnO_3$ [15] and theoretical investigations [101] of $Fe/BaTiO_3$ superlattices. First principle methods that rely on density functional theory were used for the study.

The first investigation considered clean ferroelectric surfaces of $BaTiO_3$, $PbTiO_3$ and non-ferroelectric $SrTiO_3$. It was found that the preferred surface termination is TiO_2 for the ferroelectrics. However, for non-polar $SrTiO_3$ both terminations (SO and TiO_2) are equal with respect to energy. Furthermore, the changed coordination number of Ti at the surface causes a shift of the oxygen by 0.1 Å above Ti. Due to this, the polarization at the surface is suppressed. The strength of the suppression depends on the direction of $\mathbf{P}$. A polarization reversal changes the behavior of the surface layer from metallic to insulating, which changes the surface conductance drastically.

In the following the magnetoelectric coupling of two component multiferroics was studied on. They were realized by $ATiO_3(001)$ (A=Ba,Pb) perovskites in combination with Fe and Co films. It turned out that the magnetic order of the composite multiferroic in the case of Fe films was sensitive to the thickness. A ferromagnetic to antiferrimagnetic to ferromagnetic transition was observed, which was not present for Co. Furthermore, the polarization affected the magnetization at the interface due to a hybridization effect. However, a spin-reorientation transition under switching of the polarization was not found. Nevertheless, already small modifications within the system with 2 ML of Fe on $BaTiO_3$ allowed to gain control on the magnetic ordering. The two suggestions were a substitution of the interface TiO_2 layer by CrO_2 or alloying the Fe with Co. The modifications permitted the change of magnetic ordering by polarization reversal.

The observed change of magnetization at the interfaces was further studied in the case of an oxidized ferromagnetic layer. Therefore, oxygen coverages, ranging between c = 0.5 and 2 adsorbed O per Fe atom were simulated for $O_x/Fe_2/BaTiO_3(001)$ and $O_x/Fe_2/PbTiO_3(001)$ multiferroics. The result showed that oxygen adatoms found their relaxed positions atop the Ba/Pb and/or Ti sites. For c > 1, the magnetic properties computed for the Fe layer gradually

degrade with increasing O coverage. However, even for c=1.5 the change in magnetization induced by polarization reversal was robust for all energetically preferable compositions. Therefore, the intrinsic oxidation of multiferroic composites may not significantly damage their magnetoelectricity.

In summary, the study gave a detailed insight in the mechanism for the magnetoelectric coupling at ferroelectric/ferromagnetic interfaces. The underlying coupling mechanisms have been identified and successfully applied for new systems, where the control of the magnetization via the polarization is possible.

Bibliography

[1] **D. N. Astrov**. Sov. Phys.—JETP **11,** 708 (1960).

[2] **W. Eerenstein**, **N. D. Mathur**, **J. F. Scott**. *Multiferroic and magnetoelectric materials*. Nature **442,** 759–765 (2006).

[3] **M. Bibes**, **A. Barthelemy**. *Multiferroics: Towards a magnetoelectric memory*. Nat. Mater **7 (6),** 425–426 (2008).

[4] **W. F. Brown**, **R. M. Hornreich**, **S. Shtrikman**. *Upper bound on magnetoelectric susceptibility*. Phys. Rev. **168 (2),** 574–& (1968).

[5] **N.A. Spaldin**, **M. Fiebig**. *The renaissance of magnetoelectric multiferroics*. Science **309 (5733),** 391–392 (2005).

[6] **T. Kimura**, **T. Goto**, **H. Shintani**, **K. Ishikawa**, **T. Arima**, **Y. Tokura**. *Magnetic control of ferroelectric polarization*. Nature **426 (6962),** 55–58 (2003).

[7] **K. H. Shin**, **M. Inoue**, **K. I. Arai**. *Preparation and properties of elastically coupled electro-magnetic elements with a bonding structure*. IEEE T. Magn. **34 (4),** 1324–1326 (1998).

[8] **H. Schmid**. *Multi-ferroic magnetoelectrics*. Ferroelectrics **162 (1),** 317–338 (1994).

[9] **M. Fiebig**. *Revival of the magnetoelectric effect*. J. Phys. D Appl. Phys. **38 (8),** R123–R152 (2005).

[10] **N. A. Hill**. *Why are there so few magnetic ferroelectrics?* J. Phys. Chem. B **104 (29),** 6694–6709 (2000).

[11] **T. Lottermoser**, **T. Lonkai**, **U. Amann**, **D. Hohlwein**, **J. Ihringer**, **M. Fiebig**. *Magnetic phase control by an electric field*. Nature **430 (6999),** 541–544 (2004).

[12] **E. Y. Tsymbal**, **H. Kohlstedt**. *Applied physics - Tunneling across a ferroelectric*. Science **313 (5784),** 181–183 (2006).

[13] **V. Garcia, M. Bibes, L. Bocher, S. Valencia, F. Kronast, A. Crassous, X. Moya, S. Enouz-Vedrenne, A. Gloter, D. Imhoff, C. Deranlot, N. D. Mathur, S. Fusil, K. Bouzehouane, A. Barthelemy**. *Ferroelectric Control of Spin Polarization*. Science **327 (5969),** 1106–1110 (2010).

[14] **M. Gajek, M. Bibes, S. Fusil, K. Bouzehouane, J. Fontcuberta, A. Barthelemy, A. Fert**. *Tunnel junctions with multiferroic barriers*. Nat. Mater **6,** 296–302 (2007).

[15] **W. Eerenstein, M. Wiora, J. L. Prieto, J. F. Scott, N. D. Mathur**. *Giant sharp and persistent converse magnetoelectric effects in multiferroic epitaxial heterostructures*. Nat. Mater **6,** 348–351 (2007).

[16] **P. Hohenberg, W. Kohn**. *Inhomogeneous electron gas*. Phys. Rev. B **136 (3B),** B864–& (1964).

[17] **W. Kohn**. *Highlights of Condensed Matter Theory*. Amsterdam (1985).

[18] **P. E. Blöchl**. *Projector augmented-wave method*. Phys. Rev. B **50,** 17 953–17 979 (1994).

[19] **L. D. Landau, E. M. Lifschitz**. *Elektrodynamik der Kontinua* 8. Akademie-Verlag Berlin (1985).

[20] **J. D. Jackson**. *Klassische Elektrodynamik* 3. Walter de Gruyter (2003).

[21] **P. Ghosez, J. Junquera**. *Handbook of Theoretical and Computational Nanotechnology* 134. American Scientific Publishers (2006).

[22] **K. M. Rabe, C. H. Ahn, J. M. Triscone**. *Physics of Ferroelectrics*. Springer Berlin (2007).

[23] **J. Valasek**. *Piezoelectric and allied phenomena in Rochelle salt*. Phys. Rev. **15,** 537 (1920).

[24] **M. E. Lines, A. M. Glass**. *Principles and Applications of Ferroelectrics and Related Materials*. Oxford University Press, USA (2001).

[25] **T. Tybell, P. Paruch, T. Giamarchi, J.M. Triscone**. *Domain wall creep in epitaxial ferroelectric Pb(Zr0.2Ti0.8)O-3 thin films*. Phys. Rev. Lett. **89 (9),** 097 601 (2002).

[26] **R.E. Cohen**. *Origin of ferroelectricity in perovskite oxides*. Nature **358,** 136–138 (1992).

[27] **R.E. Cohen**. *Theory of ferroelectrics: a vision for the next decade and beyond*. J Phys. Chem. Solids **61 (2),** 139–146 (2000).

[28] **H.D. Megaw**. *Origin of ferroelectricity in barium titanate and other perovskite-type crystals*. Acta Crystallogr. **5 (6),** 739–749 (1952).

[29] **U. Opik**, **M.H.L. Pryce**. *Studies of the Jahn-Teller effect 1. A Survey of the static problem*. Proc. R Soc. Lon. Ser-A **238 (1215),** 425–447 (1957).

[30] **R.F.W. Bader**. *An interpretation of potential interaction constants in terms of low-lying excited states*. Mol. Phys. **3 (2),** 137–151 (1960).

[31] **P.S. Halasyamani**, **K.R. Poeppelmeier**. *Noncentrosymmetric oxides*. Chem. Mater. **10 (10),** 2753–2769 (1998).

[32] **I.B. Bersuker**. *Modern aspects of the Jahn-Teller effect theory and applications to molecular problems*. Chem Rev **101 (4),** 1067–1114 (2001).

[33] **H.A. Jahn**, **E. Teller**. *Stability of polyatomic molecules in degenerate electronic states. I. Orbital degeneracy*. Proceedings of the Royal Society of London. Series A, Mathematical and Physical Sciences **161 (905),** 220–235 (1937).

[34] **A. Filippetti**, **N. A. Hill**. *Coexistence of magnetism and ferroelectricity in perovskites*. Phys. Rev. B **65 (19),** 195 120 (2002).

[35] **R.E. Cohen**, **H. Krakauer**. *Electronic-structure studies of the differences in ferroelectric behavior of $BaTiO_3$ and $PbTiO_3$*. Ferroelectrics **136 (1-4),** 65–83 (1992).

[36] **W. Zhong**, **D. Vanderbilt**, **K. M. Rabe**. *Phase-transitions in* $BaTiO_3$ *from first principles*. Phys. Rev. Lett. **73,** 1861–1864 (1994).

[37] **J. Junquera**, **P. Ghosez**. *Critical thickness for ferroelectricity in perovskite ultrathin films*. Nature **422,** 506–509 (2003).

[38] **Y.S. Kim**, **D.H. Kim**, **J.D. Kim**, **Y.J. Chang**, **T.W. Noh**, **J.H. Kong**, **K. Char**, **Y.D. Park**, **S.D. Bu**, **J.G. Yoon**, **J.S. Chung**. *Critical thickness of ultrathin ferroelectric $BaTiO_3$ filMS*. Appl. Phys. Lett. **86 (10),** 102 907 (2005).

[39] **D. D. Fong**, **G. B. Stephenson**, **S. K. Streiffer**, **J. A. Eastman**, **O. Auciello**, **P. H. Fuoss**, **C. Thompson**. *Ferroelectricity in ultrathin perovskite films*. Science **304,** 1650–1653 (2004).

[40] **C. Ederer**, **N. A. Spaldin**. *Effect of epitaxial strain on the spontaneous polarization of thin film ferroelectrics*. Phys. Rev. Lett. **95,** – (2005).

[41] **N. Sai**, **A. M. Kolpak**, **A. M. Rappe**. *Ferroelectricity in ultrathin perovskite films*. Phys. Rev. B **72,** 020 101 (2005).

[42] **N. A. Spaldin**. *Fundamental size limits in ferroelectricity*. Science **304,** 1606–1607 (2004).

[43] **W. Nolting**. *Grundkurs Theoretische Physik 3: Elektrodynamik*. Springer, Berlin (2007).

[44] **E. Stoner**. *Atomic moments in ferromagnetic metals and alloys with non- ferromagnetic elements*. Philosophical Magazine Series 7 **15,** 1018–1034 (1933).

[45] **M. Getzlaff**. *Fundamentals of Magnetism*. Springer Verlag (2007).

[46] **W. C. Röntgen**. *Beschreibung des Apparates, mit welchem die Versuche über die electrodynamische Wirkung bewegter Dielectrica ausgeführt wurden*. Ann. Phys. **35,** 264 (1888).

[47] **P. Debye**. *Bemerkung zu einigen neuen Versuchen über einen magneto-elektrischen Richteffekt*. Zeitschrift für Physik A Hadrons and Nuclei (1926).

[48] **I. E. Dzyaloshinskii**. Sov. Phys.—JETP **10,** 628 (1959).

[49] **G.A. Gehring**. *On the microscopic theory of the magnetoelectric effect*. Ferroelectrics **161 (1),** 275–285 (1994).

[50] **R. Hornreich**, **S. Shtrikman**. *Statistical Mechanics and Origin of the Magnetoelectric Effect in Cr_2O_3*. Phys. Rev. **161 (2),** 506–& (1967).

[51] **J. M. Rondinelli**, **M. Stengel**, **N. A. Spaldin**. *Carrier-mediated magnetoelectricity in complex oxide heterostructures*. Nature Nanotech **3,** 46–50 (2008).

[52] **D. Khomskii**. *Classifying multiferroics: Mechanisms and effects*. Physics **2 (20),** 1–8 (2009).

[53] **H. Schmid**. *Some symmetry aspects of ferroics and single phase multiferroics*. J Phys.-Condens. Mat. **20 (43),** 434 201 (2008).

[54] **J. B. Neaton**, **C. Ederer**, **U.V. Waghmare**, **N. A. Spaldin**, **K.M. Rabe**. *First-principles study of spontaneous polarization in multiferroic $BiFeO_3$*. Phys. Rev. B **71 (1),** 014 113 (2005).

[55] **D.V. Efremov**, **J. Van den Brink**, **D. Khomskii**. *Bond-versus site-centred ordering and possible ferroelectricity in manganites*. Nat. Materials **3 (12),** 853–856 (2004).

[56] **B.B. van Aken**, **T. T. M. Palstra**, **A. Filippetti**, **N. A. Spaldin**. *The origin of ferroelectricity in magnetoelectric $YMnO_3$*. Nat. Materials **3 (3),** 164–170 (2004).

[57] **M. Mostovoy**. *Ferroelectricity in spiral magnets*. Phys. Rev. Lett. **96 (6),** 067 601 (2006).

[58] **T. Moriya**. *Anisotropic superexchange interaction and weak ferromagnetism*. Phys. Rev. **120 (1),** 91–98 (1960).

[59] **Y. J. Choi**, **H. T. Yi**, **S. Lee**, **Q. Huang**, **V. Kiryukhin**, **S. W. Cheong**. *Ferroelectricity in an Ising chain magnet*. Phys. Rev. Lett. **100 (4),** 047 601 (2008).

[60] **C. Israel**, **N. D. Mathur**, **J. F. Scott**. *A one-cent room-temperature magnetoelectric sensor*. Nat. Mater **7 (2),** 93–94 (2008).

[61] **J. Ryu**, **S. Priya**, **K. Uchino**, **H.E. Kim**. *Magnetoelectric effect in composites of magnetostrictive and piezoelectric materials*. J Electroceram. **8 (2),** 107–119 (2002).

[62] **M. Born**, **R. Oppenheimer**. *On the quantum theory of molecules*. Ann. Phys. **84,** 457 (1927).

[63] **E. Fermi**. *Eine statistische Methode zur Bestimmung einiger Eigenschaften des Atoms und ihre Anwendung auf die Theorie des periodischen Systems der Elemente*. Zeitschrift für Physik A Hadrons and Nuclei **48,** 73 (1928).

[64] **L. Thomas**. *The calculation of atomic fields*. Proc. Camb. Phil. Soc **23,** 542 (1927).

[65] **W. Kohn**, **L.J. Sham**. *Self-consistent equations including exchange and correlation effects*. Phys. Rev. **140 (4A),** 1133–& (1965).

[66] **U. Von Barth**, **L. Hedin**. *A local exchange-correlation potential for the spin polarized case. i*. Journal of Physics C: Solid State Physics **5,** 1629 (1972).

[67] **L.M. Sandratskii**. *Energy Band Structure Calculations for Crystals with Spiral Magnetic Structure*. Phys. Status Solidi B **136 (1),** 167–180 (1986).

[68] **J. Kübler**. *Theory of Itinerant Electron Magnetism*. Clarendon Press (2000).

[69] **L. Hedin**, **B. Lundqvist**. *Explicit local exchange-correlation potentials*. Journal of Physics C: Solid State Physics **4,** 2064 (1971).

[70] **S. Vosko**, **L. Wilk**, **M. Nusair**. *Accurate spin-dependent electron liquid correlation energies for local spin density calculations: a critical analysis*. Canadian Journal of Physics **58,** 1200 (1980).

[71] **V. L. Moruzzi**, **J. F. Janak**, **A. R. Williams**. *Calculated electronic properties of Metals*. Pergamon New York (1978).

[72] **J. Perdew**, **Y. Wang**. *Accurate and simple analytic representation of the electron-gas correlation energy*. Phys. Rev. B **45,** 13 244 (1992).

[73] **D. Ceperley**, **B. Alder**. *Ground state of the electron gas by a stochastic method*. Phys. Rev. Lett. **45,** 566 (1980).

[74] **C. Amador**, **W. Lambrecht**, **B. Segall**. *Application of generalized gradient-corrected density functionals to iron*. Phys. Rev. B **46,** 1870 (1992).

[75] **V.I. Anisimov**, **F. Aryasetiawan**, **A.I. Lichtenstein**. *First-principles calculations of the electronic structure and spectra of strongly correlated systems: The LDA+U method*. J Phys.-Condens. Mat. **9 (4),** 767–808 (1997).

[76] **M. Lüders**, **A. Ernst**, **M. Däne**, **Z. Szotek**, **A. Svane**, **D. Ködderitzsch**, **W. Hergert**, **B. L. Gyor?y**, **W. M. Temmerman**. *Self-interaction correction in multiple scattering theory*. Phys. Rev. B **71,** 205109 (2005).

[77] **J. C. Phillips**, **L. Kleinman**. *New method for calculating wave functions in crystals and molecules*. Phys. Rev. **116,** 287 (1959).

[78] **D. Hamann**, **M. Schlüter**, **C. Chiang**. *Norm-conserving pseudopotentials*. Phys. Rev. Lett. **43,** 1494 (1979).

[79] **G. Bachelet**, **D. Hamann**, **M. Schlüter**. *Pseudopotentials that work: From H to Pu*. Phys. Rev. B **26,** 4199 (1982).

[80] **G. Kerker**. *Non-singular atomic pseudopotentials for solid state applications*. Journal of Physics C: Solid State Physics **13,** L189 (1980).

[81] **D. Vanderbilt**. *Optimally smooth norm-conserving pseudopotentials*. Phys. Rev. B **32,** 8412 (1985).

[82] **N. Troullier**, **J. Martins**. *A straightforward method for generating soft transferable pseudopotentials*. Solid State Commun. **74 (7),** 613 (1990).

[83] **N. Troullier**, **J. Martins**. *Efficient pseudopotentials for plane-wave calculations*. Phys. Rev. B **43 (3),** 1993 (1991).

[84] **S. Goedecker**, **M. Teter**, **J. Hutter**. *Separable dual-space Gaussian pseudopotentials*. Phys. Rev. B **54 (3),** 1703 (1996).

[85] **D. Vanderbilt**. *Soft self-consistent pseudopotentials in a generalized eigenvalue formalism*. Phys. Rev. B **41 (11),** 7892–7895 (1990).

[86] **G. Kresse**, **J. Furthmuller**. *Efficient iterative schemes for ab initio total-energy calculations using a plane-wave basis set*. Phys. Rev. B **54,** 11 169–11 186 (1996).

[87] **G. Kresse**, **D. Joubert**. *From ultrasoft pseudopotentials to the projector augmented-wave method*. Phys. Rev. B **59,** 1758–1775 (1999).

[88] **G. Kresse**, **J. Furthmuller**. *Efficiency of ab-initio total energy calculations for metals and semiconductors using a plane-wave basis set*. Comp. Mater. Sci. **6 (1),** 15–50 (1996).

[89] **J. Shin**, **V. B. Nascimento**, **A. Y. Borisevich**, **E. W. Plummer**, **S. V. Kalinin**, **A. P. Baddorf**. *Polar distortion in ultrathin BaTiO3 films studied by in situ LEED I-V*. Phys. Rev. B **77 (24),** 245 437 (2008).

[90] **R.E. Cohen**. *Surface effects in ferroelectrics: Periodic slab computations for BaTiO3*. Ferroelectrics **194,** 323–342 (1997).

[91] **R. I. Eglitis**, **S. Piskunov**, **E. Heifets**, **E. A. Kotomin**, **G. Borstel**. *Ab initio study of the $SrTiO_3$, $BaTiO_3$ and $PbTiO_3$ (001) surfaces*. Ceram. Int. **30,** 1989–1992 (2004).

[92] **C.-C. Duan**, **J.P. Velev**, **R.F. Sabirianov**, **W.N. Mei**, **S.S. Jaswal**, **E.Y. Tsymbal**. *Tailoring magnetic anisotropy at the ferromagnetic/ferroelectric interface*. Appl. Phys. Lett. **92 (12),** 122905 (2008).

[93] **M. Hölzer**. *Magnetoelektrische Kopplung an multiferroischen Grenzflächen*. Diplomarbeit Martin-Luther-Universität Halle-Wittenberg (2010).

[94] **C. A. F. Vaz**, **J. Hoffman**, **A.-B. Posadas**, **C. H. Ahn**. *Magnetic anisotropy modulation of magnetite in $Fe_3O_4/BaTiO_3(100)$ epitaxial structures*. Appl. Phys. Lett. **94 (2),** 022 504 (2009).

[95] **J. Wang**, **Y. Zhang**, **J. Ma**, **Y. Lin**, **C.-W. Nan**. *Magnetoelectric behavior of $BaTiO_3$ films directly grown on $CoFe_2O_4$ ceramics*. J Appl. Phys. **104 (1),** 014 101 (2008).

[96] **J. Liu**, **Y. Zhang**, **Y. Lin**, **C.-W. Nan**. *Magnetoelectric coupling in $BaTiO_3/(NiFe_2O_4/BaTiO_3)(n)$ (n=1,2,3,4) multilayered thin films*. J Appl. Phys. **105 (8),** 083 915 (2009).

[97] **G. Sreenivasulu**, **V. H. Babu**, **G. Markandeyulu**, **B. S. Murty**. *Magnetoelectric effect of $(100-x)BaTiO_3$-$(x)NiFe_{1.98O4}$ (x=20-80 wt %) particulate nanocomposites*. Appl. Phys. Lett. **94 (11),** 112 902 (2009).

[98] **H. Zheng**, **J. Wang**, **S. E. Lofland**, **Z. Ma**, **L. Mohaddes-Ardabili**, **T. Zhao**, **L. Salamanca-Riba**, **S. R. Shinde**, **S. B. Ogale**, **F. Bai**, **D. Viehland**, **Y. Jia**, **D. Schlom**, **M. Wuttig**, **A. Roytburd**, **R. Ramesh**. *Multiferroic $BaTiO_3$-$CoFe_2O_4$ nanostructures*. Science **303,** 661–663 (2004).

[99] **W. H. Tuan**, **S. S. Chen**. *Processing and Properties of $BaTiO_3$-Ni Ferroelectric-Ferromagnetic Composites*. Ferroelectrics **381,** 167–175 (2009).

[100] **Y. S. Koo**, **K. M. Song**, **N. J. Hur**, **J. H. Jung**, **T.-H. Jang**, **H. J. Lee**, **T. Y. Koo**, **Y. H. Jeong**, **J. H. Cho**, **Y. H. Jo**. *Strain-induced magnetoelectric coupling in $BaTiO_3/Fe_3O_4$ core/shell nanoparticles*. Appl. Phys. Lett. **94 (3),** 032 903 (2009).

[101] **C.-G. Duan**, **S. S. Jaswal**, **E. Y. Tsymbal**. *Predicted magnetoelectric effect in $Fe/BaTiO_3$ multilayers: Ferroelectric control of magnetism*. Phys. Rev. Lett. **97 (4),** 047 201 (2006).

[102] **M. K. N.**, **J. D. Burton**, **J. P. Velev**, **S. S. Jaswal**, **E. Y. Tsymbal**. *Magnetoelectric effect at the $SrRuO_3/BaTiO_3$ (001) interface: An ab initio study*. Appl. Phys. Lett. **95 (5),** 052 501 (2009).

[103] **J. D. Burton**, **E. Y. Tsymbal**. *Prediction of electrically induced magnetic reconstruction at the manganite/ferroelectric interface*. Phys. Rev. B **80 (17),** 174 406 (2009).

[104] **C. Yu**, **M. J. Pechan**, **S. Srivastava**, **C. J. Palmstrøm**, **M. Biegaslski**, **C. Brooks**, **D. Schlom**. *Ferromagnetic resonance in ferromagnetic/ferroelectric $Fe/BaTiO_3/SrTiO_3(001)$*. J Appl. Phys. **103 (7),** 07B108 (2008).

[105] **P. Weinberger**. *Theory for Ordered and Disordered Matter*. Clarendon Press, Oxford (1990).

List of publications

[E1] **M. Fechner**, **S. Ostanin**, **I. Mertig**. *Effect of the surface polarization in polar perovskites studied from first principles*. Phys. Rev. B **77 (9),** 094 112 (2008).

[E2] **M. Fechner**, **I. V. Maznichenko**, **S. Ostanin**, **A. Ernst**, **J. Henk**, **P. Bruno**, **I. Mertig**. *Magnetic phase transition in two-phase multiferroics predicted from first principles*. Phys. Rev. B **78 (21),** 212 406 (2008).

[E3] **M. Fechner**, **S. Ostanin**, **I. Mertig**. *Magnetoelectric coupling at biferroic interface studied from first principles*. J. Phys.: Conf. Ser. **200 (7),** 072 027 (2010).

[E4] **M. Fechner**, **S. Ostanin**, **I. Mertig**. *Effect of oxidation of the ultrathin Fe electrode material on the strength of magnetoelectric coupling in composite multiferroics*. Phys. Rev. B **80 (9),** 094 405 (2009).

[E5] **M. Fechner**, **I. V. Maznichenko**, **S. Ostanin**, **A. Ernst**, **J. Henk**, **I. Mertig**. *Ab initio study of magnetoelectricity in composite multiferroics*. Phys. Status Solidi (b) **247 (7),** 1600–1607 (2010).

[E6] **M. Hölzer**, **M. Fechner**, **S. Ostanin**, **I. Mertig**. *Effect of interfacial Cr on magnetoelectricity of $Fe_2/CrO_2/BaTiO_3(001)$*. Phys. Rev. B **81 (21),** 214428 (2010).

[E7] **N.F. Hinsche**, **M. Fechner**, **P. Bose**, **S. Ostanin**, **J. Henk**, **I. Mertig**, **P. Zahn**. *Strong influence of the complex bandstructure on the tunneling electroresistance: A combined model and ab-initio study*. submitted 2010.

[E8] **L. Gerhard**, **K. Yamada**, **A. F. Takács**, **R. J. H. Wesselink**, **M. Däne**, **M. Fechner**, **S. Ostanin**, **A. Ernst**, **I. Mertig**, **W. Wulfhekel**. *Magneto-electric coupling via induced surface charge*. submitted 2010.

[E9] **F. Klimenta**, **L. Meyerheim**, **A. Ernst**, **K. Mohseni**, **S. Ostanin**, **M. Fechner**, **S. Parihar**, **I.V. Maznichenko**, **I. Mertig**, **J. Kirschner**. *The structural secrets of multiferroic interfaces*. submitted 2010.

x

Acknowledgement

Curriculum vitae

Personal data:

name	Michael Fechner
address	Ritter-von-Schuh Platz 17, 90459 Nürnberg
date of birth and place	05. August 1981, Schkeuditz (Germany)

Education:

1989 - 1993	Primary school: Trotha Grundschule
1993 - 2000	Grammar school: Hans-Eisler Gymnasium Halle
2000 - 2001	Military service
2001 - 2006	Studies of physics at Martin Luther University Halle-Wittenberg completed as graduate physicist (degree: Diplom-Physiker) Diploma title: "Dispersionsrelation von Feldemissionszuständen" ("Dispersion Relation of Image Potential States")
since 2007 -	PhD Studentship at Max Planck Instute of Microstructure Physics
since 2007 -	Member of the International Max Planck Research School for Science and Technology of Nanostructures
break in 2009 -	Parental leave for four months starting from september

Eidesstattliche Erklärung

Hiermit erkläre ich gemäß §5 Abs. 2b der Promotionsordnung der Naturwissenschaftlichen Fakultät II-Chemie und Physik der Martin-Luther-Universität Halle-Wittenberg vom 3.2.2004, dass ich die vorliegende Arbeit

MAGNETOELECTRIC COUPLING AT MULTIFERROIC INTERFACES

selbständig und ohne fremde Hilfe verfaßt, andere als die von mir angegebenen Quellen und Hilfsmittel nicht benutzt und die den benutzten Werken wörtlich oder inhaltlich entnommenen Stellen als solche kenntlich gemacht habe. Ich erkläre, die Angaben wahrheitsgemäß gemacht und keine wissenschaftliche Arbeit an einer anderen wissenschaftlichen Einrichtung zur Erlangung eines akademischen Grades eingereicht zu haben.

Halle, den 30. Juni 2010

Michael Fechner